

**POLYTECHNIQUE MONTRÉAL**

affiliée à l'Université de Montréal

**Raman spectroscopy of spatially confined phonon-polaritons in GaSe Van der  
Waals crystals**

**CLÉMENT GRADZIEL**

Département de génie physique

Mémoire présenté en vue de l'obtention du diplôme de *Maîtrise ès sciences appliquées*  
génie physique

Avril 2023

**POLYTECHNIQUE MONTRÉAL**

affiliée à l'Université de Montréal

Ce mémoire intitulé :

**Raman spectroscopy of spatially confined phonon-polaritons in GaSe Van der  
Waals crystals**

présenté par **Clément GRADZIEL**

en vue de l'obtention du diplôme de *Maîtrise ès sciences appliquées*

a été dûment accepté par le jury d'examen constitué de :

**Yves-Alain PETER**, président

**Sébastien FRANCOEUR**, membre et directeur de recherche

**Sean MOLESKY**, membre

## ACKNOWLEDGMENTS

First of all, I would like to thank Telecom Physique Strasbourg and Polytechnique Montreal for allowing me to study at such a prestigious university and to discover the great city that is Montreal, as well as the discovery of the Quebec culture.

I want to thank Alexandre Dabrowski, Anne-Sophie Cordan and Yann Leroy from Telecom Physique Strasbourg for their help and support, especially during this period of uncertainty during Covid-19 that made the start of my program complicated.

I am delighted to have been able to work and share good times with all my lab mates. I warmly thank Anne-Laurence, Leonard, Maxime, and Marcin for their kind welcome and precious help during my first steps in the laboratory. Ryan and Arnaud, I really enjoyed your company, and the support we gave each other allowed us to move forward together. And Simon, we managed to keep our good resolution to go to the gym! Thank you very much for your support during the end of my master's degree.

I would also like to thank the technicians of the physics department, Samuel and Emile, for their help in the mechanical design of the components necessary for my instrumentation.

I want to thank my supervisor, Professor Sébastien Francoeur, for trusting me with this very inspiring project. For the always very informative and inspiring discussions and for your encouragement towards ever more innovative solutions. I was able to gain confidence professionally but also personally. Finally, I thank you for the support you gave me throughout the writing of this thesis.

Finally, I address a particular thanks to my family and my friends, here in Montréal, but also in France (coucou la "contre!"), for their constant support.

## RÉSUMÉ

Les polaritons sont des états mixtes composés de lumière et de matière. Ils proviennent d'un couplage fort entre une onde électromagnétique et une excitation de la matière. Dans les matériaux polaires, le couplage de la lumière avec un phonon polaire est appelé un phonon-polariton (PhP). Les PhPs se propageant dans les matériaux hyperboliques ont attiré beaucoup d'intérêt pour leur capacité à fortement confiner la lumière. L'interaction de ces PhPs avec un émetteur quantique devrait considérablement améliorer les interactions lumière-matière au-delà du régime de couplage faible. La recherche sur les PhPs est alors très active pour des applications en nanophotonique et en optique quantique.

Les PhPs sont généralement étudiés en utilisant une technique de microscopie de champ proche (s-SNOM). Cette technique mesure la dispersion des PhPs, dans laquelle leurs propriétés sont encodées. Les PhPs sont excités par un laser infrarouge pendant qu'une pointe d'AFM mesure leur champ proche pour en extraire leur longueur d'onde. Cependant, certains matériaux polaires supportent la propagation de PhPs à des fréquences situées dans l'infrarouge lointain. Il n'existe pas de source laser efficace dans ces fréquences pour le moment, ce qui limite le champ d'application du s-SNOM pour l'étude des PhPs.

La spectroscopie Raman utilise la lumière du visible pour étudier des excitations de la matière dans l'infrarouge. Cette technique est communément utilisée pour étudier les phonons optiques par exemple. Dans un travail précédemment effectué dans le groupe, la possibilité d'étudier les propriétés des PhPs en utilisant la spectroscopie Raman en configuration rétro-diffusée a été démontrée. Cette configuration permet de mesurer les PhPs présents dans le GaSe, un matériau hyperbolique 2D qui supporte la propagation de PhPs ayant des fréquences aux alentours de  $240 \text{ cm}^{-1}$ .

Dans le travail présenté ici, l'étude des PhPs du GaSe est continuée en se focalisant sur les phénomènes de confinement spatial. Dans un premier temps, la dispersion des PhPs en fonction de l'épaisseur du cristal de GaSe est mesurée. Le confinement des PhPs augmente avec l'épaisseur qui diminue, ce qui mène à un aplatissement des courbes de dispersion. Des facteurs de confinement  $\lambda_0/\lambda_{PhPs}$  allant jusqu'à 100 sont estimés. Ces valeurs sont plus grandes que celles rapportées dans le hBN et le MoO<sub>3</sub>, deux matériaux hyperboliques dans lesquels les PhPs sont activement étudiés. La vitesse de groupe des PhPs a aussi pu être extraite, et une valeur de  $0.014c$  a été obtenue. Même si des vitesses deux ordres de grandeur plus basses ont déjà été rapportées, cela démontre la capacité de la spectroscopie Raman pour extraire des propriétés des PhPs. Ensuite, la fréquence des PhPs en fonction de l'épaisseur du

crystal est comparée avec des spectres Raman calculés. Un excellent accord entre l'expérience et la simulation est trouvé. Une diminution en fréquence de  $18.1 \text{ cm}^{-1}$  est mesurée entre une épaisseur de 380 et 84 nm. Cela montre que sous l'effet d'un confinement vertical, la fréquence des PhPs diminue avec l'épaisseur de l'échantillon. De plus, le modèle théorique utilisé afin de calculer les spectres Raman reproduit fidèlement les données expérimentales. Enfin, l'effet du confinement latéral sur des PhPs se propageant dans des échantillons rectangulaires est sondé à l'aide de la spectroscopie Raman résolue en polarisation. Quand les dimensions de l'échantillon sont proches de la distance de propagation des PhPs, la fréquence des PhPs est affectée à cause des nouvelles conditions aux frontières. Quand la propagation des PhPs entre l'axe court et l'axe long de l'échantillon est sondée, une anisotropie de polarisation en fréquence des PhPs est mesurée. Un écart en fréquence maximal de  $1.2 \text{ cm}^{-1}$  est mesurée entre les polaritons se propageant le long d'un axe de l'échantillon et ceux se propageant le long d'une diagonale. La longueur de propagation des PhPs peut alors être estimée comme étant la longueur de l'axe long de l'échantillon. Une distance de propagation maximale de  $328 \mu\text{m}$  a pu être estimée, ce qui est un ordre de grandeur plus grand que ce qui est rapporté dans la littérature pour les PhPs du hBN et du  $\text{MoO}_3$ .

Toutes ces contributions démontrent que la spectroscopie Raman est une technique prometteuse pour étudier les propriétés des PhPs dans les matériaux polaires 2D. De plus, les propriétés des PhPs extraites du GaSe démontrent que ce matériau est un bon candidat pour le développement futur de la phonon-polaritonique.

## ABSTRACT

Polaritons are mixed states of light and matter that arise from the strong coupling between an electromagnetic wave and a matter excitation. In a polar material, the coupling of light with a polar phonon is called a phonon-polariton (PhP). PhPs propagating in hyperbolic 2D materials recently gained much interest because of their ability to confine electromagnetic fields strongly. They would highly improve light-matter interactions with a quantum emitter beyond the weak coupling regime. PhPs are therefore intensively investigated for potential applications in nanophotonics and quantum optics.

PhPs are usually probed using scattering-type scanning near-field optical microscopy (s-SNOM). This technique measures the PhPs dispersion, which encodes all their properties. PhPs are excited by an infrared laser source, and an AFM tip probes their near-field to retrieve the PhPs wavelength. However, some polar materials support PhPs with frequencies in the far-infrared spectral region. Efficient laser sources are not available yet in this frequency region, which limits the uses of s-SNOM for probing PhP dispersions.

Raman spectroscopy uses visible light to probe infrared material excitations and is commonly used to probe optical phonons in crystals. In a previous work of the group, the possibility of probing PhP properties using Raman scattering in the backward configuration was demonstrated. This configuration allows for the measurement of highly confined PhPs in GaSe, a 2D hyperbolic material that supports PhPs with frequencies around  $240\text{ cm}^{-1}$ .

The study of PhPs in GaSe is pursued in this work by focusing on the study of PhP spatial confinement effects. First, the PhP dispersion is measured as a function of the crystal thickness. The PhP confinement increases with decreasing the sample thickness. This results in a flattening of the PhP dispersion curve. Moreover, PhP confinement factors  $\lambda_0/\lambda_{PhPs}$  of up to 100 is reported. This value is higher than those reported in the most recent literature in hBN and MoO<sub>3</sub>, two other hyperbolic materials in which PhPs are intensively studied. The PhP group velocity can also be extracted from the dispersion curve, and a value of  $0.014c$  is obtained. It is higher than the ones reported in the literature by two orders of magnitude, but it still demonstrates the ability of Raman scattering to extract important PhP properties. Then, the PhP frequency as a function of the sample thickness is compared with computed PhP Raman spectra. An excellent agreement between the two is observed, and a diminution of the PhP frequency of  $18.1\text{ cm}^{-1}$  is observed between sample thicknesses of 380 and 84 nm. It demonstrates that PhPs experience frequency shifts because of vertical confinement effects, which is faithfully reproduced by computational methods. Finally, lateral confinement

effects of PhPs are probed using polarization-resolved Raman scattering in rectangular GaSe samples. Indeed, when the sample dimension approaches the PhP propagation length, the frequency of the PhP shifts because of the new boundary conditions. Polarization anisotropy of the PhP frequency is measured when the propagation of the PhP is scanned from the short to the long sample axis. A frequency shift of up to  $1.2 \text{ cm}^{-1}$  is reported between PhPs propagating along the sample axes and ones propagating along a diagonal of the sample. The PhP propagation length can be estimated as the length of the sample long axis. A propagation length of up to  $328 \text{ }\mu\text{m}$  is estimated, one order of magnitude higher than that reported in the literature for hBN and  $\text{MoO}_3$ .

These contributions demonstrate that Raman scattering is a promising technique to probe the properties of PhPs from 2D polar materials. Moreover, the PhP properties extracted from GaSe place this material as an excellent candidate for the future developments of phonon-polaritonics.

## TABLE OF CONTENTS

ACKNOWLEDGMENTS . . . . .	iii
RÉSUMÉ . . . . .	iv
ABSTRACT . . . . .	vi
TABLE OF CONTENTS . . . . .	viii
LIST OF TABLES . . . . .	x
LIST OF FIGURES . . . . .	xi
ACRONYMS AND ABBREVIATIONS . . . . .	xiii
CHAPTER 1 INTRODUCTION . . . . .	1
1.1 Research objectives . . . . .	3
1.2 Thesis outline . . . . .	4
CHAPTER 2 LITERATURE REVIEW . . . . .	6
2.1 Hyperbolic materials . . . . .	6
2.2 Phonon-polaritons in hyperbolic materials . . . . .	9
2.3 Gallium Selenide overview . . . . .	12
CHAPTER 3 PHONON-POLARITONS IN 2D HYPERBOLIC MATERIALS . . . . .	16
3.1 Phonons in uniaxial crystals . . . . .	16
3.1.1 Phonons dispersion . . . . .	16
3.1.2 Polar phonons in uniaxial crystals . . . . .	18
3.2 Photon/phonon coupling : phonon-polaritons in hyperbolic materials . . . . .	21
3.2.1 The electromagnetic wave equation . . . . .	22
3.2.2 Polarization response of a polar material to an electric field . . . . .	23
3.2.3 Phonon-polariton dispersion in bulk materials . . . . .	25
3.3 Raman scattering by phonon-polaritons . . . . .	29
3.3.1 Raman scattering by phonons . . . . .	30
3.3.2 Raman scattering by polar phonons and phonon-polaritons . . . . .	34
3.4 Phonon-polaritons in 2D materials: numerical modeling . . . . .	39
3.4.1 Symmetric waveguide model . . . . .	40

3.4.2	4x4 matrix formalism . . . . .	42
3.4.3	Finite element method model . . . . .	47
CHAPTER 4 SAMPLE FABRICATION AND RAMAN SETUP . . . . .		53
4.1	Sample preparation and characterization . . . . .	53
4.1.1	Mechanical exfoliation . . . . .	53
4.1.2	Protecting sample from oxidation . . . . .	55
4.1.3	Dimensional characterization . . . . .	56
4.2	Phonon-polariton measurement . . . . .	56
4.2.1	Optical setup . . . . .	57
4.2.2	Excitation beam dimension . . . . .	59
4.2.3	Calibration . . . . .	60
4.2.4	Data processing . . . . .	62
4.2.5	Angular Broadening . . . . .	65
CHAPTER 5 RESULTS . . . . .		69
5.1	Raman measurement of phonon-polaritons dispersion . . . . .	69
5.1.1	Thickness dependent phonon-polaritons dispersion . . . . .	69
5.1.2	Thickness dependent Raman spectra . . . . .	77
5.2	Polarization resolved Raman scattering of laterally confined phonon-polaritons	80
5.2.1	Mathematical resources for the data processing . . . . .	80
5.2.2	Polarization resolved Raman scattering from Silicon . . . . .	82
5.2.3	Polarization-resolved Raman scattering from bulk GaSe . . . . .	88
5.2.4	Polarization-resolved Raman scattering from thin rectangular GaSe samples . . . . .	93
CHAPTER 6 CONCLUSION . . . . .		110
6.1	Contributions . . . . .	110
6.2	future works and conclusion . . . . .	111
REFERENCES . . . . .		113
APPENDIX . . . . .		121

**LIST OF TABLES**

Table 2.1	List of the state-of-the-art PhPs properties in the literature for hBN and MoO <sub>3</sub> . . . . .	11
Table S1	Normal mode of vibration of GaSe . . . . .	121
Table S2	Pure phonon frequencies of GaSe in the studied frequency range at room temperature . . . . .	122
Table S3	Character table of the $D_{3h}$ space group . . . . .	122

## LIST OF FIGURES

Figure 1.1	Typical polariton dispersion curve . . . . .	3
Figure 2.1	Isofrequency contour for different classes of material . . . . .	7
Figure 2.2	Isofrequency contour for hyperbolic materials . . . . .	8
Figure 2.3	Example of hyperbolic material structures . . . . .	9
Figure 2.4	Planar focusing of PhPs launched from gold antenna in $\alpha$ -MoO <sub>3</sub> . . .	13
Figure 2.5	Crystal structure of the GaSe different polytypes with their stacking order . . . . .	14
Figure 3.1	1D chain of atoms with 2 different atoms per unit primitive cell . . .	17
Figure 3.2	Phonon dispersion of a 1D biatomic unit cell in the first Brillouin zone	19
Figure 3.3	2D lattice mode oscillations for the two phonon branches . . . . .	20
Figure 3.4	Angular dispersion of GaSe polar phonons . . . . .	22
Figure 3.5	Permittivity of GaSe near polar phonon frequencies . . . . .	26
Figure 3.6	PhPs dispersion in a infinite GaSe crystal . . . . .	29
Figure 3.7	Inelastic light scattering energy diagram . . . . .	31
Figure 3.8	Near-forward and backscattering Raman geometries . . . . .	38
Figure 3.9	Geometry of the symmetric waveguide . . . . .	41
Figure 3.10	PhP Dispersion curves in a 1 $\mu$ m GaSe slab waveguide suspended in air calculated with the analytical model . . . . .	42
Figure 3.11	PhP electric field map intensity in an asymmetric waveguide . . . . .	45
Figure 3.12	Geometry of the symmetric and asymmetric waveguide of the FEM model . . . . .	48
Figure 3.13	Mesh element quality for the two geometries . . . . .	49
Figure 3.14	Distribution of the mesh elements quality for the two geometries . . .	49
Figure 3.15	Comparison of the obtain PhP dispersion between the analytic solution and the FEM model for the symmetric waveguide . . . . .	50
Figure 3.16	Example of obtained PhP fields using the FEM model . . . . .	52
Figure 4.1	Exfoliation process followed to produce thin GaSe flakes . . . . .	54
Figure 4.2	Impact of the presence of contamination on AFM images . . . . .	55
Figure 4.3	AFM image and extracted line profile of a GaSe flake . . . . .	57
Figure 4.4	Raman backscattering experimental setup . . . . .	58
Figure 4.5	Measurement of the beam radius focused by an under illuminated 0.55 NA objective . . . . .	61
Figure 4.6	Raman spectra from a GaSe flake of thickness 380 nm at 300 K . . . .	63

Figure 4.7	Calculated Raman spectra and experimental PhP dispersion for a 650 nm sample . . . . .	67
Figure 5.1	PhP dispersions from GaSe samples of different thicknesses . . . . .	71
Figure 5.2	Surface PhP field maps from two GaSe waveguides suspended in air .	74
Figure 5.3	Calculated surface PhP dispersion for GaSe slabs of different thicknesses suspended in air . . . . .	76
Figure 5.4	Computed PhP Raman dispersion as a function of the GaSe thickness	76
Figure 5.5	Comparison between computed thickness dependent Raman spectra and experimental data . . . . .	78
Figure 5.6	PhP electric field as a function of the GaSe crystal thickness . . . . .	79
Figure 5.7	Polarization-resolved Raman intensity from a Si sample . . . . .	84
Figure 5.8	Phonon frequency polarization response from a Si sample . . . . .	86
Figure 5.9	Autocorrelation of the intensity and frequency Si polarization response	87
Figure 5.10	Polarization-resolved Raman intensity from a bulk GaSe sample . . .	89
Figure 5.11	Autocorrelation on the polarization-resolved Raman intensity from bulk GaSe . . . . .	90
Figure 5.12	Polarization-resolved Raman frequency from a bulk GaSe sample . .	92
Figure 5.13	Autocorrelation of the frequency offset extracted from the polarization response . . . . .	92
Figure 5.14	Intensity polarization response of the first sample . . . . .	95
Figure 5.15	Frequency polarization response of the first sample . . . . .	96
Figure 5.16	Intensity polarization response of the second sample . . . . .	100
Figure 5.17	Frequency polarization response of the second sample . . . . .	101
Figure 5.18	Intensity polarization response of the third sample . . . . .	106
Figure 5.19	Frequency polarization response of the third sample . . . . .	107

**ACRONYMS AND ABBREVIATIONS**

**AFM** atomic force microscopy.

**BEC** Bose-Einstein condensate.

**CCD** charge coupled device.

**EMCCD** electron multiplying charge coupled device.

**FEM** finite element method.

**FWHM** full width at half maximum.

**GaP** gallium phosphide.

**GaSe** gallium selenide.

**Le** longitudinal extraordinary.

**NA** numerical aperture.

**PDMS** polydimethylsiloxane.

**PhP** phonon-polariton.

**PTIR** photothermal induced resonance.

**QCL** quantum cascade laser.

**Si** silicon.

**s-SNOM** scattering-type scanning near-field optical microscopy.

**Te** transverse extraordinary.

**TE** transverse electric.

**TM** transverse magnetic.

**To** transverse ordinary.

## CHAPTER 1 INTRODUCTION

A crystal has many natural resonances that define the dielectric properties of a material. These resonances can have various origins and are usually modeled by a matter excitation associated with a characteristic frequency. When an electromagnetic wave with a similar frequency propagates in a material, absorption can occur by the emission of such matter excitations in the crystal. They can carry an electric and/or a magnetic dipole momentum through which electromagnetic energy can be shared. An electromagnetic wave can eventually couple to this dipole momentum to create a hybrid quasi-particle called a *polariton*. This mixed state of light and matter shares properties of its two constituents: the ability to interact with dipole moments through the electromagnetic field; a large momentum provided by the matter excitation mass.

In 1950 and 1951, *Tolpygo* [1]<sup>1</sup> and *Huang* [2] independently came up with the first theoretical description of the coupling between an electromagnetic field and a polar matter excitation. They demonstrated the contribution of the dipole momentum induced by the oscillation of ions in ionic crystals on the material dielectric properties. In 1958, *Hopfield* demonstrated the implication of the strong coupling between light and excitons in the dielectric properties of semiconductors. He also proposed the name "polariton" to define the quasi-particle arising from the strong coupling between light and a matter excitation [3]. Polaritons mainly occur in the infrared spectral region because of the low energy of crystal resonances. They are now intensively investigated for applications in nanophotonics and quantum optics owing to their ability to manipulate highly confined electromagnetic fields at the nanoscale [4–7].

The range of matter excitations that can couple to light to form a polariton is broad [8]. For example, excitons are electron-hole pairs bound by Coulomb interaction in gaped materials such as semiconductors. They can emit or absorb light through their optical dipole moment. When an exciton is in the vicinity of a photon, they eventually couple to form a bosonic quasi-particle called an *exciton-polariton* [9]. One of their main attraction is their ability to exhibit Bose-Einstein condensate (BEC) at room temperature. In contrast, typical atomic BECs require to be cooled down to a very low temperature of 100 nK [10]. Among many other applications [11–13], they are actively investigated in order to artificially reproduce the photosynthesis reaction occurring in plants [14].

In metals, the main channel of absorption near the plasma frequency is via the emission of a plasmon. It is the quantified mode of oscillating charge density, such as free electrons in

---

<sup>1</sup>This reference is a translation from Russian of the original article written in 1950.

metals. Thanks to the electron charge, a plasmon carries an oscillating dipole moment that can couple to a photon and form a *plasmon-polariton*. Because light propagates very little in metals, plasmon-polaritons are mainly observed at dielectric/metal interfaces and referred to as surface plasmon-polaritons (SPPs). They have a much higher momentum than light in vacuum due to the mass of the electron, which results in very confined electromagnetic fields. A confinement factor  $\lambda_0/\lambda_{\text{polariton}}$  of up to 240 has been reported in graphene [15]. When a quantum emitter is coupled with such a confined light, it results in a strong coupling that significantly enhances the emission properties of the emitter. Breakdown of selection rules and 2<sup>nd</sup> order emission processes like single or bi-photon emission as efficient as dipolar transitions are for example expected [15]. Additionally, the ease of surface patterning of metals allows for the fabrication of sub-wavelength devices that find applications in sensors, imaging, and SPP waveguides [16].

Finally, in polar and ionic crystals, the quanta of lattice oscillations known as phonons can be accompanied by an oscillating dipole. These phonons are referred to as polar phonons and can eventually couple to a photon to form a quasi-particle called a *phonon-polariton* (PhP). They are actively studied in a class of highly anisotropic materials that possess permittivities of opposite signs along different crystal axes. These materials display a hyperbolic dispersion and can therefore host electromagnetic modes with very high momentum [17]. PhPs propagating in such materials are therefore called hyperbolic phonon-polaritons. They were first reported in hexagonal boron nitride (hBN) [18], where they are intensively studied. In recent years, biaxial  $\alpha$ -MoO<sub>3</sub> has gained more interest because of its stronger anisotropy and even more confined hyperbolic PhPs [19]. The literature review will further discuss the properties of PhPs.

A typical dispersion relation curve of a polariton is shown in Fig. 1.1. The dispersion relation expresses the polariton frequency  $\omega$  as a function of its wavevector  $q$ . The red and the black dashed lines depict the dispersion of light and the one of the matter excitation, respectively. Since matter excitations generally have a much higher wave vector than light, its dispersion is flat when scaled to that of light. These two dispersions intersect without coupling. When coupling occurs, the polariton dispersion exhibits two branches that never intersect. The lower-frequency branch extrapolates to the dispersion of light at low wavevectors and the excitation frequency at high wavevectors. The high-frequency branch displays the opposite behavior. The polariton mixed property is more pronounced where the curvature of the dispersion is maximum, which corresponds to the dispersion region where polaritonic properties can be most effectively exploited.

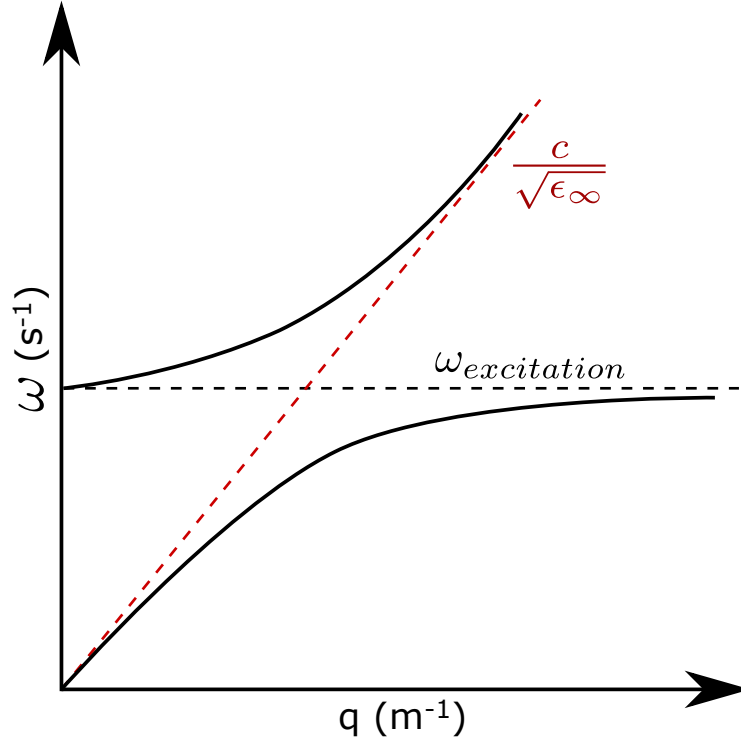


Figure 1.1 Typical polariton dispersion curve.  $q$  and  $\omega$  are the polariton wavevector and frequency, respectively. The solid black curves depict the polariton upper and lower branches originating from the strong coupling of light with a matter excitation. The red dashed line is the dispersion of light in a given material that sees the high frequency permittivity  $\epsilon_\infty$ . The black dashed line is the dispersion of the material excitation.

### 1.1 Research objectives

The study of PhPs is an emerging field that needs constant experimental innovations in order to characterize and harvest their promising properties. The real-space imaging technique scattering-type scanning near-field optical microscopy (s-SNOM) initiated the study of highly confined PhPs in naturally-occurring hyperbolic materials [18]. To both launch and measure PhPs, this technique requires an infrared laser that is focused onto the apex of an atomic force microscopy (AFM) tip. In  $\text{MoO}_3$  and hBN, the frequency of the PhPs lie around  $950$  and  $1500 \text{ cm}^{-1}$ , respectively [20, 21]. A quantum cascade laser (QCL) is therefore utilized, but with the cost of an AFM, this technique necessitates a large budget to be implemented. Moreover, there exist a lots of materials with polar resonance at even lower frequencies ( $\approx 250 \text{ cm}^{-1}$ ) [22], where efficient laser sources are not available yet.

By limiting the study of PhPs to the use of near-field scanning techniques, the expansion of knowledge about PhPs is impeded by technological constraints and poor accessibility of these

experiments by research groups. The inelastic Raman scattering spectroscopy technique was proposed in the group to overcome these limitations. Raman scattering is a well established spectroscopy technique for studying infrared excitations such as optical phonons. As it only requires a visible laser source and a spectrometer, it can be more easily implemented than the s-SNOM, making the study of PhPs more accessible to the community. The measurement of PhPs using near-forward Raman scattering has been demonstrated in 1965 by *Henry* and *Hopfield* in a GaP crystal, very early in the study of PhPs [23]. This geometry is however restricted to the study of weakly confined PhPs. Raman scattering in the backward configuration enables the measurement of excitations with much higher wavevectors. The democratization of 2D materials in recent years enabled the emergence of highly confined PhPs that remained inaccessible in near-forward Raman scattering. *Bergeron* demonstrated that PhP dispersions from 2D gallium selenide (GaSe) crystals can be accessed by using Raman scattering in the backward configuration [24].

This work pursues the study of PhPs in GaSe by using Raman backscattering and explores the PhP properties that can be extracted with this technique. First, the dispersion of PhPs is measured as a function of the GaSe crystal thickness. It enables the extraction of the PhP confinement factor and group velocity. Then, computed PhP Raman spectra as a function of the sample thickness are compared with measured PhP frequencies. Finally, polarization-resolved Raman scattering from rectangular GaSe crystals is utilized to probe lateral confinement of PhPs. Because lateral confinement occurs when the propagation length of a PhP approaches the dimension of the crystal, the propagation length of the measured PhPs can be estimated.

## 1.2 Thesis outline

Chapter 2 reviews the properties of hyperperbolic materials and their applications. Then the most recent literature on PhPs is overviewed and the properties of GaSe are presented.

The next chapter presents the theory of PhPs. First, the dispersion of phonons and polar phonons is presented. Then, the dispersion of PhPs is derived by combining Maxwell's equations with the material polarization induced by the interaction of partially charged atoms with an electromagnetic field. The Raman theory of phonons and PhPs from GaSe is derived afterward. Finally, the computational methods used in this thesis are presented. The dispersion of a symmetric waveguide and a matrix formalism for PhP field computation are overviewed, and a finite element method (FEM) model developed in this work is presented.

Chapter 4 presents the experimental methodology of this work. The samples are prepared

using mechanical exfoliation, and their dimensions are characterized using an optical microscope and an AFM. The optical setup is then presented, along with the data processing routine used to exploit the Raman spectra.

Chapter 5 presents the important results of this work. First, a flattening of PhPs dispersion curves is observed experimentally as the thickness of the GaSe samples decreases. This demonstrates that PhPs experience vertical confinement. Next, the reported PhP frequencies are compared with computed Raman spectra to demonstrate the computational model efficiency in reproducing the experimental data. Then, the lateral confinement of PhPs is studied in rectangular GaSe samples. Polarization-resolved Raman scattering is used to probe frequency polarization anisotropy revealing spatial confinement of PhPs.

Finally chapter 6 briefly reviews the contributions of this work, the problems encountered and the planned future studies.

## CHAPTER 2 LITERATURE REVIEW

This chapter presents an overview of the literature on hyperbolic PhPs. Hyperbolic materials are first briefly introduced. Then, the state-of-the-art measurement techniques and reported properties of hyperbolic PhPs are presented. A few applications in nanophotonics are also reviewed. Finally, the crystal structure and essential properties of GaSe are overviewed, along with the limited literature available on polaritons from GaSe.

### 2.1 Hyperbolic materials

The displacement field  $\mathbf{D}$  quantifies the total electric dipole moment induced by the movement of the material bound charges upon the propagation of an electric field  $\mathbf{E}$ . In the case of a linear response,  $\mathbf{D}$  and  $\mathbf{E}$  are linked by the permittivity tensor such as

$$\mathbf{D} = \epsilon_0 \overset{\leftrightarrow}{\epsilon} \mathbf{E}, \quad (2.1)$$

where  $\epsilon_0$  and  $\overset{\leftrightarrow}{\epsilon}$  are the vacuum and relative permittivity. The latter is a rank-2 tensor that expresses as

$$\overset{\leftrightarrow}{\epsilon} = \begin{pmatrix} \epsilon_x & 0 & 0 \\ 0 & \epsilon_y & 0 \\ 0 & 0 & \epsilon_z \end{pmatrix} \quad (2.2)$$

in the crystal coordinates, in which off-diagonal terms vanish. This tensor encodes the information describing the material light-matter interaction properties (absorption, transmission, reflection). These interactions are frequency dependent and are described by the dispersion relation  $\overset{\leftrightarrow}{\epsilon}(\omega) = \frac{c^2 k^2}{\omega^2}$ , where  $c$  is the vacuum celerity of light,  $k$  the electromagnetic field wavevector and  $\omega$  its frequency.

The symmetry of the crystal imposes the symmetry of the permittivity tensor. Solid-state materials are then separated into two categories: isotropic and anisotropic. Isotropic materials have the same permittivity in each direction so the permittivity tensor is a scalar. They correspond to fully symmetric (cubic) crystals. Anisotropic materials have different permittivity values depending on the direction of the induced polarization. They are also separated into two categories: uniaxial and biaxial. Uniaxials are crystals of tetragonal, hexagonal, and trigonal symmetry. They have a symmetry plane in which the permittivity

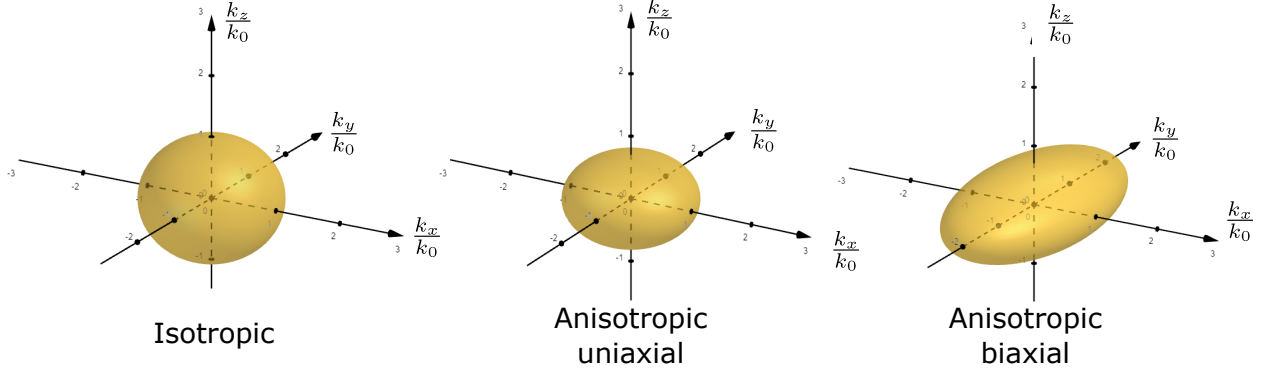


Figure 2.1 Typical isofrequency contour for the different classes of material, normalized by  $k_0$ .

is similar  $\epsilon_x = \epsilon_y = \epsilon_\perp$ . This plane is orthogonal to the crystal uniaxial, which has a different permittivity  $\epsilon_z = \epsilon_\parallel \neq \epsilon_\perp$ . Biaxial materials have a orthorhombic, monoclinic, and triclinic crystal symmetry. These materials are highly anisotropic because each crystal axis has a different permittivity [25].

The general dispersion relation of a material can be written as

$$\frac{k_x^2}{\epsilon_x} + \frac{k_y^2}{\epsilon_y} + \frac{k_z^2}{\epsilon_z} = k_0^2, \quad (2.3)$$

where  $k_0 = \frac{\omega}{c}$  is the vacuum wave vector. When the frequency of the propagating electromagnetic field in the material is fixed, this relation defines the possible values of each wavevector component. The wavevector and the permittivity of uniaxials can be written in terms of parallel and orthogonal components (with respect to the crystal uniaxial). This leads to

$$\frac{k_\parallel^2}{\epsilon_\parallel} + \frac{k_\perp^2}{\epsilon_\perp} = k_0^2, \quad (2.4)$$

where  $k_\perp^2 = k_x^2 + k_y^2$  and  $k_\parallel^2 = k_z^2$ .

Fig. 2.1 depicts the isofrequency contour for the classes of material presented above. As can be seen, the contour is always closed so the value of the wavevector is bounded. The contour from an isotropic material is spherical because of the same permittivity in each crystal direction. The contour is ellipsoidal with symmetric values in the  $k_x - k_y$  plane for uniaxial materials, which is expected from the in-plane symmetry of such materials. Finally, the contour of biaxial materials also displays an ellipsoidal surface but with no symmetry plane.

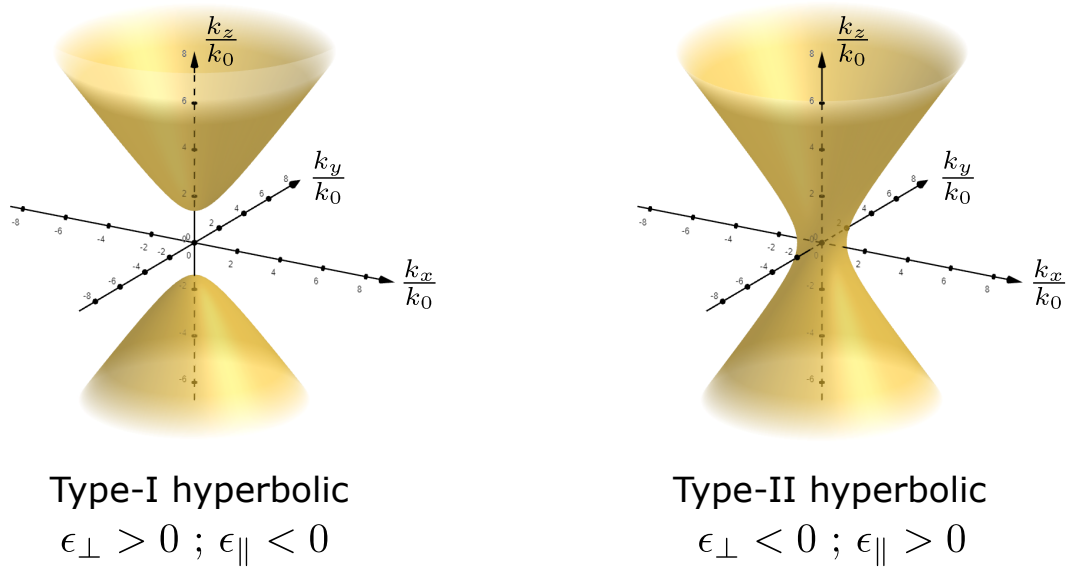


Figure 2.2 Typical isofrequency contour for uniaxial hyperbolic materials, normalized by  $k_0$ .

In some cases, the different permittivities of anisotropic materials can have opposite signs. Fig. 2.2 displays the isofrequency contour of such materials in the case of uniaxial materials. The isofrequency contour is not closed and defines a hyperboloid. These materials are called *hyperbolic* materials and can host highly confined electromagnetic fields [26]. The frequency region in which one permittivity component is negative is called a *reststrahlen band*. In this region, the material reflectivity gets very high (near 100% at normal incidence for type-II hyperbolic materials), similar to metals under the plasma frequency [27]. Some materials, like GaSe, exhibit double Reststrahlen bands where the orthogonal and parallel permittivities are negative. No volume mode is allowed in these frequency regions, so only highly confined surface waves can propagate.

A material can be artificially designed to exhibit a hyperbolic behavior in a given frequency region. These materials are called metamaterials and are made of microstructured periodic arrangement with a few tens of nanometer to micrometer periodicity. Hyperbolic behavior arises when the electromagnetic field wavelength approaches the spatial periodicity of the metamaterial [17]. They can be designed to operate in the near-infrared and visible spectral regions. Fig. 2.3 depicts three types of artificial arrangements: multilayer hyperbolic metamaterials are metal/dielectric stacking with sub-wavelength layer sizes. The electrons are therefore confined in 2D layers. The in-plane and out-of-plane permittivities are fixed by the selected materials and the thickness of the metal and dielectric layers. These are mostly used to design type-II hyperbolic materials. Then, nanowires hyperbolic metama-

materials are metal nanowires arranged with a sub-wavelength periodicity inside a dielectric material. Again, the in-plane and out-of-plane permittivities can be tailored by choice of the materials, the periodicity and the radius of the nanowires. They are mostly designed to exhibit type-I hyperbolicity. Finally, surfaces with sub-wavelength patterning are called hyperbolic metasurfaces. They are intensively used in metallic materials to manipulate the dispersion of SPPs [16]. Finally, some 2D materials such as black phosphorus and hBN are naturally hyperbolic because of their strong polar resonances highly confined between the crystal monolayers [26, 28].

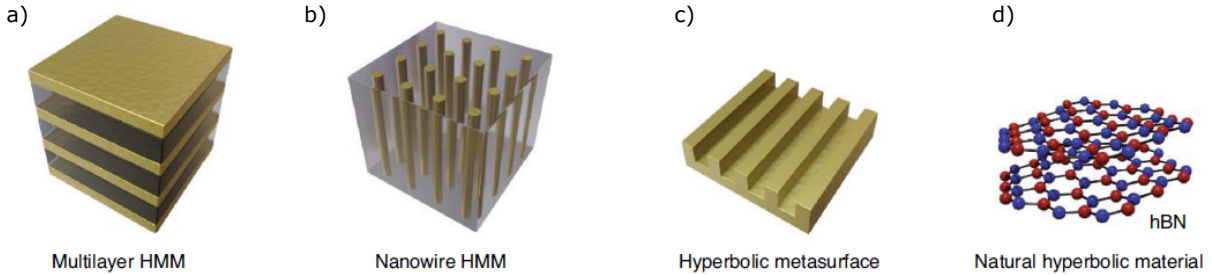


Figure 2.3 Example of hyperbolic materials. HMM stands for hyperbolic metamaterial. From left to the right are multilayers, nanowires, metasurfaces, and natural hyperbolic materials. Adapted with permission from Ref. [26] © 2022 Springer Nature.

Hyperbolic materials are actively studied for many applications such as sub-wavelength imaging, high-resolution lithography, hyperlensing and sub-wavelength cavities [17, 27, 29]. In addition, the highly confined electromagnetic fields hosted by such materials greatly enhance light-matter interactions [17].

## 2.2 Phonon-polaritons in hyperbolic materials

In highly anisotropic polar materials, hyperbolic regions can occur between the TO and LO polar phonon frequencies. In these regions, strongly confined electromagnetic fields eventually couple to polar phonons to form a quasi-particle called a hyperbolic phonon-polariton (PhP). First observed in gallium phosphide (GaP) crystals by *Henry* and *Hopfield* in 1965 [23], they are now reported in many other hyperbolic polar materials such as quartz [30], hBN and MoO<sub>3</sub> [31].

PhPs are entirely characterized by their dispersion relation  $\omega(k)$ . PhP properties can then be extracted such as the group velocity  $\partial\omega/\partial k$ , life time, propagation length, confinement factor<sup>1</sup> (ratio between the vacuum and PhP wavelengths  $\lambda_0/\lambda_{PhPs}$ ) and quality factor (ratio

<sup>1</sup>Also sometimes referred as optical compression in the literature.

between the real and imaginary part of the PhP wavevector  $\text{Re}(k)/\text{Im}(k)$ ). The experimental techniques used to extract the PhP properties are reviewed below.

The most common method is the scattering-type scanning near-field optical microscopy (s-SNOM). An infrared laser source is focused on the tip of an AFM to generate and probe PhPs at the surface of a material. The evanescent field generated upon the polarization of the AFM tip provides enough light momentum to launch PhPs inside the hosting material [18]. AFM can also be used as a probe only for the imaging of PhP evanescent fields launched via a metal-edge [32]. The dispersion relation is retrieved by measuring the PhP wavelength and sweeping over frequencies.

A recent approach called photothermal induced resonance (PTIR), already used to identify the chemical composition of samples with 1  $\mu\text{m}$  depth [33], has recently emerged as a tool for observing the propagation of PhPs. The sample, also illuminated using an infrared laser source to excite PhPs in resonance, thermally expands upon light absorption. This expansion is measured by the AFM tip and provides a measurement of the sample absorption at nanoscale spatial dimensions ( $\sim 10$  nm). [20,34]. Like s-SNOM, this technique enables the visualization of PhP waves in real space. Therefore, the PhP wavelength can be extracted as a function of the frequency.

Despite its first use for their experimental observation, Raman scattering is little used for the measurement of PhPs. Before the recent democratization of 2D materials, PhPs were only probed in bulk polar materials. These volume PhPs are weakly confined and most of their dispersion is close to the light line. Raman scattering in the near-forward configuration enables to probe such weakly confined PhPs [23, 35–39]. Then, near-field imaging techniques gained much more interest, and has become the dominant technique for the characterization of PhPs. However, near-field imaging techniques are limited by the availability of far-infrared laser sources. Indeed, some 2D polar materials such as  $\text{WSe}_2$  and  $\text{GaSe}$  exhibit polar resonances at frequencies around  $250\text{ cm}^{-1}$  [22]. Consequently, PhPs from these materials cannot be accessed. It has recently been demonstrated that Raman scattering in the backward configuration is a promising technique to probe the properties of highly confined PhPs in  $\text{GaSe}$  [24]. This geometry remains unexploited and absent from the literature, whereas it could favor the study of PhPs in a wider range of materials. To date, only one article used Raman backscattering to study PhPs in 2D materials [40]. This work aims to further demonstrate the capacity of Raman backscattering in extracting the PhP propagation properties.

Table 2.1 presents the state-of-the-art properties of PhPs from hBN and  $\text{MoO}_3$ , on which the study of PhPs is mainly focused. The values given in a reference may come from measure-

Material	Reference	Group velocity	Quality factor	Confinement factor	lifetime (ps)	Propagation length ( $\mu\text{m}$ )
hBN	[34] <sup>1</sup>	-	90	7	4.2	25
	[31]	-	60	5	5	25
	[21]	-	42	31	-	-
	[41] <sup>2</sup>	-	-	60	-	-
	[32]	$0.002c$	-	-	1.8	6
MoO <sub>3</sub>	[42]	-	40	2.5	-	-
	[20]	$0.001c$	-	33	12	-
	[19]	-	29	50	-	-
	[43] <sup>3</sup>	$0.002c$	20	5	13.9	6.8
	[44]	$8 \times 10^{-4}c$	-	60	22	8

Table 2.1 List of the state-of-the-art PhP properties in the literature for hBN and MoO<sub>3</sub>. The quantities presented are a selection of the best reported in each article. Moreover, values from the same article could originate from different experimental conditions (sample thickness, substrate, measurement method. <sup>1</sup>: 99% <sup>10</sup>B isotopically purified hBN crystal ; <sup>2</sup>: PhP measured from hBN monolayers ; <sup>3</sup>: isotopically purified 99.9% <sup>92</sup>Mo and 99.0% <sup>100</sup>Mo MoO<sub>3</sub> crystals.

ments made under different experimental conditions (different sample thickness, substrate, or measurement method). The higher PhP quality factor of 90 has been reported in thin 99%  $^{10}\text{B}$  purified hBN [34]. Isotopic purity minimizes phonon scattering due to isotropic disorder and therefore increases the lifetime of optical phonons [45]. Because the decay rate of PhPs is closely related to the optical phonon lifetime, isotopically purified crystals improve PhP quality factors. The highest PhP confinement factor is 60, reported in hBN and  $\text{MoO}_3$ . In 2D materials, the confinement factor is influenced by the crystal thickness. The reported value in hBN is measured in a monoatomic layer [41] and therefore defines the highest confinement factor obtainable in this materials. The thickness of the  $\text{MoO}_3$  crystal in which this value was measured was 55 nm. Finally, the slowest PhP was measured in the biaxial  $\text{MoO}_3$ , with a group velocity of  $8 \times 10^{-4}c$  [44]. This low group velocity denotes a strong PhP dispersion in favor of high confinement factors. It nevertheless implies lower propagation lengths. Extremely low group velocities are interesting for enhanced light-matter interactions with quantum emitters. However, they should be avoided when a higher propagation length is prioritized, in PhP waveguides for example.

From sensing to quantum optics, the range of applications of PhPs in nanophotonics is broad [4,6]. The choice of the substrate is of great importance as it modulates the dispersion of PhPs as well as their propagation properties. Planar refractive optics for PhP is achieved by substrate patterning. For example, super-resolution imaging with PhPs from hBN has been demonstrated [47]. Moreover, PhP lenses with sub-diffraction properties were fabricated with  $1/15 \lambda_0$  focal length and  $1/33 \lambda_0$  spot size [46]. Fig. 2.4 shows the focusing of PhP fields launched from circular gold antennas to thin  $\text{MoO}_3$  crystal. The circular shape of the antennas induces a circular PhP wavefront, leading to a focusing of the polaritonic field. For disc diameters of  $D = 6.7, 11$  and  $15 \mu\text{m}$ , the FWHM spot size is  $\sim 600, 430$  and  $420 \text{ nm}$ , and the focal length is  $\sim 7, 5$  and  $3 \mu\text{m}$ , respectively. Hence, the focal length can be tuned by the disk diameter and the PhP energy, as demonstrated by Ref. [46]. These focusing properties could be utilized to concentrate highly confined PhP fields in the vicinity of a quantum emitter to enhance light-matter interactions and improve second-order emission processes such as two-photon emission [48].

### 2.3 Gallium Selenide overview

The III-VI monochalcogenides family, from which GaTe and InSe and GaSe belong, have attracted many interests for the development of optoelectronic devices when reaching the few monolayer thickness regime. They are investigated for the development of piezoelectric devices that can be combined with their high photo-sensitivity [49]. They are also used as

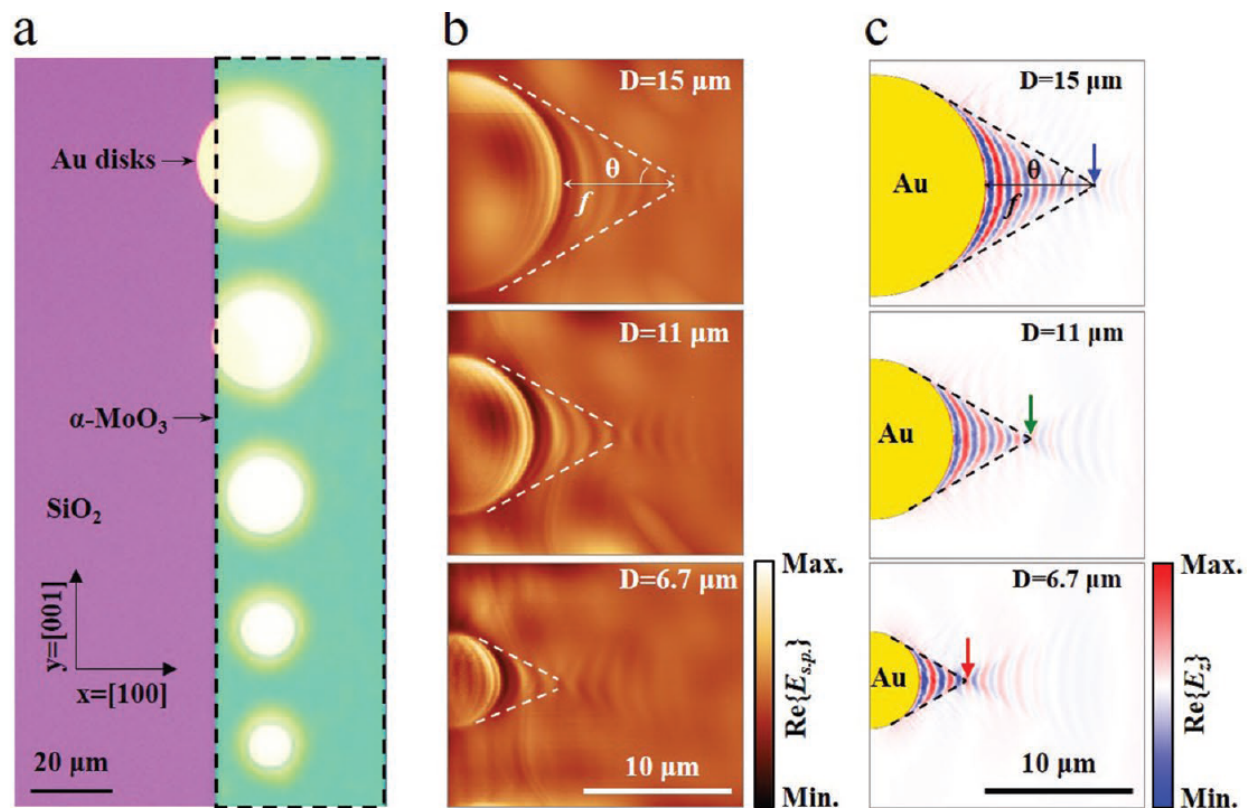


Figure 2.4 Planar focusing of PhPs launched from gold antenna in  $\alpha$ -MoO<sub>3</sub>. PhP are directly excited by a tunable infrared laser source focused on gold disc antennas. **a)** optical microscopy image of the device, showing gold nano-disks of different diameters, under the  $\alpha$ -MoO<sub>3</sub> flake delimited by the green region. **b)** Real-space image of the PhP  $E_z$  field using s-SNOM, at a frequency  $910 \text{ cm}^{-1}$ .  $f$  is the focal length,  $\theta$  the focusing angle and  $D$  the disk diameters. **c)** Simulated  $E_z$  PhP field for the same experimental settings. Adapted with permission from [46] © 2022 John Wiley and Sons.

a photocatalyst to improve the efficiency of the water splitting reaction. This field aims to find a high-yield production protocol for clean energy production of  $\text{H}_2$ . [50,51]

GaSe is a semi-conductor of the III-VI group with a direct band-gap of 2.00 eV [52]. 4 polytypes  $\epsilon$ ,  $\beta$ ,  $\gamma$ , and  $\delta$  exist due to the possible different stacking ordering between layers [53]. In this work, GaSe crystals were grown by the Bridgman method. With this method, the dominant polytype is the  $\epsilon$ , belonging to the  $D_{3h}$  space group. Without an inversion center, this polytype presents a non-zero  $\chi^{(2)}$  that is intensively exploited in the literature [54–56]. The  $\epsilon$  polytype has a ABA stacking with 8 atoms per primitive cell, composed of 2 layers of 4 atoms bounded via the Van der Waals force. Therefore, 2D GaSe layers can be fabricated using mechanical exfoliation. All the space groups and stacking order are listed in Ref. [53] and shown in Fig. 2.5

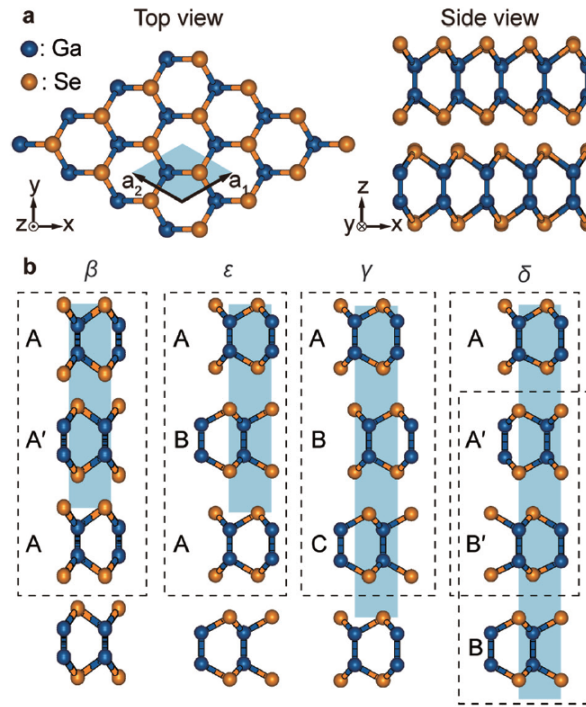


Figure 2.5 Crystal structure of the different GaSe polytypes with their stacking order. Adapted with permission from Ref. [53] © 2020 Royal Society of Chemistry.

Having two pairs of polar phonons with intersecting LO-TO splitting, GaSe is a promising hyperbolic material displaying type-II hyperbolicity and a double Reststrahlen band. Because of the strong polar resonances, GaSe supports highly confined hyperbolic PhPs. These polar resonances lie at a low frequency (around  $240 \text{ cm}^{-1}$ ). s-SNOM technique cannot be used because no laser source is available to excite these PhPs in resonance. The literature on PhPs from GaSe is therefore lacking [38]. In addition to keep demonstrating the interest of

Raman scattering for the study of PhPs, this work aims to enrich the literature of PhPs from GaSe by providing interesting polariton property measurements.

## CHAPTER 3 PHONON-POLARITONS IN 2D HYPERBOLIC MATERIALS

The theory of PhPs and Raman scattering by PhPs are presented in this chapter. First, the dispersion of phonons and polar phonons is presented. Then, the dispersion of PhPs propagating in an infinite crystal is derived. The theory of Raman scattering by phonons and PhPs of GaSe is then discussed through group theory. The symmetry of the GaSe phonons and PhPs and the Raman selection rules are presented. Finally, the numerical models used to compute the PhP electric fields and their dispersion are presented.

### 3.1 Phonons in uniaxial crystals

As photons are quanta of electromagnetic radiation, phonons are quanta of lattice oscillation in solid state matter. Phonons play an essential role in defining properties like specific heat, thermal and electric conductivity, and the speed of sound propagating inside materials. First, a derivation based on *Kittel's* textbook [57] of the dispersion of phonons in a 1D biatomic crystal is presented. Acoustic and optical phonons are introduced, along with some properties that can be extracted from their dispersion relation. Then, a focus is made on polar phonons from GaSe, along with their angular dispersion. Due to the crystal anisotropy, they can be expressed in a longitudinal, transverse, ordinary and extraordinary modes basis.

#### 3.1.1 Phonons dispersion

In a 1D crystal with 2 atoms per unit cell, there are two phonon branches. This section presents the derivation of their dispersion using the simple model of a linear chain of atoms bonded by springs.

The system considered is a unit cell with 2 atoms of different masses  $m_1$  and  $m_2 < m_1$ , depicted in Fig. 3.1. The force acting upon the atom of the  $s^{\text{th}}$  unit cell is described by the Hooke's law. Considering only nearest neighbors interactions, the 2<sup>nd</sup> law of Newton leads to the following set of coupled equations

$$\begin{aligned} m_1 \frac{d^2 u_s}{dt^2} &= C(v_s + v_{s-1} - 2u_s) \\ m_2 \frac{d^2 v_s}{dt^2} &= C(u_s + u_{s+1} - 2v_s). \end{aligned} \tag{3.1}$$

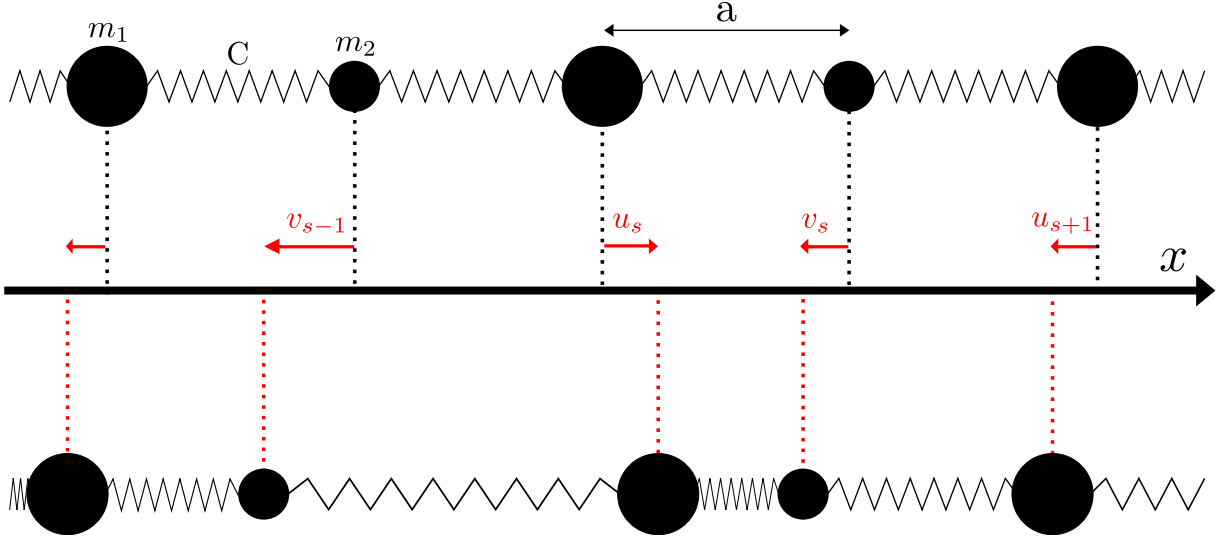


Figure 3.1 1D chain of atoms with 2 different atoms per unit primitive cell. The top shows the position of atoms at equilibrium ( $\mathbf{u}_s = \mathbf{v}_s = \mathbf{0}$ ).  $C$  is the spring constant,  $a$  the atomic distance at rest, and  $m_1$  and  $m_2 < m_1$  the atoms masses.  $u_s$  and  $v_s$  are the relative displacement from the equilibrium of the atoms of the  $s^{\text{th}}$  unit cell.

$C$  is the spring constant, and  $u_s$  and  $v_s$  the deviations from equilibrium of the  $s^{\text{th}}$  unit cell atom, with a mass  $m_1$  and  $m_2$  respectively.

A harmonic excitation and a linear response are assumed, leading to a harmonic response at the frequency of the vibrational mode  $\omega$ . A plane wave response is also assumed since no damping is considered. The atoms oscillation around equilibrium therefore writes

$$\begin{aligned} u_s &= u e^{isk_x a} e^{-i\omega t} \\ v_s &= v e^{isk_x a} e^{-i\omega t} \end{aligned} \quad (3.2)$$

where  $u, v$  are amplitudes,  $k_x = \frac{2\pi}{\lambda}$  is the wavevector,  $sk_x a$  is the phase shift accumulated with respect to the first atom of the chain, and  $a$  the distance between two atoms at rest. Substituting into Eq. 3.1 leads to a system of two equations

$$\begin{pmatrix} 2C - \omega^2 m_1 & C(1 + e^{-ik_x a}) \\ C(1 + e^{ik_x a}) & 2C - \omega^2 m_2 \end{pmatrix} \begin{pmatrix} u \\ v \end{pmatrix} = 0. \quad (3.3)$$

For non-trivial solutions,  $\omega^2$  and  $k_x$  must satisfy

$$\begin{vmatrix} 2C - \omega^2 m_1 & C(1 + e^{-ik_x a}) \\ C(1 + e^{ik_x a}) & 2C - \omega^2 m_2 \end{vmatrix} = 0, \quad (3.4)$$

describing a second order polynomial equation of  $\omega^2$ . The two solutions are

$$\begin{aligned} \omega_{optical}^2 &= \frac{2C(m_1 + m_2) + \sqrt{\Delta}}{2m_1 m_2} \\ \omega_{acoustic}^2 &= \frac{2C(m_1 + m_2) - \sqrt{\Delta}}{2m_1 m_2}, \end{aligned} \quad (3.5)$$

where  $\Delta = 4C^2(m_1 + m_2)^2 - 8m_1 m_2 C^2 [1 - \cos(k_x a)]$ . This describes the dispersion of the two branches, named *optical* and *acoustic* with  $\omega_{optical} > \omega_{acoustic}$ . In the long-wavelength approximation near the Brillouin zone center ( $k_x a \ll 1$ ), these dispersion relations simplify to

$$\begin{aligned} \omega_{optical} &\sim \sqrt{2C \left( \frac{1}{m_1} + \frac{1}{m_2} \right)} \\ \omega_{acoustic} &\sim \sqrt{\frac{1}{2} \frac{C}{m_1 + m_2}} \cdot k_x a. \end{aligned} \quad (3.6)$$

The optical branch is constant, while the acoustical one evolves linearly with  $k_x$ . Near the center of the Brillouin zone, optical phonons have a zero group velocity  $\frac{\partial \omega}{\partial k}$ . Thermal energy therefore only flows via acoustic phonons. The dispersion described by Eq. 3.5 is shown in Fig. 3.2, with an arbitrary mass ratio. Due to the different atomic masses, there is a frequency gap between the optical and acoustical branches at the edge of the Brillouin zone.

### 3.1.2 Polar phonons in uniaxial crystals

Atoms inside a unit cell of a crystal may be totally (ionic crystals) or partially (polar crystals) charged. In the case of GaSe, Ga and Se atoms are partially charged. The electronegativity of Se is higher than that of Ga. As a result, electron clouds composing covalent bonds are more localized around Se atoms, giving it a negative partial charge.

The motion of atoms inside their unit cell upon the propagation of a phonon can induce an oscillating electric dipole moment. Such vibrational modes are called *polar phonons*. Fig. 3.3 shows the 2D motion of atoms arranged in a linear chain. The unit cell is composed of

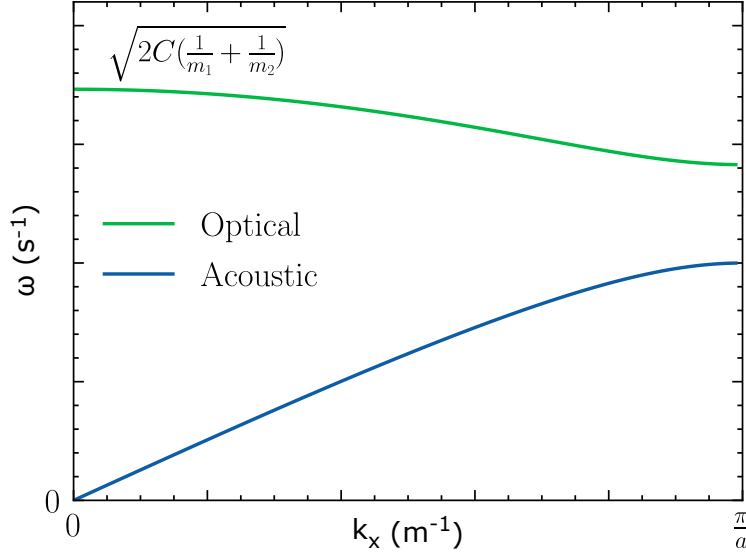


Figure 3.2 Phonon dispersion of a 1D biatomic unit cell in the first Brillouin described by Eq. 3.6. The ratio between  $m_1$  and  $m_2$  is arbitrary different from 1.

2 atoms of different partial charges. As can be seen, transverse polar phonons have dipole moments perpendicular to the propagation direction. These dipoles are not oriented toward the neighboring unit cells, preventing any influence on the restoring force between atoms. In the case of longitudinal polar phonons however, dipole moments can add up and increase the restoring force between atoms due to the long range Coulomb forces. As a result, the transverse/longitudinal degeneracy of polar phonons is lifted at the center of the Brillouin zone. The longitudinal phonon has a higher energy than the transverse phonon, and the energy splitting can be used to evaluate the dipole moment of a crystal unit cell. [58]

The lattice anisotropy of uniaxial crystals such as GaSe also affects the energy of polar phonons. The restoring force, formerly considered isotropic, now depends on the propagation direction inside the crystal. It lifts another degeneracy between polar phonons having an atomic motion either aligned or perpendicular to the crystal uniaxis. The firsts have an atomic motion along the uniaxis (symmetry  $A$ ) and are subscripted  $\parallel$ . The seconds are phonons with an atomic motion in the 2D plane (symmetry  $E$ ) orthogonal to the uniaxis, and are subscripted  $\perp$ . Here, Mulliken's symbols  $A$  and  $E$  identifies the representation associated to the normal modes [59]. As a result, there are a set of four non-degenerate polar phonons. Their frequencies are labeled  $\omega_{TO,\perp}$ ,  $\omega_{TO,\parallel}$ ,  $\omega_{LO,\perp}$  and  $\omega_{LO,\parallel}$ .

The frequency of these phonons therefore depends on the propagation angle with respect to the crystal uniaxis. For oblique angles, they have a mixed  $A$  and  $E$  or mixed  $TO$  and  $LO$  characters. This mixed nature depends on the dominant splitting process : the lattice

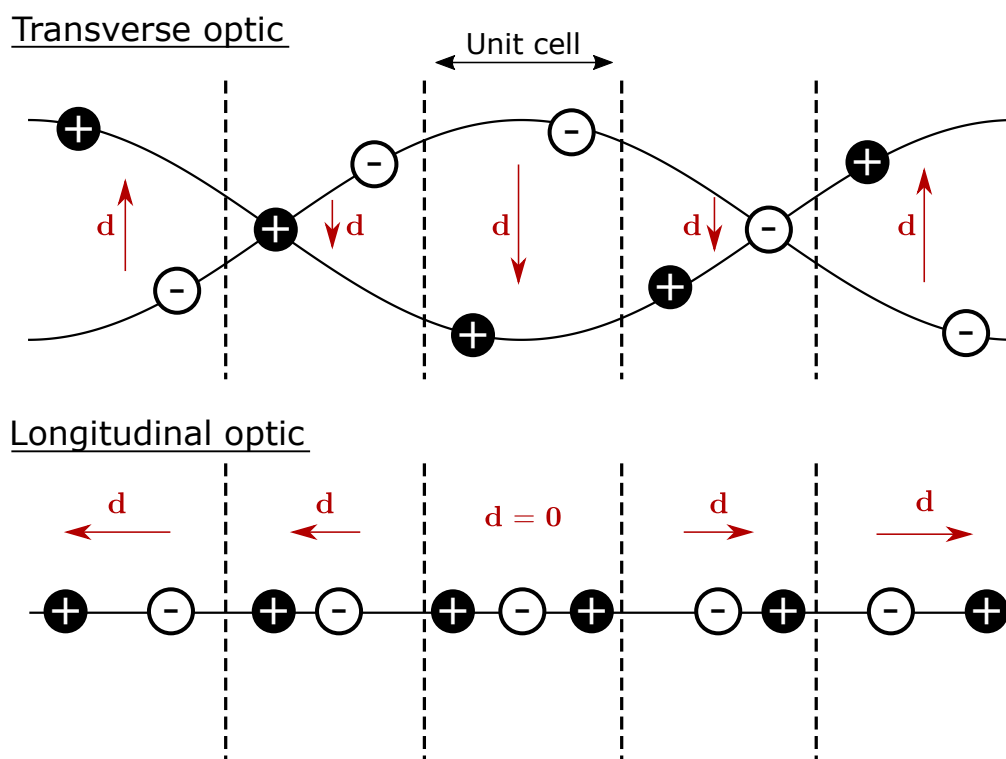


Figure 3.3 2D lattice mode oscillations of transverse and longitudinal phonons. Partial charge of atoms are depicted by "+" or "-" signs.  $\mathbf{d}$  is the dipole moment inside an unit cell induced by the displacement of the two partially charged atoms.

anisotropy or Coulomb forces at the origin of the LO-TO splitting.

In GaSe, the Coulomb interaction prevails [58]. Polar phonons will then display angular dispersion while preserving LO and TO characters. *Loudon* derived a simple set of formula, plotted in Fig. 3.4, to describes the resulting angular dispersion [60]

$$\omega_{To}^2(\theta) = \omega_{TO,\perp}^2 \quad (3.7a)$$

$$\omega_{Te}^2(\theta) = \omega_{TO,\perp}^2 \cos^2(\theta) + \omega_{TO,\parallel}^2 \sin^2(\theta) \quad (3.7b)$$

$$\omega_{Le}^2(\theta) = \omega_{LO,\parallel}^2 \cos^2(\theta) + \omega_{LO,\perp}^2 \sin^2(\theta). \quad (3.7c)$$

$\theta$  is the angle between the crystal uniaxis and the phonons wavevector. For GaSe, the set of frequencies, also listed in Table S1, is  $\omega_{TO,\perp} = 213.5 \text{ cm}^{-1}$ ,  $\omega_{TO,\parallel} = 236.5 \text{ cm}^{-1}$ ,  $\omega_{LO,\perp} = 253.3 \text{ cm}^{-1}$  and  $\omega_{LO,\parallel} = 246.1 \text{ cm}^{-1}$ . The subscripts transverse ordinary (To), transverse extraordinary (Te) and longitudinal extraordinary (Le) correspond to the new basis in which polar phonons are expressed. The To branch, equivalent to a mode propagating in an isotropic media, does not display any angular dispersion. The extraordinary Te and Le branches have their energy lying between the two TO and LO polar phonon frequencies, respectively. When studying other dispersive excitations, such as PhPs, this angular dispersion must be taken into account in the interpretation of the experimental data.

These formulas are derived assuming a few amounts of approximations, such as a small difference between  $\epsilon_{\perp}$  and  $\epsilon_{\parallel}$ . This limits the range of application of these equations near permittivity resonances for example. Other approximations are discussed by Loudon in Ref. [60]. In the next section, the dispersion of PhPs in polar material is derived. It will show the few discrepancies between Eqs 3.7 and an exact solution.

### 3.2 Photon/phonon coupling : phonon-polaritons in hyperbolic materials

This section illustrate how an infrared photon can couple to the dipole moment of a transverse polar phonon to form a hybrid quasi-particle called a *phonon-polariton* (PhP). This derivation combines Maxwell's equations with a classical oscillating bound charges model to describe the dispersion of this quantum quasi-particle in an infinite polar crystal.

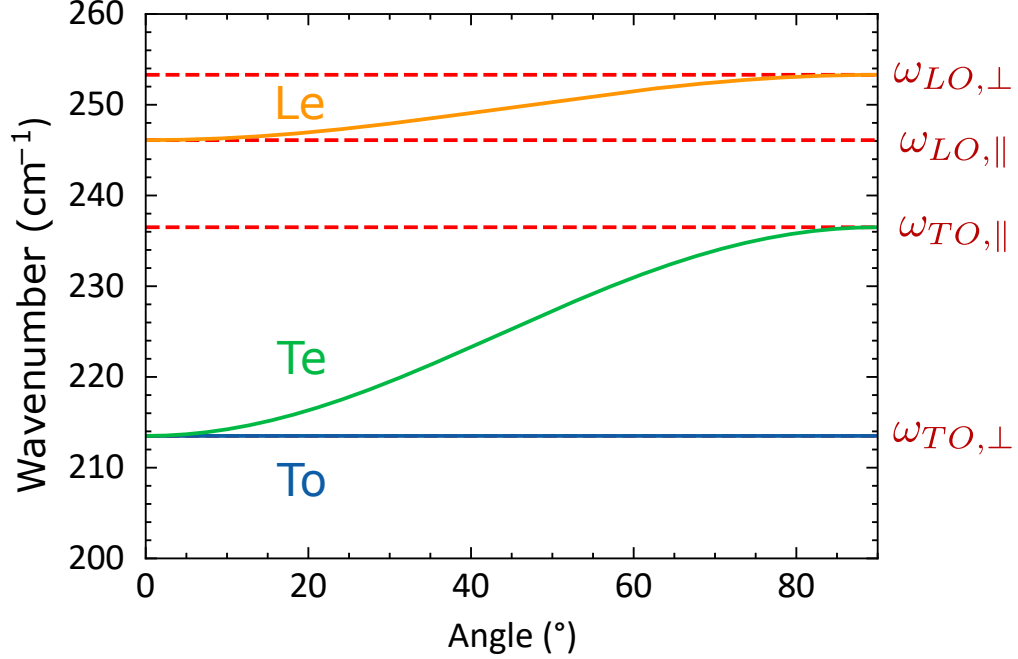


Figure 3.4 Angular dispersion of GaSe polar phonons calculated with Eqs. 3.7. The dashed red lines correspond to the frequencies of normal polar modes.

### 3.2.1 The electromagnetic wave equation

Assuming no free charge, the three Maxwell's equations used in this derivation are

$$\nabla \times \mathbf{E} = -\frac{\partial \mathbf{B}}{\partial t} \quad (3.8)$$

$$\nabla \times \mathbf{H} = \frac{\partial \mathbf{D}}{\partial t} \quad (3.9)$$

$$\nabla \cdot \mathbf{D} = 0. \quad (3.10)$$

The relations between the electric displacement field  $\mathbf{D}$ , the electric field  $\mathbf{E}$  and the polarization density  $\mathbf{P}$ , and between the magnetic flux  $\mathbf{B}$  and the magnetic field  $\mathbf{H}$ , are

$$\mathbf{D} = \epsilon_0 \mathbf{E} + \mathbf{P} \quad (3.11)$$

$$\mathbf{B} = \mu_0 \mathbf{H}, \quad (3.12)$$

without magnetization of the material.  $\epsilon_0$  is the vacuum permittivity and  $\mu_0$  is the vacuum

permeability. Assuming traveling plane waves, combining Eq. 3.8, 3.9, 3.11 and 3.12 leads to the eigenvalue equation

$$\mathbf{k} \times (\mathbf{k} \times \mathbf{E}) + \omega^2 \mu_0 (\epsilon_0 \mathbf{E} + \mathbf{P}) = 0 \quad (3.13)$$

known as the electromagnetic wave equation. With the identity  $\mathbf{u} \times \mathbf{v} \times \mathbf{w} = (\mathbf{u} \cdot \mathbf{w})\mathbf{v} - (\mathbf{u} \cdot \mathbf{v})\mathbf{w}$  and Eq. 3.10 developed as  $\mathbf{k} \cdot \mathbf{E} = -\frac{1}{\epsilon_0} \mathbf{k} \cdot \mathbf{P}$ , Eq. 3.13 can be written as [60]

$$\epsilon_0 \mathbf{E} = \frac{\frac{\omega^2}{c^2} \mathbf{P} - (\mathbf{k} \cdot \mathbf{P}) \mathbf{k}}{k^2 - \frac{\omega^2}{c^2}}. \quad (3.14)$$

$\omega$  is the frequency of the electromagnetic field,  $\mathbf{k}$  its wave vector and  $c = 1/\sqrt{\epsilon_0 \mu_0}$  its speed in vacuum. This equation describes the electromagnetic part of a PhP and will be the starting point to derive their dispersion relation. The polarization density  $\mathbf{P}$ , describing the response of the material to the electromagnetic field, is derived next using a model describing the interaction between oscillating bonded charges and an electric field.

### 3.2.2 Polarization response of a polar material to an electric field

Electric dipole moments originating from oscillating charged atoms can interact with an electric field, unless they are orthogonal. The interaction of a transverse polar phonon of frequency  $\omega_{TO}$  with a transverse electromagnetic field, both propagating in the same direction, is considered. Since the momentum of light is much lower than the size of the Brillouin zone, only long-wavelength optical polar phonons are considered. At equilibrium (without electromagnetic field), all the unit cells have the same dipole moment since there is no atomic displacement ( $\mathbf{u} = \mathbf{0}$ ).

When an electromagnetic field propagates inside a polar material, the dipole moment of each unit cell tends to align with the electric field. This induces a motion of the atoms at the frequency of the electric field and counterbalanced by the restoring force arising from atomic bonds. The motion of charged atoms is then described by the two following forces

$$\text{Hooke's law : } \mathbf{F}_H = -m\omega_{TO}^2 \mathbf{u} \quad (3.15)$$

$$\text{Lorentz law : } \mathbf{F}_L = e^* \mathbf{E} \quad (3.16)$$

where  $m$  is the effective mass and  $e^*$  is the effective charge of the unit cell.  $\mathbf{E}$  is the electric

field component of the electromagnetic wave. The atoms motion is relatively slow due to the long-wavelength nature of phonons near the centre of the Brillouin zone, so the magnetic contribution of the Lorentz force is neglected. The 2<sup>nd</sup> law of Newton leads to

$$\frac{d^2 \mathbf{u}}{dt^2} = -\omega_{TO}^2 \mathbf{u} + \frac{e^*}{m} \mathbf{E}. \quad (3.17)$$

Still in linear response theory, with an electromagnetic field at the frequency  $\omega$ , this equation can be written as

$$\mathbf{u} = \frac{e^*}{m} \frac{1}{\omega_{TO}^2 - \omega^2} \mathbf{E}. \quad (3.18)$$

The polarization density is defined as  $\mathbf{P} = ne^* \mathbf{u}$ , with  $n$  the number of unit cell per volume. As a result, the polarization attributed to the photon-phonon coupling is therefore

$$\mathbf{P}_{\text{photon-phonon}} = \epsilon_0 \epsilon_\infty \frac{\Omega_p^2}{\omega_{TO}^2 - \omega^2} \mathbf{E}, \quad (3.19)$$

where  $\Omega_p^2 = \frac{ne^{*2}}{m\epsilon_0\epsilon_\infty}$  is the effective plasma frequency [61], and  $\epsilon_\infty$  the high frequency ( $\omega \gg \omega_{TO}$ ) permittivity of the material. The high frequency polarization response

$$\mathbf{P}_\infty = \epsilon_0(\epsilon_\infty - 1) \mathbf{E} \quad (3.20)$$

should also be accounted for in the total polarization. Finally, the total polarization density originating from the coupling between an electromagnetic field and a transverse polar phonon is [2]

$$\mathbf{P} = \epsilon_0 \epsilon_\infty \frac{\Omega_p^2}{\omega_{TO}^2 - \omega^2} \mathbf{E} + \epsilon_0(\epsilon_\infty - 1) \mathbf{E}. \quad (3.21)$$

Since  $\mathbf{P} \propto \mathbf{E}$ , the coupling of light with polar phonons can be described by a linear material response. The displacement field is then linearly linked to the applied electric field by the permittivity tensor  $\overleftrightarrow{\epsilon}$

$$\mathbf{D} = \epsilon_0 \overleftrightarrow{\epsilon} \mathbf{E}. \quad (3.22)$$

To extract the permittivity tensor, Eq. 3.21 must be combined with the electromagnetic wave equation.

### 3.2.3 Phonon-polariton dispersion in bulk materials

To obtain the PhPs dispersion relation, the electromagnetic wave equation described by Eq. 3.13 must be combined with the polarization response of a polar material to an electromagnetic field, described by Eq. 3.21. The cases of isotropic and uniaxial materials are considered next.

#### Isotropic materials

In an isotropic material, the properties of electromagnetic modes are independent of the propagation direction. These modes can be decomposed into transverse ( $\mathbf{k} \perp \mathbf{P}$ ) and longitudinal ( $\mathbf{k} \parallel \mathbf{P}$ ) components [60]. Starting with the transverse solution, the combination of Eq. 3.14 with 3.21 leads to the dispersion relation of transverse PhPs

$$\epsilon(\omega) = \epsilon_\infty + \epsilon_\infty \frac{\Omega_p^2}{\omega_{TO}^2 - \omega^2} \quad (3.23)$$

where  $\epsilon(\omega) = \frac{c^2 k^2}{\omega^2}$ . The dispersion of longitudinal PhPs is much simpler since it reduces to

$$\omega = \sqrt{\frac{\epsilon_s}{\epsilon_\infty}} \omega_{TO} \equiv \omega_{LO}, \quad (3.24)$$

where  $\epsilon_s = \epsilon(0)$  corresponds to the material permittivity seen by a DC field. The dipole induced by longitudinal polar phonons is orthogonal to the transverse electromagnetic field. There is therefore no coupling between light and longitudinal polar phonons since it does not induce any polarization inside the material ( $\epsilon(\omega_{LO}) = 0$ ). As expected for the propagation of electromagnetic modes inside an isotropic material, PhPs are purely transverse. Rewriting Eq. 3.23 leads to the PhPs dispersion relation in isotropic materials

$$\epsilon(\omega) = \epsilon_\infty \frac{\omega_{LO}^2 - \omega^2}{\omega_{TO}^2 - \omega^2 - i\Gamma\omega}. \quad (3.25)$$

The  $-i\Gamma\omega$  complex term is added to account for the PhPs damping rate, attributed to the contribution of anharmonic mode oscillation. It results in lower PhPs lifetime [24].

#### Uniaxial materials

The permittivity seen by an electromagnetic field propagating inside a uniaxial material depends on the direction of the induced polarization, with  $\epsilon_{xx} = \epsilon_{yy} = \epsilon_\perp$  and  $\epsilon_{zz} = \epsilon_\parallel$ . As

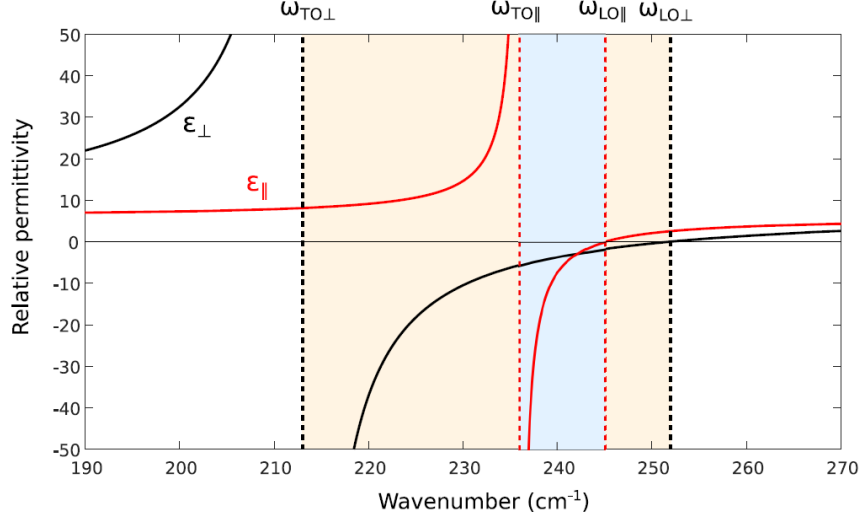


Figure 3.5 Permittivity of GaSe near polar phonon frequencies. The polar phonon frequencies are  $\omega_{TO,\perp} = 213.5 \text{ cm}^{-1}$ ,  $\omega_{TO,\parallel} = 236.5 \text{ cm}^{-1}$ ,  $\omega_{LO,\parallel} = 246.1 \text{ cm}^{-1}$  and  $\omega_{LO,\perp} = 253.3 \text{ cm}^{-1}$ . In orange are type-II hyperbolic regions ( $\epsilon_{\perp} < 0$  and  $\epsilon_{\parallel} > 0$ ). The blue region is the double Reststrahlen band ( $\epsilon_{\perp} < 0$  and  $\epsilon_{\parallel} < 0$ ). Reprinted with permission from Ref. [24] © 2020 Alaric Bergeron.

a result, the dispersion of PhPs in uniaxial materials depends on the propagation angle  $\theta$  between the wavevector  $\mathbf{k}$  and the crystal uniaxis.

As seen in the previous section, the TO and LO polar phonons from uniaxial crystals split into 2 distinct frequencies  $\omega_{TO,LO\perp}$  and  $\omega_{TO,LO\parallel}$  for polarization orthogonal and parallel to the crystal uniaxis. Eq.3.21 then separates into two independent equations, bringing two permittivity components  $\epsilon_{\perp}$  and  $\epsilon_{\parallel}$

$$\epsilon_{\perp}(\omega) = \epsilon_{\infty,\perp} \frac{\omega_{LO,\perp}^2 - \omega^2}{\omega_{TO,\perp}^2 - \omega^2 - i\Gamma_{\perp}\omega}, \quad \epsilon_{\parallel}(\omega) = \epsilon_{\infty,\parallel} \frac{\omega_{LO,\parallel}^2 - \omega^2}{\omega_{TO,\parallel}^2 - \omega^2 - i\Gamma_{\parallel}\omega}. \quad (3.26)$$

The permittivity of GaSe is shown in Fig. 3.5, with  $\epsilon_{\infty,\perp} = 5.76$  and  $\epsilon_{\infty,\parallel} = 7.44$  [24], and without damping ( $\Gamma_{\perp} = \Gamma_{\parallel} = 0 \text{ cm}^{-1}$ ). The type-II hyperbolic ( $\epsilon_{\perp} < 0$  and  $\epsilon_{\parallel} > 0$ ) frequency regions between  $\omega_{TO,\perp}$  and  $\omega_{TO,\parallel}$ , and  $\omega_{LO,\parallel}$  and  $\omega_{LO,\perp}$ , are displayed in orange. The blue region is the double Reststrahlen band ( $\epsilon_{\perp} < 0$  and  $\epsilon_{\parallel} < 0$ ) between the  $\omega_{TO,\parallel}$  and  $\omega_{LO,\parallel}$  frequencies.

Uniaxial crystals have a rotational symmetry around their uniaxis. A propagation restricted in the  $x - z$  plane is then assumed without loss of generality. The PhP wavevector is

decomposed into  $\mathbf{k} = k \sin(\theta)\hat{x} + k \cos(\theta)\hat{z}$  with  $\theta$  the angle between the PhPs wavevector and the crystal uniaxis. Plugging Eqs. 3.11 and 3.22 in the wave equation 3.13 leads to the set of equations [61]

$$\left[ \frac{c^2 k^2}{\omega^2} \cos^2(\theta) - \epsilon_{\perp}(\omega) \right] E_x - \frac{c^2 k^2}{\omega^2} \cos(\theta) \sin(\theta) E_z = 0 \quad (3.27a)$$

$$\left[ \frac{c^2 k^2}{\omega^2} - \epsilon_{\perp}(\omega) \right] E_y = 0 \quad (3.27b)$$

$$\left[ \frac{c^2 k^2}{\omega^2} \sin^2(\theta) - \epsilon_{\parallel}(\omega) \right] E_z - \frac{c^2 k^2}{\omega^2} \cos(\theta) \sin(\theta) E_x = 0. \quad (3.27c)$$

As can be seen, there always exists a transverse component both orthogonal to the plane of incidence (defined by  $\mathbf{k}$  and the crystal uniaxis, the latter coinciding with the optical axis) and  $\mathbf{k}$ . It corresponds to the  $E_y$  component and describes ordinary PhPs that possesses the same dielectric properties as transverse PhPs in isotropic materials.

The two other components  $E_x$  and  $E_z$  are coupled and parallel to the plane of incidence. They therefore describe extraordinary PhPs. They can be expressed in a longitudinal  $E_l$  and transverse  $E_t$  basis [61] such as

$$E_x = E_l \sin(\theta) - E_t \cos(\theta) \quad (3.28a)$$

$$E_z = E_l \cos(\theta) + E_t \sin(\theta). \quad (3.28b)$$

Replacing  $E_x$  and  $E_z$  into Eq. 3.27 leads to

$$\epsilon_{\perp}(\omega) \sin(\theta) E_l - \left[ \epsilon_{\perp}(\omega) - \frac{c^2 k^2}{\omega^2} \right] \cos(\theta) E_t = 0, \quad (3.29a)$$

$$\epsilon_{\parallel}(\omega) \cos(\theta) E_l - \left[ \epsilon_{\parallel}(\omega) - \frac{c^2 k^2}{\omega^2} \right] \sin(\theta) E_t = 0. \quad (3.29b)$$

Considering non-zero field amplitudes, the dispersion relation can be written as a 2x2 determinant that must vanishes

$$\begin{vmatrix} \epsilon_{\perp}(\omega) \sin(\theta) & \left[ \epsilon_{\perp}(\omega) - \frac{c^2 k^2}{\omega^2} \right] \cos(\theta) \\ \epsilon_{\parallel}(\omega) \cos(\theta) & \left[ \epsilon_{\parallel}(\omega) - \frac{c^2 k^2}{\omega^2} \right] \sin(\theta) \end{vmatrix} = 0. \quad (3.30)$$

Finally, the angle dependent dispersion of extraordinary PhPs is [60]

$$\epsilon(\omega, \theta) = \frac{\epsilon_{\perp}(\omega) \epsilon_{\parallel}(\omega)}{\epsilon_{\perp}(\omega) \sin^2(\theta) + \epsilon_{\parallel}(\omega) \cos^2(\theta)}, \quad (3.31)$$

in which the propagation of PhPs in an isotropic material is retrieved by considering  $\epsilon_{\perp} = \epsilon_{\parallel}$ . Extraordinary PhPs in a uniaxial material have a mixed longitudinal and transverse nature, whose dispersions cannot be analytically decoupled.

PhPs propagating in infinite crystals can be decomposed in a basis of 3 normal coordinates: a transverse ordinary (To) described by  $E_y$ , a transverse extraordinary (Te) described by  $E_t$ , and a longitudinal extraordinary (Le) described by  $E_l$ . These 3 components experience different permittivities and have distinct dispersion branches as a result.

### Phonon-polaritons dispersion in a infinite GaSe crystal

The dispersion of PhPs in an infinite GaSe crystal is shown Fig. 3.6 for an internal propagation angle of  $\theta = 45^\circ$ . The solid blue curve is the dispersion of the To mode  $\sqrt{\epsilon_{\perp}(\omega)} = ck/\omega$ , calculated from Eq. 3.26, independent of the propagation angle. The solid green and brown curves are the dispersion of Te and Le modes  $\sqrt{\epsilon(\omega)} = ck/\omega$ , with  $\epsilon(\omega)$  calculated from Eq. 3.31. The prefixes "L" and "U" denote the lower (low-frequency) and upper (high-frequency) branches. Since an infinite crystal is considered, no mode exists in the double Reststrahlen band between the  $\omega_{TO,\parallel}$  and  $\omega_{LO,\parallel}$  phonon frequencies where only surface modes can propagate.

Regions with non-zero second derivative are dispersion domains where PhPs have the highest mixed electromagnetic and phononic nature. As can be seen in Fig. 3.6, the amplitude of the PhPs wavevectors in the dispersion anti-crossing region is around  $10^4 \text{ cm}^{-1}$ . Light in the visible spectral range ( $k_0 \sim 10^5 \text{ cm}^{-1}$  at 532 nm) has therefore enough momentum to probe such a dispersion. On the contrary, dispersion domains with zero second derivative (linear dispersion regions) are regions of the dispersion where PhPs have more electromagnetic nature (at low wavevectors), or more phononic nature (at high wavevectors).

The LTe and Le branches extrapolate to a limit frequency of 228.3 and 248.1  $\text{cm}^{-1}$  for high wavevectors, respectively. These frequencies are extraordinary polar phonon frequencies expressed in the new transverse and longitudinal basis. The polar phonons frequencies of GaSe

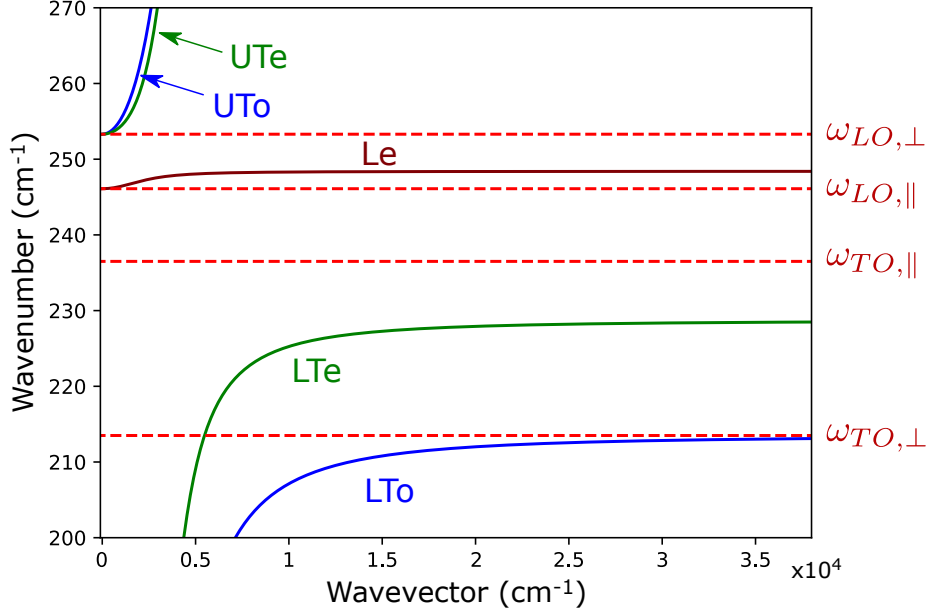


Figure 3.6 PhPs dispersion in a infinite GaSe crystal at an incidence angle of  $45^\circ$ . The dispersion is composed of 3 branches : transverse ordinary (To) in blue, transverse extraordinary (Te) in green and longitudinal extraordinary (Le) in brown. The prefixes "L" and "U" of the To and Te modes denote for lower and upper branches, respectively. The horizontal dashed lines are the frequencies of GaSe polar phonons.

returned by Eq. 3.7 at an angle of  $45^\circ$  are  $225.3 \text{ cm}^{-1}$  for the Te and  $249.7 \text{ cm}^{-1}$  for the Le polar phonons. This small discrepancy is attributed to the assumptions made in order to derive Eq. 3.7, extensively discussed in Ref. [60].

The next section discusses the theory of Raman spectroscopy by phonon and PhPs from GaSe, and demonstrates the capability of this technique for probing the dispersion of PhPs using visible light.

### 3.3 Raman scattering by phonon-polaritons

PhPs are infrared excitations that cannot couple to vacuum photons due to their high momentum mismatch. Near-field techniques presented in Sec. 2.2, where a tip generates high-k light components, are then used to probe PhP dispersions. Raman scattering uses visible light to probe infrared excitations. This work aims to show that it is also a convenient means to probe PhPs.

This section discusses the theory of Raman scattering from phonons and PhPs in GaSe. It presents the derivation of the Raman tensors and the selection rules. Finally, the expressions of the Raman intensity in infinite and thin film crystals are overviewed. They can be used

to compute PhPs Raman spectra and dispersion.

### 3.3.1 Raman scattering by phonons

Raman scattering, discovered in 1928 by *C.V. Raman*, is an inelastic scattering process enabling the probing of infrared excitations using visible light. Upon applying an electromagnetic field to a polarizable material, protons and electrons experience opposite Lorentz force, creating electric dipole moments. The total electric dipole moment per unit volume is called the polarization density  $\mathbf{P}$ , and is for weak fields linked to the applied electric field  $\mathbf{E}$  by the susceptibility tensor  $\overset{\leftrightarrow}{\chi}$ ,

$$\mathbf{P} = \epsilon_0 \overset{\leftrightarrow}{\chi} \mathbf{E}. \quad (3.32)$$

In the presence of lattice oscillations, the susceptibility is dynamically modulated. To a first order, the susceptibility can be written as

$$\overset{\leftrightarrow}{\chi} = \overset{\leftrightarrow}{\chi}_0 + \sum_N \left( \frac{\partial \overset{\leftrightarrow}{\chi}}{\partial \mathbf{u}_N} \right)_{\mathbf{u}_N=0} \mathbf{u}_N + \dots, \quad (3.33)$$

where  $\mathbf{u}_N$  is the crystal lattice displacement from its equilibrium, induced by the propagation of a phonon mode  $N$ , and  $\overset{\leftrightarrow}{\chi}_0$  is the non-modulated susceptibility. The Raman tensor of the vibrational mode  $N$  is defined as  $\overset{\leftrightarrow}{R}_N = \left( \frac{\partial \overset{\leftrightarrow}{\chi}}{\partial \mathbf{u}_N} \right)_{\mathbf{u}_N=0}$  [62].

Considering an electromagnetic field of frequency  $\omega$  and a phonon of frequency  $\omega_N$ , the polarization density  $\mathbf{P}$  is composed of 3 harmonic terms at frequencies  $\omega$ ,  $\omega - \omega_N$  and  $\omega + \omega_N$ . The scattered field  $\mathbf{E}_{scat} \propto \mathbf{P}$  is then composed of a field with the same frequency as the initial field  $\omega$  (*Rayleigh* signal) and two other fields at new frequencies  $\omega \pm \omega_N$  (*Raman* signals). The one with a lower frequency corresponds to the Stokes configuration and denotes the emission of a phonon inside the material. The other with a higher energy corresponds to the anti-Stokes configuration, and describes the absorption of a phonon. By energy conservation, the frequency  $\omega_N$  of the absorbed or emitted phonon can be extracted experimentally by measuring the frequency of the scattered field  $\mathbf{E}_{scat}$ .

Fig. 3.7 shows the energy diagram of a semi-conductor material along with the electron transitions involved in Rayleigh and Raman (resonant and non-resonant) light scattering processes. Only Raman scattering in the Stokes configuration is presented.

For every scattering processes studied, an absorption event of a photon having an energy of  $\omega$  promotes an electron from the valence band to a virtual level inside the conduction band.

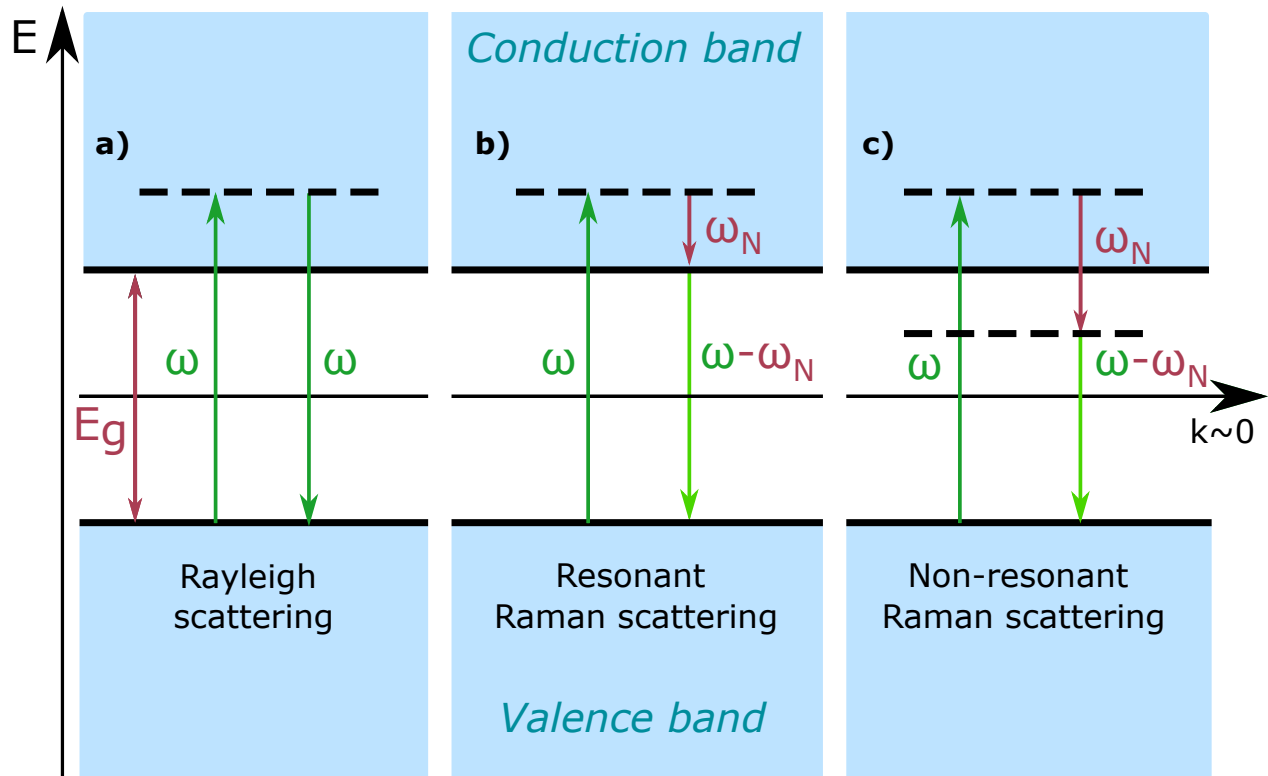


Figure 3.7 Light scattering energy diagram from a semi-conductor material. Dashed horizontal lines are virtual levels, having a lifetime of few femtoseconds. Upward arrows correspond an absorption event, and downward arrows to an emission event. 3 cases of light scattering processes are presented: **a)** Rayleigh scattering ; **b)** Resonant Raman scattering ; **c)** Non-resonant Raman scattering. Only the Stokes configuration of Raman scattering is shown. These processes are discussed in the text. The upper and the lower blue regions are the conduction and valence bands, respectively. They are separated by the band-gap energy  $E_g$ .  $\omega$  corresponds to the energy of a photon, while  $\omega_N$  to the energy of a phonon. Due to the low momentum of light compared to phonons, only transitions near the center of the Brillouin zone are considered ( $k \sim 0$ ).

These virtual levels are depicted by dashed horizontal lines in the figure. They are located far from a real energy level and have a very short lifetime of few femtoseconds due to the Heisenberg uncertainty<sup>1</sup>.

Fig. 3.7 **a)** describes the elastic Rayleigh scattering. Quasi-instantaneously after being promoted to a virtual level, the electron transitions back to the valence band by emitting a new photon at the same frequency as the initial photon. Fig. 3.7 **b-c)** describe the inelastic Raman scattering process. Within the short lifetime of the virtual state, the promoted electron can relax to a lower energy level by emitting a phonon with a frequency  $\omega_N$ . In resonance, the energy of the phonon enables the electron to relax to a real state in the conduction band, as can be seen in Fig. 3.7 **b)**. Most of the time, the electron relaxes to another virtual level as shown in Fig. 3.7 **c)**. Finally, the electron relaxes to the valence band by emitting a photon of lower energy  $\omega - \omega_N$  than the incident photon.

As the conduction band is a real energy level, Raman scattering is more efficient in resonance compared to the non-resonant Raman. However, as Raman scattering requires the interaction of a promoted electron with a phonon on a very short timescale, it remains less probable than Rayleigh scattering that only involves the relaxation of one electron. As a result, light scattered from Raman is generally a low efficiency process.

During the Raman scattering process, energy and momentum must be conserved. These conservation rules yields

$$\omega_s = \omega_i \pm \omega_N \quad (3.34)$$

$$\mathbf{k}_s = \mathbf{k}_i - \mathbf{q}_N, \quad (3.35)$$

with  $\omega_{i,s}$  and  $\mathbf{k}_{i,s}$  respectively the frequency and the wavevector of the incident (subscript -i) and scattered (subscript -s) photon, and  $\mathbf{q}_N$  the wavevector of the emitted or absorbed phonon.

For visible light around 532 nm, the initial and the scattered photons have a wavevector of amplitude  $k_0 \sim 1.2 \times 10^5 \text{ cm}^{-1}$ . In backscattering configuration, the wavevectors of the initial and the scattered photons are nearly collinear with opposite directions. The probed phonon wavevector amplitude is then in the order of  $2 \times k_0 \sim 2.4 \times 10^5 \text{ cm}^{-1}$ , approximately 0.3% of the Brillouin zone ( $\sim 8.4 \times 10^7 \text{ cm}^{-1}$  for GaSe [63]). As a result, no phonon dispersion can be measured using Raman spectroscopy, and the wavevectors of the probed phonons are

---

<sup>1</sup>For comparison, real energy levels have lifetime on the order of nanoseconds and more.

very close to zero relatively to the size of the Brillouin zone.

### GaSe phonon modes and selection rules

The number of phonon modes allowed in Raman scattering, along with their symmetry, is derived next for GaSe. In this discussion, only group theory is applied, and the Raman tensor of each mode is presented.

$\epsilon$ -GaSe is a non-centrosymmetric uniaxial crystal that belongs to the  $D_{3h}$  space group. With 8 atoms per unit cell, it has 24 normal modes of vibration (3 acoustic and 21 optical) [64]. These normal modes transform as  $\Gamma = 4(A'_1 + A'_2 + E' + E'')$  <sup>2</sup> [65, 66]. One acoustic mode has a  $A''_2$  symmetry and the two other, degenerate, have a  $E'$  symmetry.

Due to the  $x - y$  plane symmetry of uniaxial crystals, the two dimensional  $E'$  and  $E''$  modes are two-fold degenerate. Moreover, from the 24 normal modes, half are *Davydov* doublets. There are therefore 12 pairs of normal modes with atoms of top and bottom layers oscillating whether in phase or out of phase [67]. These pairs of modes are also degenerate due to the weak interlayer interaction in GaSe crystals [67, 68].

The list of non degenerate optical phonon modes, including their atomic displacement and their energy, are presented in Table S1. The listed frequencies are averaged values found in the literature, summarized in Table S2.

From the character table presented in Table S3 [64, 66], the Raman tensor representation is  $\Gamma(\overset{\leftrightarrow}{R}) = 2A'_1 + E' + E''$ . For a transition to be allowed in Raman, the integral  $\langle \Psi_{ini} | \overset{\leftrightarrow}{R} | \Psi_{fin} \rangle$  must be non-zero. This matrix element therefore needs to include a fully symmetric  $A'_1$  component, leading to the selection rule

$$\Gamma(\Psi_{ini}) \otimes \Gamma(\overset{\leftrightarrow}{R}) \otimes \Gamma(\Psi_{fin}) \supset A'_1, \quad (3.36)$$

where  $\Gamma(\Psi_{ini})$  and  $\Gamma(\Psi_{fin})$  are the symmetry of the initial and the final vibrational state. The initial state is the ground state, therefore totally symmetric ( $\Gamma(\Psi_{ini}) = A'_1$ ). Moreover, only first order transitions are considered. As a result, for a Raman transition to be allowed, the symmetry of the final state must satisfy

$$A'_1 \otimes (2A'_1 + E' + E'') \otimes \Gamma(\Psi_{fin}) \supset A'_1. \quad (3.37)$$

Using the character table of Table S3, vibrational mode with symmetry  $\Gamma(\Psi_{fin}) = A'_1, E'$

---

<sup>2</sup>Mulliken's symbols are used to assign the symmetry of the normal modes. [59].

and  $E''$  are allowed in Raman for crystals of the  $D_{3h}$  space group.

From the transformation properties of these modes presented in the  $D_{3h}$  character table [60,64], the Raman tensors are

$$\overset{\leftrightarrow}{R}_{A'_1} = \begin{pmatrix} a & 0 & 0 \\ 0 & a & 0 \\ 0 & 0 & b \end{pmatrix}, \quad \overset{\leftrightarrow}{R}_{A''_2}(z) = 0, \quad (3.38a)$$

$$\overset{\leftrightarrow(1)}{R}_{E'}(x) = \begin{pmatrix} 0 & c & 0 \\ c & 0 & 0 \\ 0 & 0 & 0 \end{pmatrix}, \quad \overset{\leftrightarrow(2)}{R}_{E'}(y) = \begin{pmatrix} c & 0 & 0 \\ 0 & -c & 0 \\ 0 & 0 & 0 \end{pmatrix}, \quad (3.38b)$$

$$\overset{\leftrightarrow(1)}{R}_{E''} = \begin{pmatrix} 0 & 0 & -d \\ 0 & 0 & 0 \\ -d & 0 & 0 \end{pmatrix}, \quad \overset{\leftrightarrow(2)}{R}_{E''} = \begin{pmatrix} 0 & 0 & 0 \\ 0 & 0 & d \\ 0 & d & 0 \end{pmatrix}, \quad (3.38c)$$

where  $a$ ,  $b$ ,  $c$  and  $d$  are constants, and  $x$ ,  $y$  and  $z$  the electric dipole orientation of polar modes.

The scattering intensity of a normal mode  $N$ , considering an infinite crystal, can be written as [60]

$$I_N = C |\hat{e}_i \cdot \overset{\leftrightarrow}{R}_N \cdot \hat{e}_s|^2. \quad (3.39)$$

$C$  is a constant,  $\hat{e}_i$  and  $\hat{e}_s$  the polarization of the incident and the scattered photon, and  $\overset{\leftrightarrow}{R}_N$  the Raman tensor of the normal mode  $N$ . This equation also defines the polarization selection rules of every Raman modes.

### 3.3.2 Raman scattering by polar phonons and phonon-polaritons

The electromagnetic field accompanying a polar excitation, arising from the oscillating electric dipole moments, also modulates the susceptibility of the material. This electro-optic modulation is described by a  $\chi^{(2)}$  process, and is therefore only present in non-centrosymmetric crystals. This contribution to the susceptibility gives, at first order,

$$\overset{\leftrightarrow}{\chi} = \overset{\leftrightarrow}{\chi}_0 + \sum_N \left( \frac{\partial \overset{\leftrightarrow}{\chi}}{\partial \mathbf{E}_N} \right)_{\mathbf{E}_N=0} \mathbf{E}_N + \dots \quad (3.40)$$

$\mathbf{E}_N$  is the electromagnetic field accompanying the polar excitation mode  $N$ , and  $\overset{\leftrightarrow}{\chi}_N^{(2)} = \left( \frac{\partial \overset{\leftrightarrow}{\chi}}{\partial \mathbf{E}_N} \right)_{\mathbf{E}_N=0}$  is its associated second order susceptibility.

Crystals of the  $D_{3h}$  space group have only 4 non-vanishing terms in their second order susceptibility tensor. They are linked by the relation  $\chi_{yyy} = -\chi_{yxx} = -\chi_{xxy} = -\chi_{xyx}$  [69]. In a contracted form<sup>3</sup>, the susceptibility tensors of GaSe then write as

$$\overset{\leftrightarrow}{\chi}_x^{(2)} = \begin{pmatrix} 0 & -\chi_{22} & 0 \\ -\chi_{22} & 0 & 0 \\ 0 & 0 & 0 \end{pmatrix}, \quad \overset{\leftrightarrow}{\chi}_y^{(2)} = \begin{pmatrix} -\chi_{22} & 0 & 0 \\ 0 & \chi_{22} & 0 \\ 0 & 0 & 0 \end{pmatrix}, \quad \overset{\leftrightarrow}{\chi}_z^{(2)} = 0. \quad (3.41)$$

The total variation of the susceptibility responsible for first order Raman scattering, including the contributions of the lattice motion and the electro-optic modulation, can be written using Eqs. 3.33 and 3.40 as [61]

$$\delta \overset{\leftrightarrow}{\chi} = \sum_N \left( \frac{\partial \overset{\leftrightarrow}{\chi}}{\partial \mathbf{u}_N} \right)_{\mathbf{u}_N=0} \mathbf{u}_N + \sum_N \left( \frac{\partial \overset{\leftrightarrow}{\chi}}{\partial \mathbf{E}_N} \right)_{\mathbf{E}_N=0} \mathbf{E}_N, \quad (3.42)$$

for any normal mode  $N$ . The relation between  $\mathbf{u}_N$  and  $\mathbf{E}_N$  defined in Eq. 3.18 leads to

$$\delta \overset{\leftrightarrow}{\chi} = \sum_N \left( \frac{e^*}{m} \frac{1}{(\omega_{TO,N}^2 - \omega^2)} \overset{\leftrightarrow}{R}_N + \overset{\leftrightarrow}{\chi}_N^{(2)} \right) \mathbf{E}_N, \quad (3.43)$$

where  $\overset{\leftrightarrow}{R}_N$  is the contribution of lattice oscillation defined in the last section.  $\omega_{TO,N} = \omega_{TO,\parallel}$  if the normal mode  $N$  has a A symmetry, and  $\omega_{TO,N} = \omega_{TO,\perp}$  if it has a E symmetry.  $\overset{\leftrightarrow}{\chi}_N^{(2)} = 0$  if  $N$  does not correspond to a polar mode. The total Raman tensor of the normal mode  $N$  therefore writes

$$\overset{\leftrightarrow}{R}_N^{tot} = \alpha_N \overset{\leftrightarrow}{R}_N + \overset{\leftrightarrow}{\chi}_N^{(2)}, \quad (3.44)$$

with  $\alpha_N = \frac{e^*}{m} \frac{1}{(\omega_{TO,N}^2 - \omega^2)}$ .

---

<sup>3</sup>Thanks to permutation symmetries in crystals, the notation  $\chi_{ijk}$  can be contracted into  $\chi_{il}$  using the following rules : the  $i$  subscript is replaced following  $x \rightarrow 1, y \rightarrow 2$  and  $z \rightarrow 3$ , the  $jk$  subscripts are replaced following  $xx \rightarrow 1 ; yy \rightarrow 2 ; zz \rightarrow 3 ; yz$  or  $zy \rightarrow 4 ; xz$  or  $zx \rightarrow 5 ; xy$  or  $yx \rightarrow 6$ . This is referred as the piezoelectric contraction in Ref. [69]

### Raman tensors in the phonon-polaritons normal coordinates

As seen in Sec. 3.2, the PhP normal coordinates form an orthogonal basis, in which it is more convenient to work. The wavevector of a PhP, once projected on the crystal axis coordinates, gives

$$\mathbf{q} = q(\sin(\theta) \cos(\phi), \sin(\theta) \sin(\phi), \cos(\theta)), \quad (3.45)$$

with  $\phi$  is the angle between  $\mathbf{q}$  and the x-axis and  $\theta$  between  $\mathbf{q}$  and the z-axis (parallel to the crystal uniaxis). The PhP coordinates are defined as  $\hat{T}o \perp (\hat{z}, \mathbf{q})$ ,  $\hat{T}e \perp (\hat{T}o, \mathbf{q})$  and  $\hat{L}e \parallel \mathbf{q}$ . The transformation matrix from the crystal coordinates to the PhP coordinates is [24]

$$T = \begin{pmatrix} -\sin(\phi) & \cos(\phi) & 0 \\ -\cos(\theta) \cos(\phi) & -\cos(\theta) \sin(\phi) & \sin(\theta) \\ \sin(\theta) \cos(\phi) & \sin(\theta) \sin(\phi) & \cos(\theta) \end{pmatrix}. \quad (3.46)$$

Upon applying the transformation

$$\begin{pmatrix} \overset{\leftrightarrow}{R}_{To}^{tot} \\ \overset{\leftrightarrow}{R}_{Te}^{tot} \\ \overset{\leftrightarrow}{R}_{Le}^{tot} \end{pmatrix} = T \begin{pmatrix} \overset{\leftrightarrow}{R}_x^{tot} \\ \overset{\leftrightarrow}{R}_y^{tot} \\ \overset{\leftrightarrow}{R}_z^{tot} \end{pmatrix}, \quad (3.47)$$

the Raman tensors expressed in the PhPs normal coordinates are

$$\overset{\leftrightarrow}{R}_{To}^{tot} = (\alpha_{\perp} c - \chi_{22}) \begin{pmatrix} \cos(\phi) & -\sin(\phi) & 0 \\ -\sin(\phi) & -\cos(\phi) & 0 \\ 0 & 0 & 0 \end{pmatrix}, \quad (3.48a)$$

$$\overset{\leftrightarrow}{R}_{Te}^{tot} = (\alpha_{\perp} c - \chi_{22} \cos(\theta)) \begin{pmatrix} -\sin(\phi) & -\cos(\phi) & 0 \\ -\cos(\phi) & \sin(\phi) & 0 \\ 0 & 0 & 0 \end{pmatrix}, \quad (3.48b)$$

$$\overset{\leftrightarrow}{R}_{Le}^{tot} = (\alpha_{\perp} c - \chi_{22} \sin(\theta)) \begin{pmatrix} \sin(\phi) & \cos(\phi) & 0 \\ \cos(\phi) & -\sin(\phi) & 0 \\ 0 & 0 & 0 \end{pmatrix}. \quad (3.48c)$$

## Raman conservation rules

The same energy and momentum conservation rules as for Raman scattering by phonons hold

$$\omega_s = \omega_i \pm \omega_{PhPs} \quad (3.49)$$

$$\mathbf{k}_s = \mathbf{k}_i - \mathbf{q}, \quad (3.50)$$

with  $\omega_{PhPs}$  and  $\mathbf{q}$  the energy and the wavevector of the emitted or absorbed PhPs. The probed wavevectors amplitude is in the range of  $k_i - k_s < q < k_i + k_s$ , and depends on the Raman scattering geometry considered. These geometries are shown in Fig. 3.8.

For near-forward scattering, the incident and the scattered photons travel in the same direction and therefore correspond to the left side of the inequality. The range of PhP wavevectors probed is between 0 and  $k_0 \sim 1.2 \times 10^5 \text{ cm}^{-1}$ , considering initial and scattered photons with a wavelength of 532 nm ( $\omega_{PhPs} \ll \omega_{i,s}$ ). It covers all the dispersion of PhPs from bulk GaSe crystals, as the dispersive region of PhPs is located between wavevectors of 0 and  $3 \times 10^4 \text{ cm}^{-1}$ , as can be seen in the PhPs dispersions displayed in Fig. 3.6. Therefore, Raman scattering in the near-forward configuration can probe the PhP dispersion from bulk GaSe.

In the backward geometry, the incident and the scattered photons propagate in opposite directions. It corresponds to the right side of the inequality and yields PhPs with higher wavevectors than in the near-forward geometry. The probed PhP wavevectors range between  $k_0$  and  $2 \times k_0 \sim 2.4 \times 10^5 \text{ cm}^{-1}$ . Therefore, no PhP dispersion can be measured in bulk GaSe crystals in this geometry.

For infinite crystals, the Raman intensity of a mode  $N$  including the lattice oscillation and the electro-optic contributions to the susceptibility modulation is

$$I_N = C \left| \hat{e}_i \cdot (\alpha_N \overset{\leftrightarrow}{R}_N + \overset{\leftrightarrow}{\chi}_N^{(2)}) \cdot \hat{e}_s \right|^2. \quad (3.51)$$

## Raman scattering intensity of phonon-polaritons from 2D materials

The case of a 2D material with infinite lateral and restricted vertical dimensions is now considered. The wavevector of a PhP propagating in such materials can be decomposed in terms of in-plane (subscript  $\parallel$ ) and out-of-plane (subscript  $\perp$ ) components. The out-of-plane component is collinear to the crystal uniaxial. Considering angle and frequency dependent re-

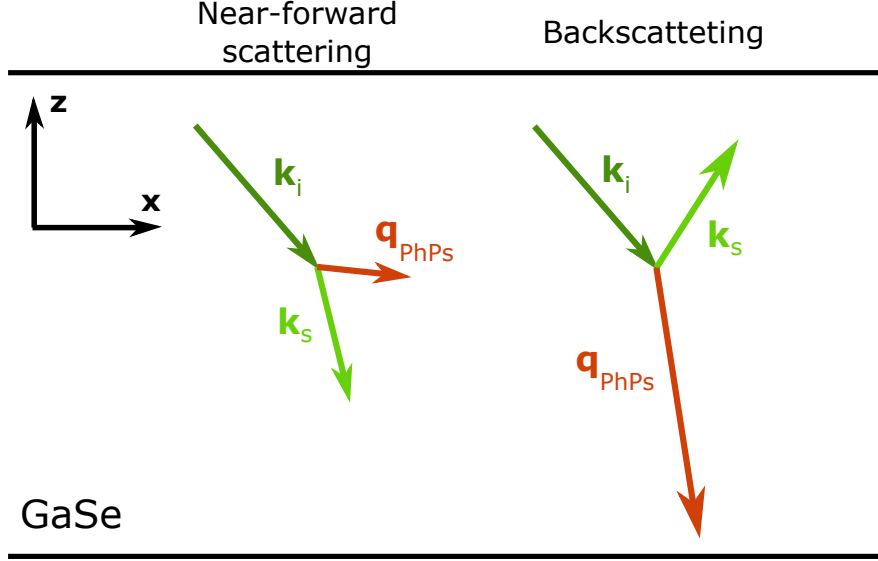


Figure 3.8 Near-forward and backscattering Raman geometries.  $\mathbf{k}_{i,s}$  is the wavevector of the incident (subscript -i) and the scattered (subscript -s) photon.  $\mathbf{q}_{PhPs}$  is the wavevector of the emitted PhPs.

fractive index  $n(\theta, \omega)$  of the crystal, the projected components from the conservation relation of Eq. 3.50 writes as

$$q_{\parallel} = 2\pi [n(\theta_i, \omega_i)\sigma_i \sin(\theta_i) - n(\theta_s, \omega_s)\sigma_s \sin(\theta_s)] \quad (3.52a)$$

$$q_{\perp} = 2\pi [n(\theta_i, \omega_i)\sigma_i \cos(\theta_i) - n(\theta_s, \omega_s)\sigma_s \cos(\theta_s)]. \quad (3.52b)$$

$\theta_{i,s}$  are the initial and scattered photon wavevector angles with respect to the crystal uniaxial and  $\sigma_{i,s} = 1/\lambda_{i,s}$  the wavenumber of the incident and the scattered photons.

*Mills, Chen and Burstein* proposed a general expression for the Raman scattering intensity of volume, guided, and surface PhPs in thin crystal films [70]. *Sasaki* and *Ushioda* adapted and simplified the writing of their result, leading to the following expression [38]

$$I_N = A \frac{n_{\omega_{PhPs}} + 1}{d} |(\hat{\mathbf{e}}_i \cdot \overset{\leftrightarrow}{R}_N \cdot \hat{\mathbf{e}}_s) \int_{-d/2}^{d/2} e^{i\Delta k_{\perp} z} \langle E_N(z) \rangle dz|^2 \delta(\Delta k_{\parallel} - q_{\parallel}) H_N^E(\omega, \theta), \quad (3.53)$$

where  $A$  is a constant,  $n_{\omega_{PhPs}}$  the Bose-Einstein occupation factor,  $d$  the thickness of the crystal, and  $\langle E_N(z) \rangle$  the time-averaged PhP electric field along the out-of-plane axis.  $\Delta k_{\perp} = k_{\perp,i} - k_{\perp,s}$  is the orthogonal wavevector difference between the incident and the scattered

photons, and  $\delta(\Delta k_{\parallel} - q_{\parallel})$  is the conservation rule on the in-plane wavevectors, with  $\Delta k_{\parallel} = k_{\parallel,i} - k_{\parallel,s}$ .  $H_N^E(\omega, \theta)$  is the Hopfield coefficient defining the electromagnetic portion of energy stored in the PhP, derived by *Irmer et. al.* [39] and added to the Raman intensity by *Bergeron* [24].

### Relaxed Raman conservation rules in thin crystals

As seen in Eq. 3.53, no wavevector conservation rule exists for the out-of-plane component. When the thickness of the crystal approaches the propagation length of a PhP ( $\sim 10 \mu\text{m}$  in thin hBN crystals [34]), its out-of-plane wavevector  $q_{\perp}$  is quantized by a multiple of  $\pi/d$ . This relaxes the wavevector selection rule on the out-of-plane component and PhPs modes with  $k_{\perp,i} - k_{\perp,s} \neq q_{\perp}$  become accessible [37, 71].

The range of PhP wavevectors accessible via Raman backscattering are only restricted by the in-plane component. Because PhPs weakly scatter visible light,  $\theta_i \sim \theta_s$  is assumed in the backscattering geometry [24]. Moreover, the parallel wavevector is conserved when the incident light is refracted from air to the GaSe crystal. Rewriting the conservation rule from Eq. 3.52b leads to

$$q_{\parallel} = 2\pi \sin(\theta_i) [2\sigma_i - \sigma_{PhPs}], \quad (3.54)$$

where  $\sigma_{PhPs}$  is the PhP wavenumber. Considering a PhP wavenumber of  $\sigma_{PhPs} = 240 \text{ cm}^{-1}$  and an excitation source at 532 nm, the range of accessible PhP wavevectors in the backscattering configuration is located between 0 and  $2 \times 10^5 \text{ cm}^{-1}$ . It makes the dispersion of PhPs from GaSe accessible with Raman backscattering.

### 3.4 Phonon-polaritons in 2D materials: numerical modeling

This section presents the numerical models used to compute PhP dispersion curves. An analytical solution for a symmetric waveguide is first presented. Then, a matrix formalism enabling PhP field calculations in a 1D-multilayer system is presented. PhP Raman spectra as a function of the PhP wavevector are computed, which allows the calculation of PhP dispersions. Finally, a model using the FEM was built to compute PhPs fields in a 2D geometry.

### 3.4.1 Symmetric waveguide model

The dispersion of PhPs propagating in a GaSe thin film suspended in air is presented next. The derivation was first made by *Sasaki* in Ref. [38], and *Bergeron* added methods to avoid numerical instabilities [24]. The waveguide transverse electric (TE) and transverse magnetic (TM) transcendental equations are presented, along with an example of calculated PhPs dispersion curves.

The geometry of the waveguide, composed of three layers, is presented in Fig. 3.9. The GaSe layer has a thickness  $d$  and an infinite width and depth. Thanks to the rotational symmetry around the crystal uniaxial (z-axis), the propagation of the PhP is assumed in the  $x - z$  plane without loss of generality. In each region, the PhP electric field writes as [24]

$$\mathbf{E}_1(\mathbf{r}, t) = \mathbf{E}_1^0 e^{iq_{z,1}z} e^{i(q_x x - \omega t)} \quad (3.55)$$

$$\mathbf{E}_2(\mathbf{r}, t) = \left( \mathbf{E}_2^{0+} e^{iq_{2,z}z} + \mathbf{E}_2^{0-} e^{-iq_{2,z}z} \right) e^{i(q_x x - \omega t)} \quad (3.56)$$

$$\mathbf{E}_3(\mathbf{r}, t) = \mathbf{E}_3^0 e^{iq_{z,3}z} e^{i(q_x x - \omega t)}. \quad (3.57)$$

$q_{\beta,j}$  is the projection of the PhP wavevector in the direction  $\beta = x, z$  and the region  $j = 1, 2, 3$ , and  $\mathbf{E}_j^0 = (E_{jx}^0, E_{jy}^0, E_{jz}^0)^T$  is the field amplitude in the region  $j$ . The + and - signs denote for the amplitude of the wave propagating in the same direction and in the opposite direction of the z-axis, respectively.

The continuity of the in-plane wavevector component writes  $q_{x1} = q_{x2} = q_{x3} = q_x$ . This component is always real since a propagative PhP is considered along the x-axis. The out-of-plane wavevector is however not continuous at interfaces. An evanescent wave is considered outside the GaSe slab, so imaginary out-of-plane wavevectors  $q_{z1} = i\alpha = -q_{z3}$  are considered in air (regions 1 and 3), where  $q_{z1} = \sqrt{\epsilon_{air}\omega^2/c^2 - q_x^2}$  and  $\epsilon_{air} \sim 1$ . Finally, a complex out-of-plane wavevector  $q_{z2}$  is assumed in the GaSe core to account for propagative and surface mode solutions. It corresponds to the real and the imaginary part of  $q_{z2}$ , respectively. The transcendental equations for TE and TM modes are [24]

$$\text{TE : } \tan(q_{z2}d) = \frac{2q_{z2}\alpha}{q_{z2}^2 - \alpha^2}, \quad q_{z2} = \sqrt{\epsilon_{\perp}(\omega^2/c^2) - q_x^2}, \quad (3.58)$$

$$\text{TM : } \tan(q_{z2}d) = \frac{2\epsilon_{\perp}q_{z2}\alpha}{q_{z2}^2 - \epsilon_{\perp}^2\alpha^2}, \quad q_{z2} = \sqrt{\epsilon_{\perp}(\omega^2/c^2) - (\epsilon_{\perp}/\epsilon_{\parallel})q_x^2}, \quad (3.59)$$

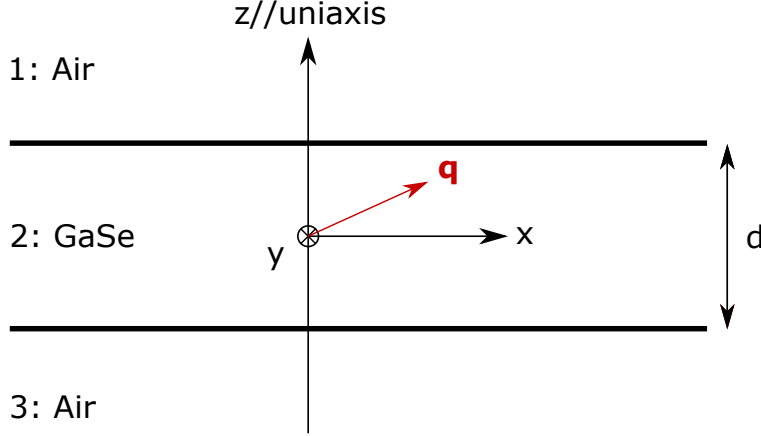


Figure 3.9 Geometry of the symmetric waveguide.  $\mathbf{q}$  is the wavevector of the propagating PhPs mode and  $d$  the thickness of the GaSe core.

where  $\epsilon_{\perp,\parallel}$  is the permittivity of GaSe.

TE solutions correspond to guided To waves, whose polarization exclusively sees the permittivity perpendicular to the crystal uniaxis,  $\epsilon_{\perp}$ . TM solutions describe Te and Le guided modes, in addition to the two surface modes arising from the two air/GaSe interfaces [38].

An example of dispersion curves obtained by solving the transcendental equations is presented in Fig. 3.10. It shows the dispersion of guided and surface PhP modes propagating in a  $1\ \mu\text{m}$  thick GaSe waveguide. An infinite number of guided modes exist in the waveguide, so only few branches are presented per mode. Since the modes propagate along the in-plane axis (x-axis), the dispersion is presented in terms of in-plane wavevector  $q_x$ . Wavevectors are displayed in a logarithmic scale to better visualize the rapid variation of the ordinary and surface branches at lower wavevectors, and the dispersion of the extraordinary modes at higher wavevectors. This calculated dispersion is compared with the dispersion of PhPs in an infinite GaSe crystal shown in Fig. 3.6.

By vertically confining PhPs, guided  $\text{To}_m$ ,  $\text{Te}_m$  and  $\text{Le}_m$  modes are quantized by their out-of-plane wavevector  $q_z$ . The total wavevector amplitude is given by  $q = \sqrt{q_x^2 + q_z^2}$ , where  $q_z = m \times \pi/d$  and  $m$  is a natural number.

As can be seen in Fig. 3.10, every PhP mode extrapolates to the dispersion of light at low wavevectors, due to the air playing the role of the waveguide cladding. The anti-crossing region of each fundamental mode ( $m = 1$ ) is located at higher wavevectors when compared to the PhPs dispersion in an infinite GaSe crystals. The dispersion of the  $\text{Le}_1$  is for example located between in-plane wavevectors  $q_x$  of  $10^4$  and  $10^5\ \text{cm}^{-1}$ . The PhPs wavevector amplitude  $q$  is therefore between  $3.3 \times 10^4$  and  $10^5\ \text{cm}^{-1}$ . This region was located around  $q = 3 \times 10^3$

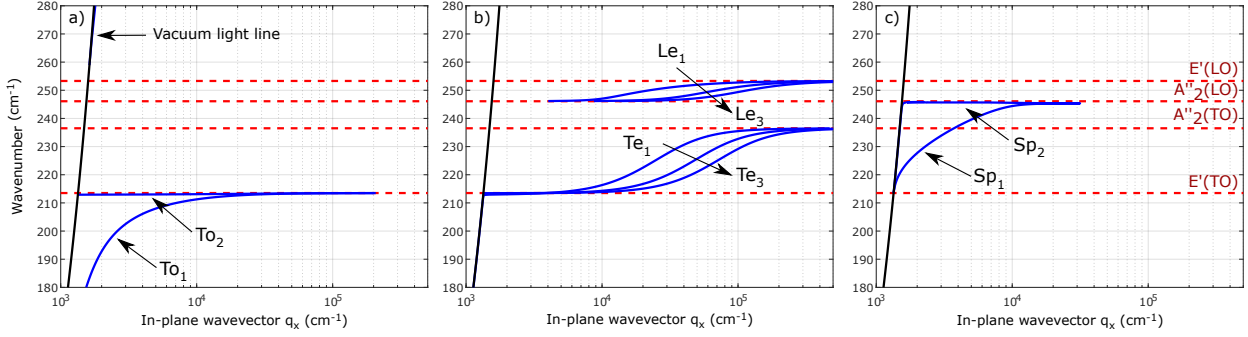


Figure 3.10 PhP ispersion curves in a 1  $\mu\text{m}$  thick GaSe waveguide suspended in air calculated with the analytical model. The dispersion is presented in terms of in-plane wavevector  $q_x$  and on a logarithmic scale. **a)** corresponds to TE solutions, while **b)** and **c)** are TM solutions.

$\text{cm}^{-1}$  in an infinite GaSe crystal as shown in Fig. 3.6, indicating that spatial confinement significantly increased the PhP wavevectors. Finally, the dispersion of every guided polariton mode extrapolates to polar phonon frequencies at higher wavevectors. These frequencies correspond to the polar phonon frequencies calculated with Eqs. 3.7 for a propagation angle of  $90^\circ$  with respect to the uniaxis.

From all guided modes, only the  $\text{Le}_m$  are of interest because the other are not observed experimentally. The  $\text{Le}_m$  lie in the type-II hyperbolic region between  $\text{A}''_2(\text{LO})$  and  $\text{E}'(\text{LO})$  phonon frequencies. They are transverse magnetic guided modes, with their electric field within the plane of incidence. At a fixed wavevector, the frequency of the  $m^{\text{th}}$  order mode decreases with increasing  $m$ .

The boundary conditions defined by the two air/GaSe interfaces of the waveguide enable the propagation of two surface modes, labeled  $\text{Sp}_{1,2}$ . They are of great interest because of their sensitivity to their dielectric environment. These modes are found between the  $\text{E}'(\text{TO})$  and the  $\text{A}''_2(\text{LO})$  phonon frequencies. They are located in a type-II hyperbolic frequency region between  $\text{E}'(\text{TO})$  and  $\text{A}''_2(\text{TO})$ , and in the double Reststrahlen band between  $\text{A}''_2(\text{TO})$  and  $\text{A}''_2(\text{LO})$  phonons. These surface modes are further discussed in Chapter 5.

### 3.4.2 4x4 matrix formalism

A 4x4 matrix formalism to calculate the distribution of the PhP electric field intensity in a multilayer system in 1D is utilized in Refs. [24, 72]. The model considers layers with infinite width and computes the evolution of the field components along the out-of-plane axis ( $z$ -axis) of a mode propagating in the  $x - z$  plane. Their article comes with a Matlab code in which the formalism is implemented. It was then adapted by *Bergeron* to compute PhPs

fields in a multilayer system containing a GaSe layer. Since no additional functionality was implemented during this work, an overview of this matrix formalism is presented next.

The algorithm uses a 4x4 matrix formalism based on Maxwell's equations. The electric field vector is composed of four components and is written as

$$\vec{E} = \begin{pmatrix} E_{trans}^p \\ E_{refl}^p \\ E_{trans}^s \\ E_{refl}^s \end{pmatrix}. \quad (3.60)$$

$E_{trans}^{p,s}$  and  $E_{refl}^{p,s}$  are the electric field amplitudes of the  $p,s$ -polarized transmitted and reflected field components. The index  $j$  is used to denote the layer number:  $j = 0$  corresponds to the incident material and  $j = N + 1$  stands for the substrate.  $N$  is the number of layers composing the system. The boundary conditions between the layers  $j - 1$  and  $j$  are encoded in a set of matrices  $\mathbf{A}$ ,

$$\mathbf{A}_{j-1} \vec{E}_{j-1} = \mathbf{A}_j \vec{E}_j. \quad (3.61)$$

The propagation matrix  $\mathbf{P}_j$  is defined to describe the propagation of each field component inside the layer  $j$

$$\mathbf{P}_j = \begin{pmatrix} e^{-ik_{j1}^z d_j} & 0 & 0 & 0 \\ 0 & e^{-ik_{j2}^z d_j} & 0 & 0 \\ 0 & 0 & e^{-ik_{j3}^z d_j} & 0 \\ 0 & 0 & 0 & e^{-ik_{j4}^z d_j} \end{pmatrix}, \quad (3.62)$$

where  $d_j$  is the thickness of the layer  $j$ .  $k_{j\beta}^z$  is the out-of-plane wavevector of the field component  $\beta = 1, 2, 3, 4$  from the vector  $\vec{E}$ . The transfer matrix  $\mathbf{T}_j$ , taking into account the boundary conditions and the propagation of the field inside the layer  $j$ , is defined as

$$\mathbf{T}_j = \mathbf{A}_j \mathbf{P}_j \mathbf{A}_j^{-1}. \quad (3.63)$$

The matrix  $\mathbf{T}_{tot}$  describing the propagation of a PhPs field through the  $N$  layers of the system therefore writes as the product

$$\mathbf{T}_{tot} = \prod_{j=1}^N \mathbf{T}_j. \quad (3.64)$$

Finally, boundary conditions imposed by the incident medium ( $j=0$ ) and the substrate ( $j=N+1$ ) are added, leading to the total transfer matrix

$$\mathbf{\Gamma}_N = \mathbf{A}_0 \mathbf{T}_{tot} \mathbf{A}_{N+1}. \quad (3.65)$$

The field from the incident medium can then be related to the field at the substrate by the simple relation

$$\vec{E}_0 = \mathbf{\Gamma}_N \vec{E}_{N+1}. \quad (3.66)$$

In order to obtain the field amplitude at any point in the structure, the z-axis is discretized and the propagation matrix of every layer  $j$  is divided into  $d_j/dz$  submatrices, where  $dz$  is the subdivision step. These submatrices are then consecutively applied to the field vector in order to evaluate the PhP field along the whole multilayer system.

From the total transfer matrix  $\mathbf{\Gamma}_N$ , the reflection and transmission coefficients of the multilayer system can be calculated. For instance, the  $r_{ss}$  and  $r_{pp}$  coefficients are given by [73]

$$r_{ss} = \frac{\Gamma'_{11}\Gamma'_{43} - \Gamma'_{41}\Gamma'_{13}}{\Gamma'_{11}\Gamma'_{33} - \Gamma'_{13}\Gamma'_{31}}, \quad r_{pp} = \frac{\Gamma'_{21}\Gamma'_{33} - \Gamma'_{23}\Gamma'_{31}}{\Gamma'_{11}\Gamma'_{33} - \Gamma'_{13}\Gamma'_{31}}. \quad (3.67)$$

Resonances of the imaginary part of  $r_{ss}$  and  $r_{pp}$  are respectively attributed to the presence of guided TE and TM modes propagating inside the multilayer system [24]. These coefficients can also be used to compute the dispersion of guided and surface PhPs modes inside the multilayer system.

### Phonon-polariton field in an asymmetric GaSe waveguide

In this work, samples are placed onto a silicon (Si) substrate with a 100 nm thick SiO<sub>2</sub> thermal oxide layer. Frequency dependent x and y polarization PhPs electric field intensity inside this multilayer system is presented in Fig. 3.11 for a GaSe thickness of 1  $\mu\text{m}$  and a PhPs in-plane wavevector of  $q_x = 2 \times 10^4 \text{ cm}^{-1}$ .

To better visualize fast variations of the PhP electric field, a logarithmic scale is used. It writes as

$$I_{log} = \frac{\log_{10}(1 + S \times I_{lin})}{\log_{10}(S)}, \quad (3.68)$$

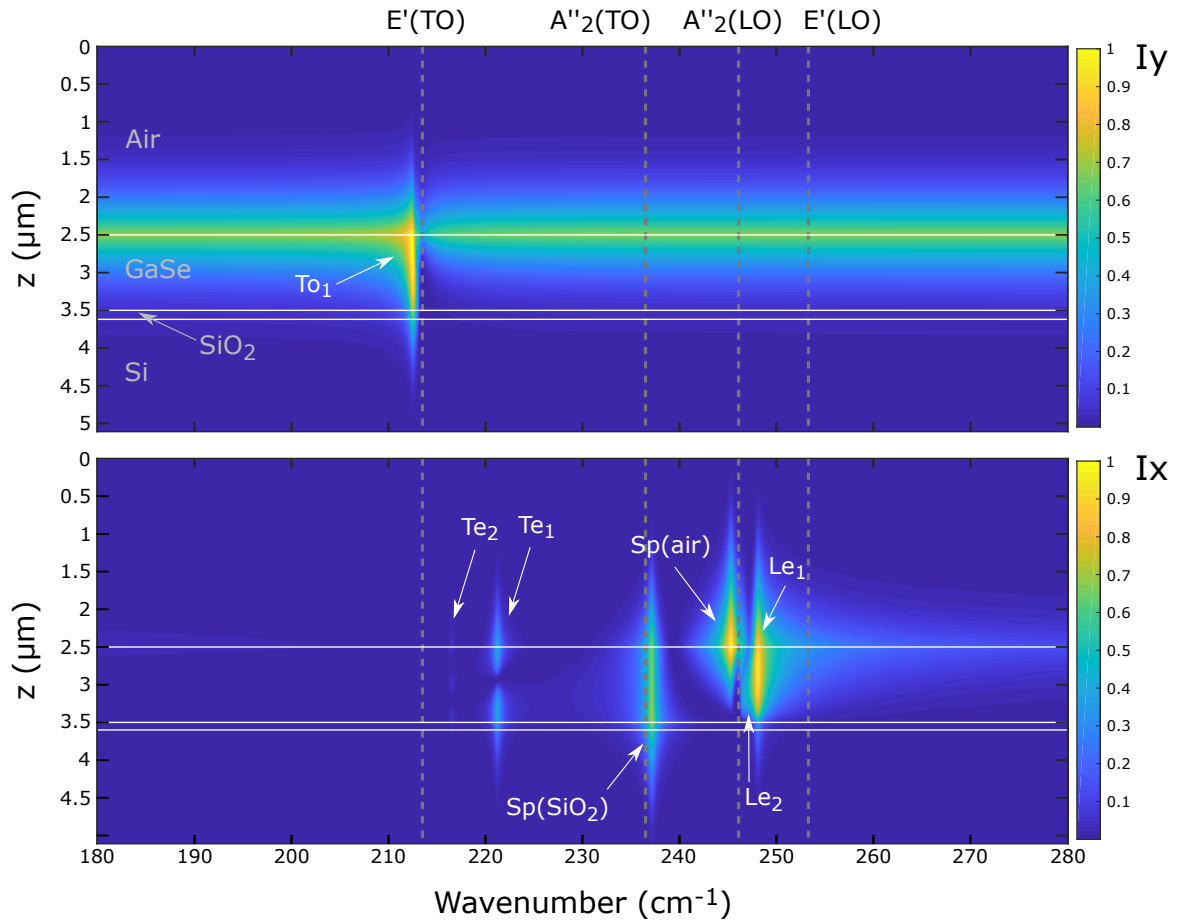


Figure 3.11 PhP electric field map intensity in an asymmetric waveguide as a function of the PhP frequency, for an in-plane wavevector of  $q_x = 2 \times 10^4 \text{ cm}^{-1}$ . The multilayer structure is composed, from top to bottom, of air/GaSe/SiO<sub>2</sub>/Si. The GaSe and the the SiO<sub>2</sub> layers have a thickness of 1  $\mu\text{m}$  and 100 nm, respectively. The color map has a logarithmic scale with a scaling factor of  $S = 10$ . The PhP electric field intensity is normalized by its maximum value.

where  $S$  is a scaling factor. In the numerator, this factor is used to artificially increase the order of magnitude of the computed field intensity, that can be as low as approximately  $10^{-2}$  a.u.. This locates the argument of the logarithm function in a region where its variation is slower than the one obtained with a linear scale. Adding 1 in the argument of the logarithm function prevents to have negative values at the output of the function. Finally, the denominator is a renormalization factor.

The permittivity of GaSe is calculated with Eq. 3.26, with a low broadening factor of  $\Gamma_{\perp} = \Gamma_{\parallel} = 0.5 \text{ cm}^{-1}$  to better separate the modes<sup>4</sup>. The permittivity of SiO<sub>2</sub> is interpolated for each frequency by using the data of Ref. [74]. Finally, the permittivity of Silicon is  $\epsilon_{Si} = 11.7$  in the frequency region of interest [75].

The upper panel of Fig. 3.11 shows the y polarization electric field intensity, which corresponds to the To PhP. Only the fundamental To<sub>1</sub> is visible at the considered wavevector, very close to the E'(TO) phonon. Its field is distributed through the whole GaSe slab, and extends approximately 1  $\mu\text{m}$  in the Si substrate and in the air. There is also a constant background at the air/GaSe interface that is frequency independent.

The bottom panel, depicting the x polarization polariton field intensity, shows extraordinary and surface PhPs. Two Te modes are visible. The fundamental Te<sub>1</sub> has one node in the middle of the GaSe slab, while the Te<sub>2</sub> has two. The fundamental Le<sub>1</sub> mode is also identified, along with the weaker Le<sub>2</sub> spotted between the A''<sub>2</sub>(LO) phonon and the Le<sub>1</sub> polariton. The spatial field distribution of these guided PhPs modes indicates that they are guided modes inside the GaSe slab.

As expected, two surface modes are found. From their spatial field distribution, they are labeled Sp(air) and Sp(SiO<sub>2</sub>). The Sp(air) is confined at the air/GaSe interface, and extends both in the air and in the GaSe slab. The Sp(SiO<sub>2</sub>) field is however not strictly confined to only one interface. It is located at both the air/GaSe and GaSe/SiO<sub>2</sub> interfaces, with a non-negligible field intensity inside the GaSe slab. Despite that, this mode is necessarily a surface mode as it is located inside the double Reststrahlen frequency region of GaSe.

These frequency dependent field maps can be combined with Eq. 3.53 to compute the associated Raman spectrum. By considering several wavevectors  $q_x$ , the Raman dispersion curve of PhPs can therefore be computed. It can be realized for any GaSe thickness, and more extensively for any multilayer system that supports PhPs.

---

<sup>4</sup> $\Gamma = 1.8 \text{ cm}^{-1}$  is usually used [24].

### 3.4.3 Finite element method model

The previous model is limited to one dimension. To improve the modeling of PhP propagating in thin GaSe waveguides, a FEM model was developed. It uses the commercial software COMSOL and computes the PhP wavevector and field distribution in two different 2D geometries. The two geometries are displayed in Fig. 3.12. As in the previous sections, PhPs are propagating along the x-axis and the uniaxis of the crystal is parallel to the z-axis.

The geometry of the symmetric waveguide, displayed in Fig 3.12 **a**), is the same as in Sec. 3.4.1. The dispersion calculated with this model can therefore be compared with the analytic solution. Continuous periodic conditions are set at the lateral edges of the model to simulate layers of infinite width. Scattering boundary conditions are set at the top and bottom of the geometry, with at least 100  $\mu\text{m}$  of air above and below the GaSe slab (not shown in Fig 3.12 for clarity). This prevents the upper and bottom boundaries to influence the calculated PhP field.

The geometry of the asymmetric waveguide corresponds to the one considered in Sec. 3.4.2. The same boundary conditions as in the symmetric geometry are considered. The Si layer thickness is set to 5  $\mu\text{m}$  to avoid reflection of the PhP at the Si/air interface which could influence the calculated field map.

#### Geometry discretization

The second step into a FEM modeling is the discretization of the model geometries. This discretization influences the quality of the computation, as a bad mesh can lead to false results. In this work, a triangular mesh is considered because of the simple geometry of the models. The most used mesh element quality metric is the skewness of the mesh element

$$Q = \min_{i=1,2,3} \left( 1 - \max \left( \frac{\theta_i - \theta_e}{180 - \theta_e}, \frac{\theta_e - \theta_i}{\theta_e} \right) \right). \quad (3.69)$$

$\theta_e$  is the angle that provides an equilateral mesh element, and  $\theta_i$  is the angle of the vertex  $i$  where  $i = 1, 2$  or  $3$ . A quality  $Q$  of 1 indicates that the mesh element is equilateral, providing the best computation results.

The number of mesh elements should also be controlled to provide enough resolution and reasonable computation time for the modeled problem. It is controlled by the maximum element size allowed in each domain. With  $h_i$  the thickness of the layer  $i$ , the maximum element size is set to  $h_{\text{GaSe}}/25$  for GaSe,  $h_{\text{Si}}/15$  for Si, and  $h_{\text{SiO}_2}/15$  for the thermal oxide. A maximum element size of 0.5  $\mu\text{m}$  is chosen in the air domains to have at least 4 mesh

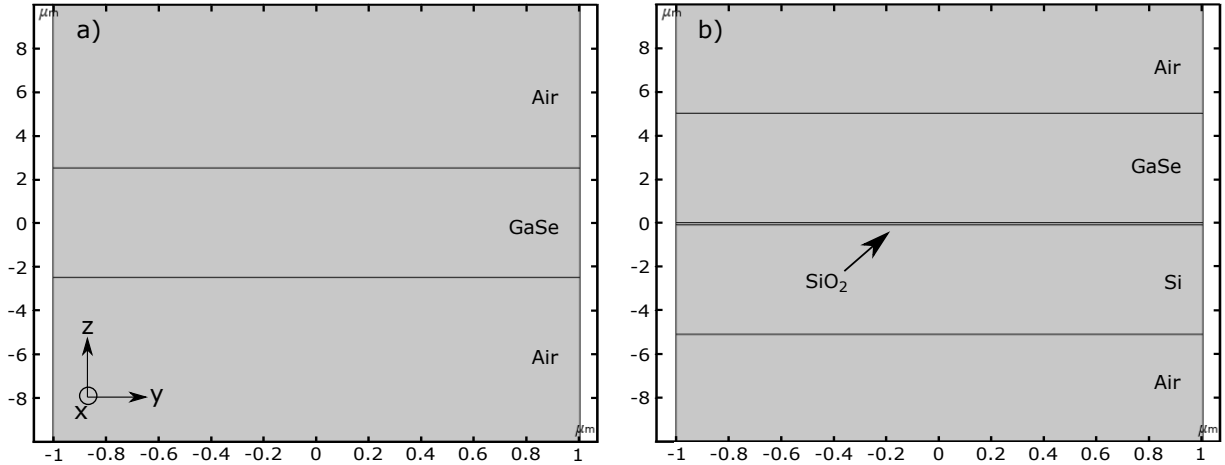


Figure 3.12 Geometry of the **a)** symmetric and **b)** asymmetric waveguide of the FEM model. The width of the two geometries is set to  $2\mu\text{m}$ . The Si layer has a thickness of  $5\mu\text{m}$ , and the  $\text{SiO}_2$  layer has a thickness of  $100\text{nm}$ . The bottom and top air layers extend to at least  $100\mu\text{m}$  away from the waveguide. In this case, a  $5\mu\text{m}$  thick GaSe layer is considered.

elements along the width of the geometry. The spatial variation of the field is indeed low in these domains, so larger mesh elements are considered to reduce the computation time.

An example of geometry discretization is shown in Fig. 3.13. The color scale depicts the quality of each mesh element calculated with Eq. 3.69. Good quality elements are depicted in green, whereas bad quality elements are shown in red. As can be seen, the mesh is regular and of good quality when far from domain frontiers. However, when approaching these frontiers, the element quality worsens due to the progressive change in element size. Since these regions are often rich in boundary conditions, the element quality should be well controlled to compute satisfying results.

To evaluate the quality of the generated mesh, bar charts of the elements quality are shown in Fig. 3.14. As can be seen, the average mesh elements quality of the two geometries is very close. There is no general rule on the sufficient mesh quality required for a FEM calculation, as it depends on too many aspects of the model and on the user's needs. For this work, the obtained average mesh element quality is sufficient. It is shown next by comparing the calculated PhP dispersion with the analytical solution, and by analyzing PhP field maps.

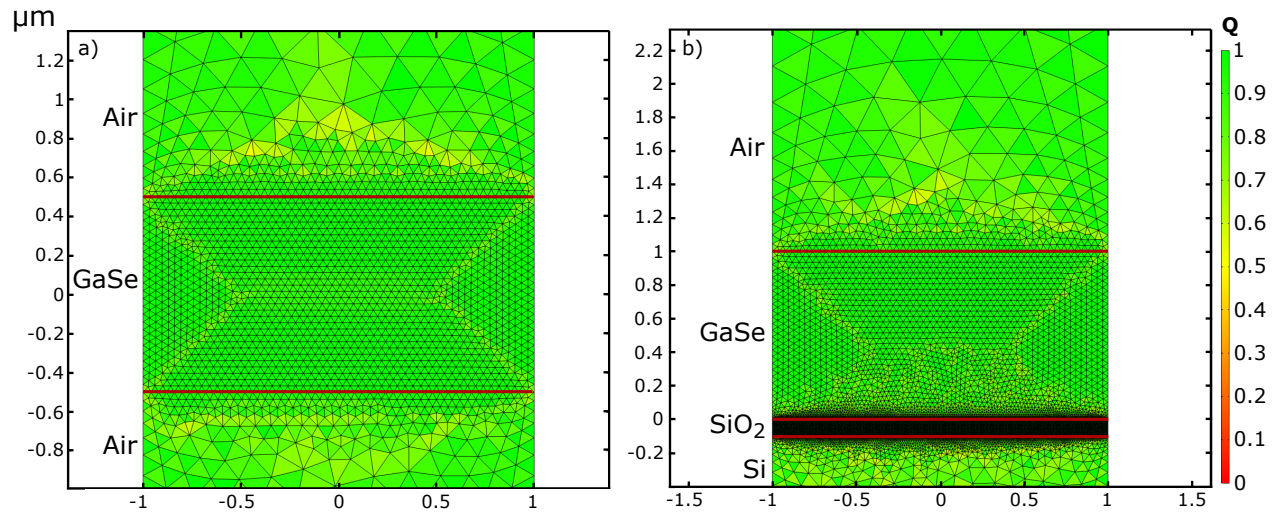


Figure 3.13 Mesh elements quality of the **a)** symmetric and **b)** asymmetric waveguide. The horizontal red lines depict the real position of the frontiers between domains. The density of mesh elements in the  $\text{SiO}_2$  domain prevents the visualization of the the color map to be visible.

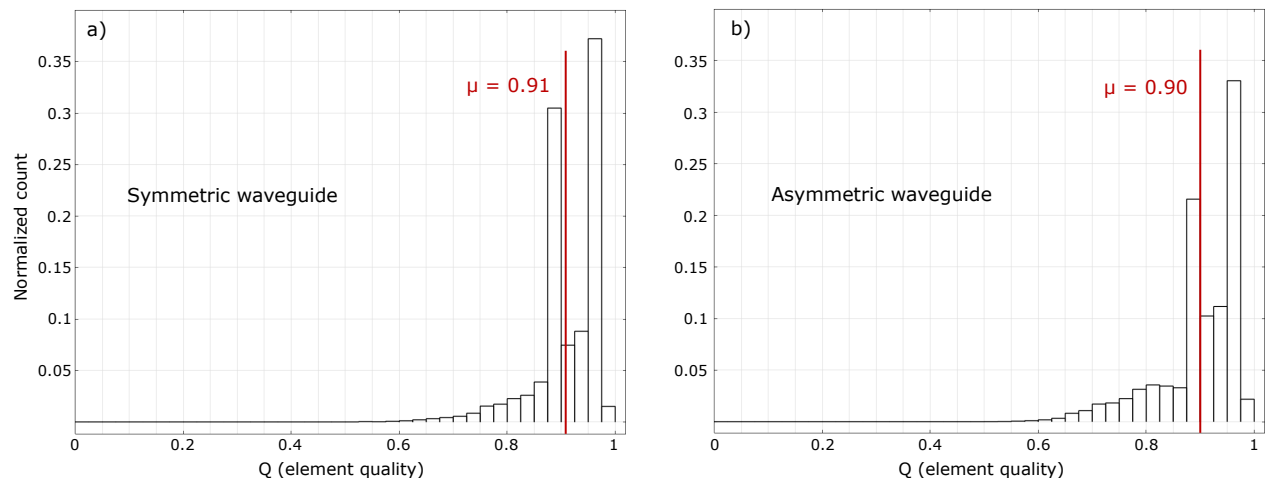


Figure 3.14 Elements quality bar charts of the **a)** symmetric and **b)** asymmetric waveguide meshes.  $\mu$  is the average element quality. Bin size is 0.025.

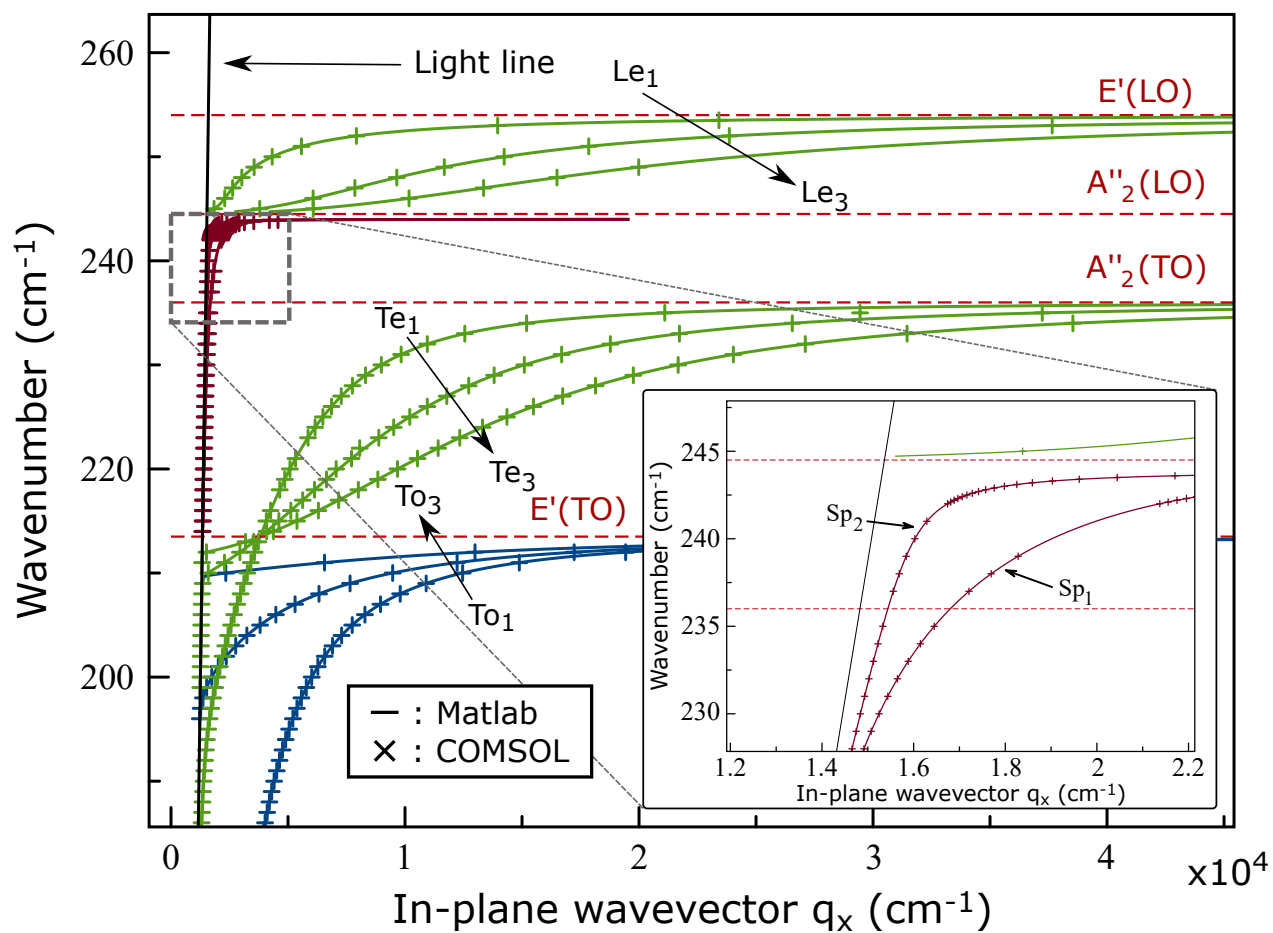


Figure 3.15 Comparison between the analytic (solid lines) and finite element calculation (crosses) of the PhPs dispersion. The solid black line is the dispersion of light in vacuum. The inset zooms onto the dispersion of surface modes.

## Comparison of the phonon-polaritons dispersion between the FEM and analytic models

In the FEM model, the frequency of the PhP is fixed and its associated in-plane wavevector  $q_x$  is returned by approximating the eigenvalues of the wave equation. To assess the quality of the FEM model, the PhP dispersion from a GaSe slab suspended in air is compared with the analytical solution presented in Sec. 3.4.1.

The results are presented in Fig. 3.15 for a 5  $\mu\text{m}$  thick GaSe waveguide. The solid curves show the analytical solution and the crosses show the in-plane wavevectors returned by the FEM model at a given frequency. The ordinary, extraordinary, and surface PhPs modes are depicted in blue, green, and brown, respectively. The inset zooms onto the two surface modes close to the light line. As can be seen, there is a perfect agreement between both calculation strategies.

However, the PhP dispersion calculation with the FEM model is cumbersome. The software returns many wavevectors that respect the fixed tolerance, and the correct wavevector must be found manually by looking at its associated field map. This approach is therefore not used to compute the dispersion of PhPs, but it remains relevant for calculating PhP field maps.

### Polariton field maps

Electric field distributions of  $\text{Le}_m$  PhP modes propagating along the x-axis in the asymmetric waveguide are shown in Fig. 3.16. They are calculated for a 1  $\mu\text{m}$  thick GaSe slab and for a polariton frequency of  $250 \text{ cm}^{-1}$ . The  $E_x$  field component of the three first Le modes is displayed. They are found at in-plane wavevectors  $q_x$  of  $3.3 \times 10^4 \text{ cm}^{-1}$  for the  $\text{Le}_1$ ,  $8.0 \times 10^4 \text{ cm}^{-1}$  for the  $\text{Le}_2$  and  $1.3 \times 10^5 \text{ cm}^{-1}$  for the  $\text{Le}_3$ .

As can be seen, these modes are guided in the GaSe slab with a very low field intensity outside the slab. The asymmetry of the waveguide induces a slight asymmetry in the spatial field distribution. Moreover, the quantization of the out-of-plane wavevector  $q_z$  is visible with the field nodes along the z-axis in the  $\text{Le}_2$  and  $\text{Le}_3$  field distributions. Finally, since the layers have infinite widths, the field intensity is constant along the y-axis.

The FEM model was initially developed to study horizontal confinement of PhPs. Some difficulties however appeared, such as non-physical field map distributions when reducing the waveguide dimensions. Despite contacting the software support, no solution to overcome these problems has been found yet. No computational method is then available to model horizontal confinement of PhPs for the moment. This could be combined with vertically confined PhPs models to study PhPs guided in 1D waveguides.

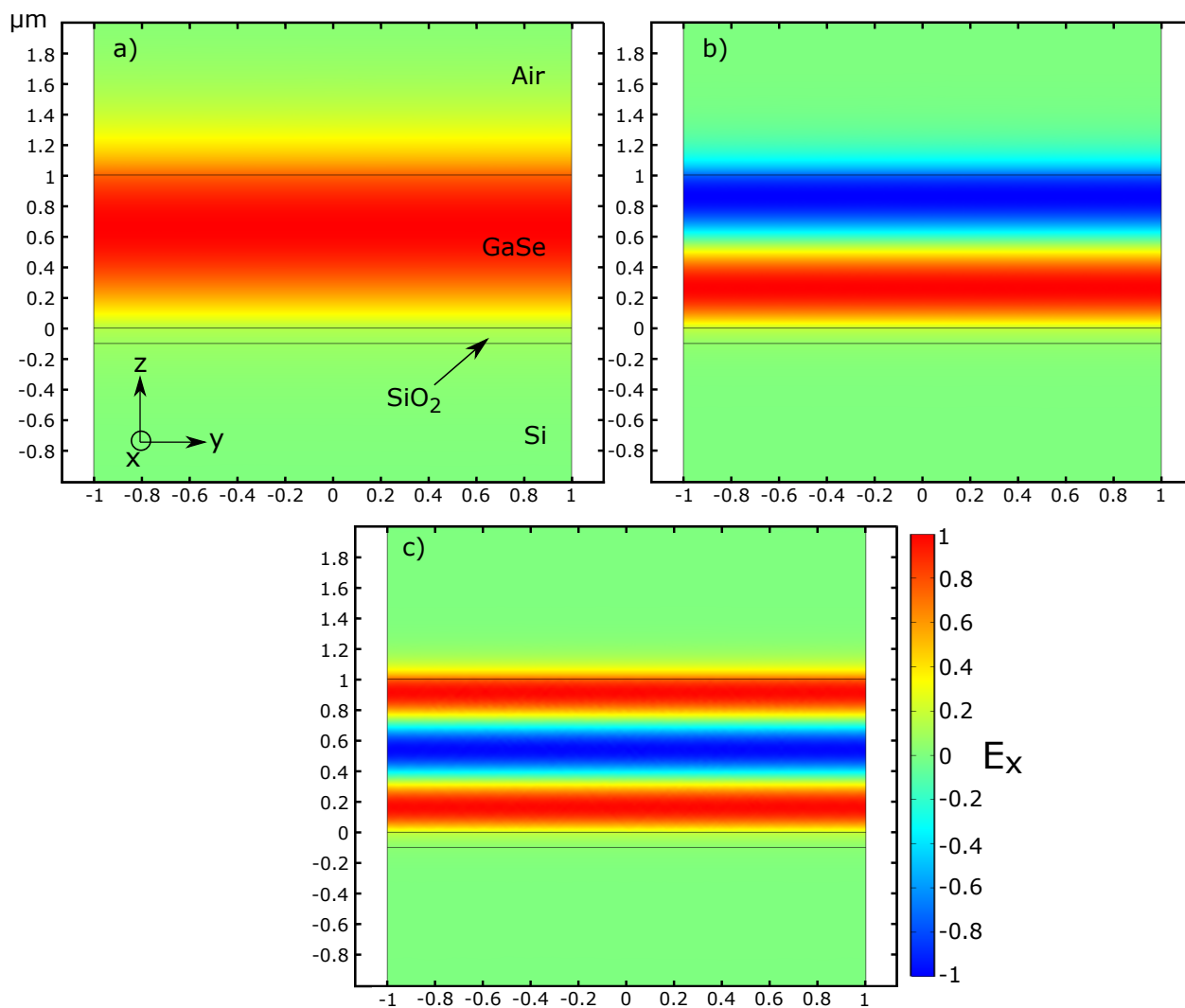


Figure 3.16 Spatial field distribution of a PhP propagating along the x-axis in the asymmetric waveguide with a 1  $\mu\text{m}$  thick GaSe slab. The PhP has a frequency of  $250\text{ cm}^{-1}$ . The PhP modes displayed are the **a)**  $\text{Le}_1$ , **b)**  $\text{Le}_2$ , and **c)**  $\text{Le}_3$ . The color bar corresponds to the PhP normalized  $E_x$  field component.

## CHAPTER 4 SAMPLE FABRICATION AND RAMAN SETUP

In this work, Raman scattering is used to study PhPs from thin GaSe samples. This chapter presents all the experimental aspects relating to this thesis. The first section discusses the production of thin GaSe samples, along with the characterization of their size. The second presents the Raman experimental setup and the processing of raw spectral data.

### 4.1 Sample preparation and characterization

The weak interlayer bonding of GaSe crystals is exploited to produce thin samples using mechanical exfoliation. An emphasis is put on the protection of samples against oxidation and external contaminations. Sample dimensions are measured by optical and atomic force microscopy.

#### 4.1.1 Mechanical exfoliation

Van der Waals crystals are layered materials where covalent bonds between atoms prevail in one plane. It defines monolayers bound together via the weaker Van der Waals force. By peeling away layers, atomically thin materials can be produced. Commonly called 2D materials, they easily generate strong quantum confinement effects in the stacking direction [5].

The most common technique used to prepare 2D materials is mechanical exfoliation, first used to produce graphite monolayers using regular adhesive tape. A more sophisticated material called polydimethylsiloxane (PDMS), a well known silicon-based organic polymer, is now more generally utilized. Its appeal comes from its viscoelasticity that depends on the speed of the pullout of the PDMS from a surface. For fast pullouts, the PDMS behaves like an elastic material, while it becomes viscous for slow ones. Playing with these characteristics enables either to transfer a raw flake from one surface to another (slow pullout) or to break interlayer bonds to produce thinner samples (fast pullout). This allows the fabrication of 2D materials as thin as a single monolayer and deterministic transfer to fabricate complex heterostructures involving several Van der Waals materials [4].

The process used to produce thin GaSe flakes is presented Fig. 4.1. First, a large flake is extracted from a GaSe crystal using a razor blade and is placed on a flat PDMS stamp. Approximately ten fast pullouts are then made on another flat PDMS stamp, as shown in Fig. 4.1 **a**), reducing the thickness of GaSe flakes to a few tens of microns. Then, using

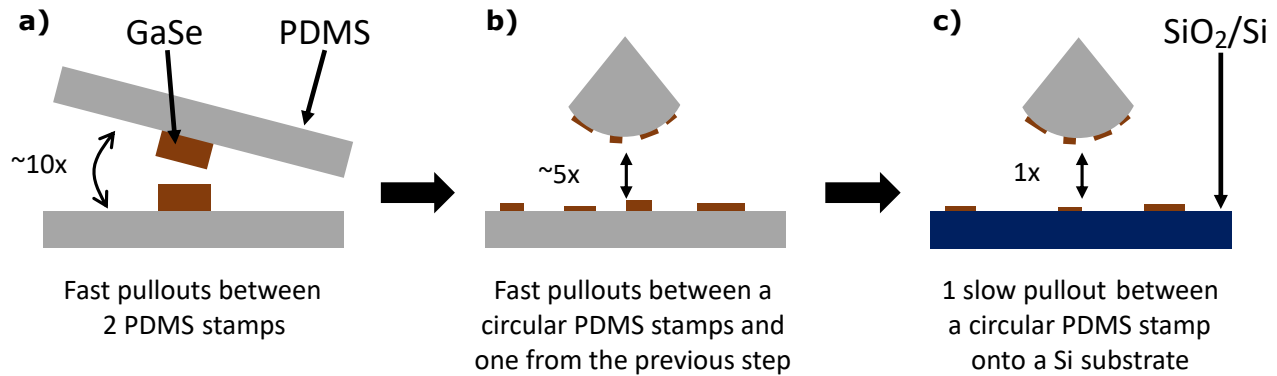


Figure 4.1 Exfoliation process followed to produce thin GaSe flakes. PDMS is shown in grey, SiO<sub>2</sub>/Si substrate in blue, and GaSe flakes in brown. The number next to double arrows is the amount of pullouts approximately done. A circular PDMS stamp allows more control over the transfer between the stamp and the substrate, for which a slow pullout is needed. **a)** a thick GaSe sample is cleaved from a mono-crystal and deposited onto a PDMS stamp. 10 fast pullouts are then made between 2 PDMS stamps to reduce the sample thickness. **b)** A circular PDMS stamp is used to do 5 more fast pullouts. **c)** the remaining flakes from the circular PDMS stamp are transferred onto the substrate with a slow pullout.

one of these two previous stamps, five more fast pullouts using a circular PDMS are done to get GaSe samples with a thickness ranging from approximately 50 nm to 1  $\mu$ m. Finally, the circular stamp, facilitating the transfer to another surface, is used to move the remaining flakes onto a SiO<sub>2</sub>/Si substrate by doing one final slow pullout.

To study the samples thickness dependence of PhP frequencies, samples between 30 nm and 1  $\mu$ m were produced. Many samples under 100 nm were studied to explore strong confinement behaviors and to find the limit at which PhPs can be probed. For studies not related to vertical confinement, thicker samples (>300 nm) were produced.

A disadvantage of using PDMS is that it leaves residues on both the GaSe sample and the substrate. These residues come from the PDMS itself and dust particles sticking to it. Hence, exfoliation must be done with care and is preferable to minimize the number of pullouts on the substrate.

The presence of contamination can easily be observed by the AFM. Images of contaminated and clean regions are shown Fig. 4.2. As can be seen, the image from a contaminated sample is blurred, making the determination of its dimensions uncertain. A clean and uncontaminated sample is a requirement for all experiments presented in this thesis, as shown in Fig. 4.2 **b)**.

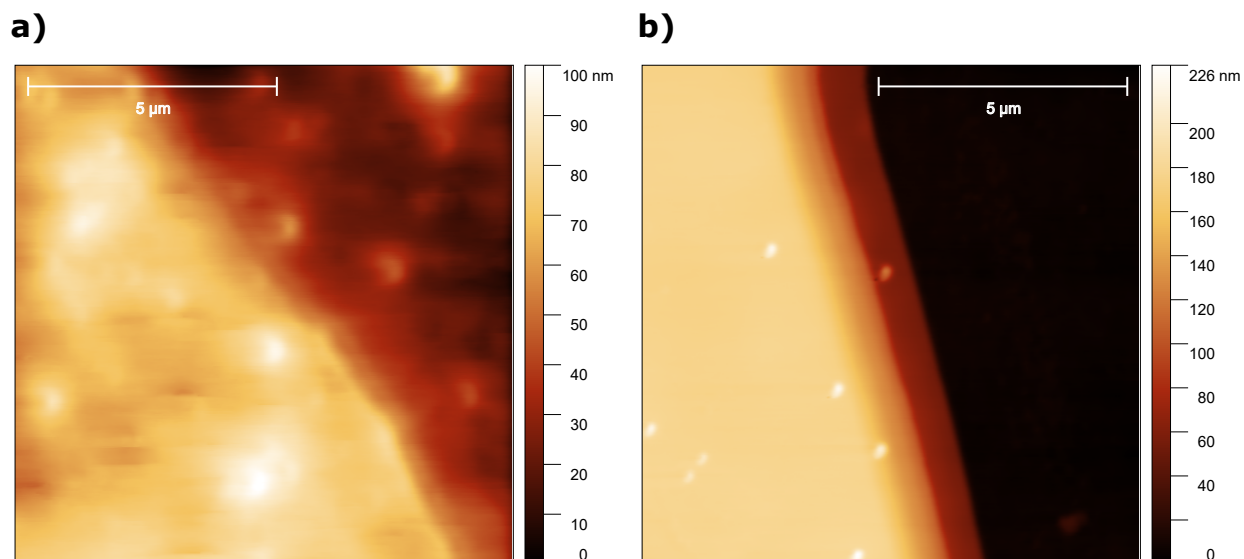


Figure 4.2 Impact of the presence of contamination on AFM images. **a)** The PDMS contaminated the sample and the substrate with residues and dust particles. The uncertainty on the sample thickness is 6%. **b)** The sample and the substrate are clean. The thickness uncertainty is 1%.

#### 4.1.2 Protecting sample from oxidation

Like many other 2D materials, GaSe is subject to oxidation. Oxidized samples prohibit the observation of PhPs since oxidation products have been shown to generate Raman signals in spectral regions of interest. For samples used in this work, degradation becomes significant on a time scale of about an hour in ambient air and temperature. However, when illuminated with a laser source, this time scale reduces to minutes and becomes an important issue for the Raman study of PhPs [76].

To prevent oxidation reactions, dioxygen and water vapor must be removed from the environment of GaSe [77]. Samples are placed into a cryostat and pumped to a pressure of  $10^{-6}$  mBar to remove ambient air. Other possible techniques to protect the samples are adding an inert gas instead of vacuum so no reaction can happen or using hBN layers to cover the GaSe flakes. [78]

The latter is not convenient since it requires the identification of interesting GaSe samples prior to deterministic transferring of h-BN flakes. It moreover requires several extra manipulations, reducing sample yield. However, when fabricating devices like GaSe nanoribbons, h-BN encapsulation could be an interesting approach.

### 4.1.3 Dimensional characterization

An optical microscope was used to locate potentially interesting flakes and estimate their lateral dimensions. Their thickness was measured using an AFM in tapping mode. To avoid oxidation, they were measured right after performing all Raman measurement in vacuum, or store in vacuum awaiting AFM availability.

AFM images were post-processed to extract the thickness along line profiles perpendicular to samples edge. In order to assess the validity of the thickness measurement, many line profiles were extracted at different locations to confirm the repeatability. Then, one line profile was selected. The average heights of the substrate and the sample as well as the standard deviation (RMS) were gathered. Finally, the extracted sample thickness is  $h = \mu_{sample} - \mu_{subs}$  with an uncertainty given by  $\sigma = \pm\sqrt{\sigma_{sample}^2 + \sigma_{subs}^2}$ , where  $\mu$  denotes the averaged height and  $\sigma$  the standard deviation.

Fig. 4.3 shows an example of an extracted line profile of a  $201 \pm 2$  nm thick GaSe sample. The chosen region of the sample is flat and with few irregularities. As a result, the extracted line profile displays smooth plateaus on both the substrate and the sample.

Despite the AFM resolution of approximately 1 nm, the sample quality and contaminations from the PDMS can lower the resolution. The experimental uncertainty on the measured thickness is below 5% of the measured thickness for most samples studied in this thesis. For some samples however, it could be as high as 14%. In this work, uncertainties are reported along with sample thicknesses.

## 4.2 Phonon-polariton measurement

This section discusses central experimental aspects of the studies of PhPs. The Raman optical setup is first presented along with the characteristics of the main optical components. A knife-edge test is then performed to measure the dimension of the laser beam at the sample location. The numerical aperture (NA) of the sample excitation setup branch is also extracted.

A typical Raman spectrum from a GaSe thin sample is presented and analyzed to attribute all Raman lines. Non-linear fits are performed to obtain the frequency, full width at half maximum (FWHM), and intensity of all modes observed. Finally, spectral broadening phenomena caused by the combination of the instrumentation finite NA and the dispersion of PhPs is discussed.

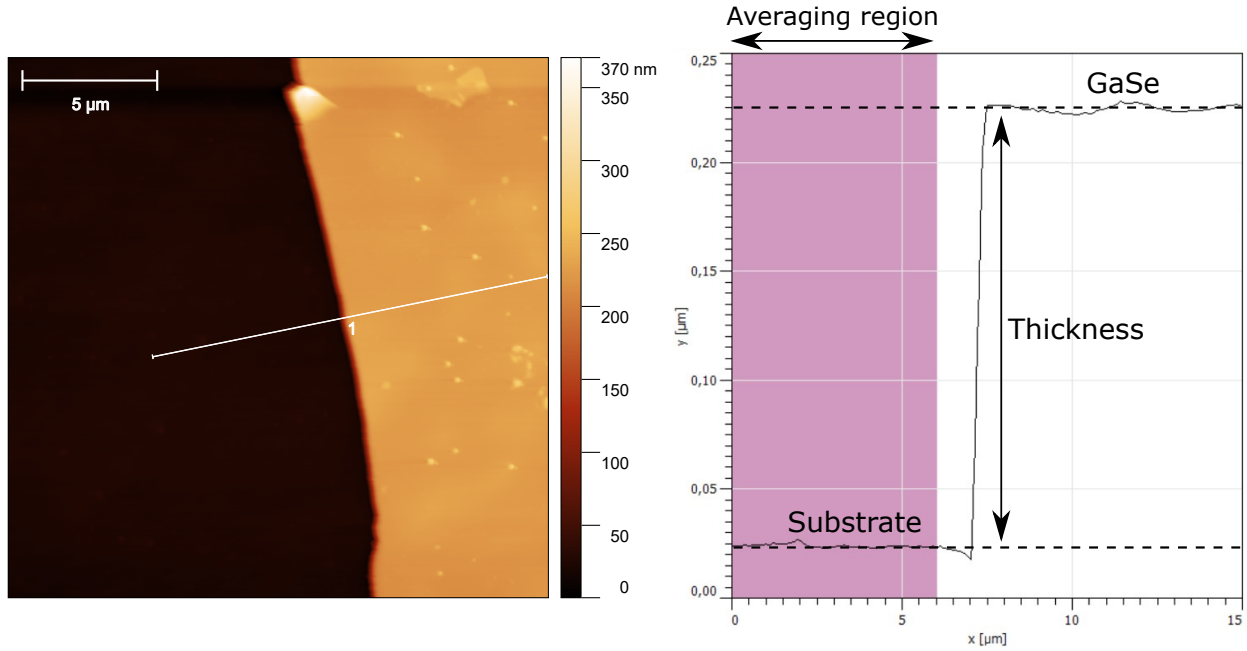


Figure 4.3 Left : AFM image of a  $201 \pm 2$  nm thick GaSe flake. Right : extracted line profile. Dashed lines are substrate and flake heights.

#### 4.2.1 Optical setup

A diagram of the backscattering Raman setup built during this project is shown in Fig. 4.4. The different signals traveling across the setup are depicted by green, blue, and red lines for the path of the excitation laser, the sample image, and the Raman signal respectively.

The excitation laser is a Nd-YAG single mode laser emitting at 532 nm with a 1 MHz FWHM linewidth. To remove laser sidebands, a band-pass filter with an optical density of 3.5 at  $\pm 1$  nm and up to 6 at  $\pm 5$  nm is used. An anti-reflection coated ( $R < 0.5\%$ ) non-polarizing beamsplitter with a transmission of 90% and a reflection of 10% redirects the excitation laser toward the sample.

The excitation laser is focused to the sample by a microscope objective with a numerical aperture of 0.55 and a transmission of 80%. The 1.9 mm laser beam diameter (see next section for laser beam characterization) does not entirely fill the 5 mm entrance pupil of the objective, and leads to an effective NA of only 0.21.

The sample is enclosed inside a cryostat and is placed under vacuum. Filled with liquid nitrogen, the cryostat allows measurements at 77 K. The cryostat is fixed to a rotating stage that allows a sample tilt of  $\pm 40^\circ$  for samples in air. This angle reduces to  $\pm 25^\circ$  when the sealing glass of the cryostat is mounted.

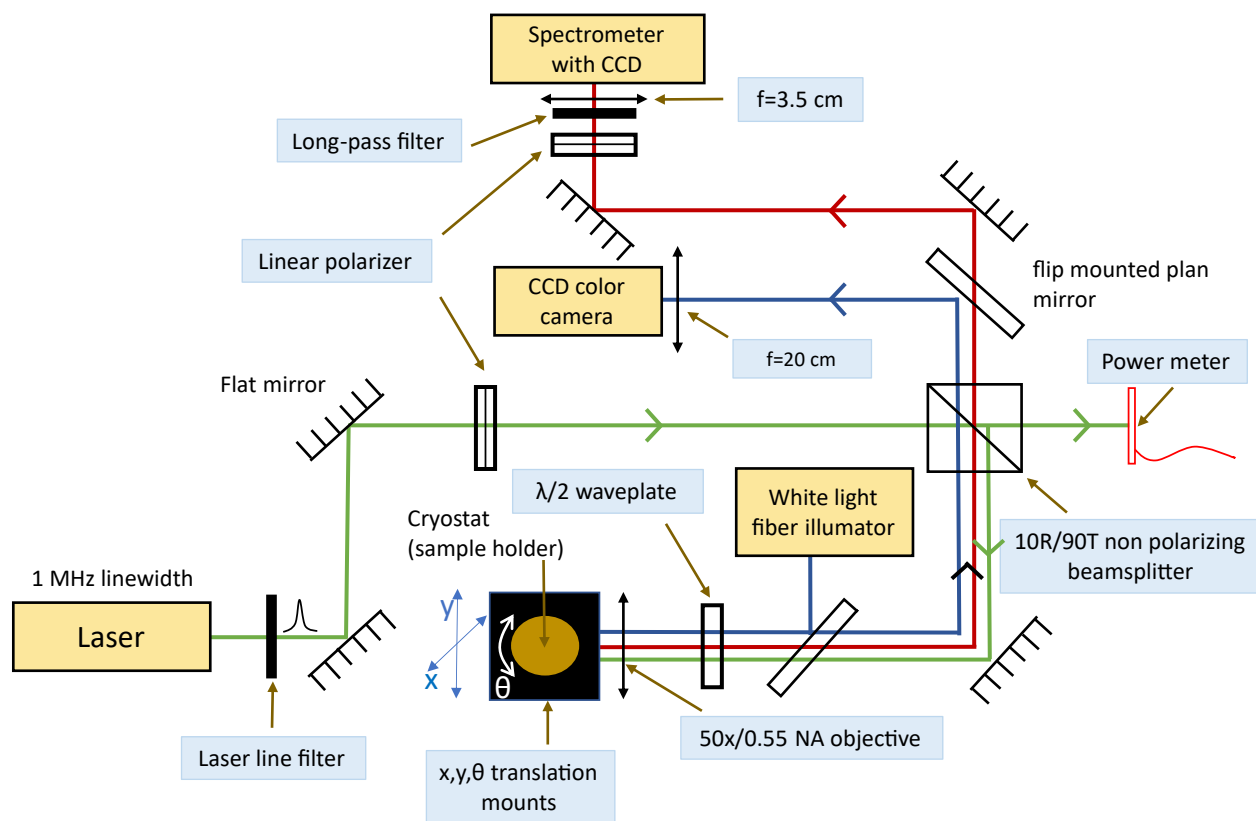


Figure 4.4 Raman backscattering experimental setup built. Green, blue and red lines indicates the path of the excitation laser, the sample image, and the Raman signal, respectively.

The scattered Raman and Rayleigh signals are collected by the objective and transmitted through the non-polarizing beamsplitter. Laser reflections and Rayleigh signals are filtered by a long-pass edge filter at 532 nm, with a transition width of  $120\text{ cm}^{-1}$ , an edge steepness of  $\sim 35\text{ cm}^{-1}$ , and transmission of 93% for wavelengths above 535 nm.

The Raman signal is focused onto the entrance slit of the spectrometer by a 3.5 cm focal length achromatic doublet with a transmission of 98%. This focal length was chosen to optimize the amount of light reaching the grating for a beam diameter of 5 mm, the diameter of the objective pupil. The spectrometer is composed of 2 aspherical mirrors with a focal length of 50 cm. It is equipped with a 1200 g/mm grating with maximum efficiency around 530 nm.

The spectra were measured using a charge coupled device (CCD) camera. Two cameras were used along this work. The data gathered for the first study (see thickness dependent PhPs energy section 5.1.2) used a EMCCD camera working at  $-80^\circ$  with a quantum efficiency of 35% around 550 nm. The sensor is composed of 1600x400 pixels, each with a size of 16 by 16  $\mu\text{m}$ . The resulting spectral resolution is  $0.85\text{ cm}^{-1}$ . The second is a cryogenically-cooled

CCD camera operating at  $-120^{\circ}\text{C}$ . It provides a quantum efficiency of 90% around 550 nm. The sensor is composed of 1340x400 pixels, each with a size of 20 by 20  $\mu\text{m}$ . This larger pixel size leads to a lower spectral resolution of  $1.1\text{ cm}^{-1}$ , but the significantly higher quantum efficiency provides much better sensitivity.

White light from a fiber-coupled illuminator is injected into the optical path using a semi-transparent mirror to image the sample and the laser excitation spot simultaneously. This mirror is installed on a flip mount between the sample and the beamsplitter. Then, the image of the sample is projected onto a color CCD camera using a 20 cm focal length achromatic lens.

Finally, polarization-resolved Raman measurements were conducted to investigate the intensity and frequency anisotropy of PhPs from rectangular GaSe samples. Although the laser is nominally vertically polarized with a 1:100 ratio, a linear polarizer with a 1:1000 polarization ratio is used at the laser output to increase the polarization contrast. A half-waveplate mounted on a rotative motorized stage is added between the beamsplitter and the sample to rotate the excitation laser polarization. It has a retardation of 0.53, a transmission of 97.5% at 530 nm and an anti-reflection coating ( $R < 0.5\%$ ). Upon rotating the waveplate from 0 to  $90^{\circ}$ , a frequency deviation of  $0.05\text{ cm}^{-1}$  is observed on the spectra, which is attributed to the birefringence uncertainty onto the frequency variation. Finally, another linear polarizer with a maximum transmission of 60% at 532 nm and an extinction ratio of 1:1000 is placed between the beamsplitter and the spectrometer. It has the role of an analyzer and enables to switch between parallel and crossed polarization configurations.

#### 4.2.2 Excitation beam dimension

To characterize the dimension of the laser spot exciting the samples, a knife-edge test was performed using a sharply cleaved Si substrate as a reflective media. This substrate was glued to a non-reflective material.

The transverse profile of the laser spot can be approximated by a 1D-Gaussian profile

$$f(x) = \frac{1}{\sigma\sqrt{2}} e^{-\frac{(x-x_0)^2}{2\sigma^2}}, \quad (4.1)$$

where  $\sigma$  is proportional to the spot width  $d_0 = 4\sigma$ , and  $x_0$  is the center position of the spot. The width is defined at an intensity of  $1/e^2$ .

By scanning this beam across the Si edge, it travels from the reflective to the non reflective medium. The reflected signal corresponds to the portion of the Gaussian profile over the

reflective part. The intensity of this signal, considering a distance  $d$  between  $x_0$  and the Si edge position, is the definite integral of the Gaussian profile

$$F(d) = \frac{1}{2} \left( 1 + \operatorname{erf} \left( \frac{d - x_0}{\sigma \sqrt{2}} \right) \right), \quad (4.2)$$

where  $\operatorname{erf}(x)$  is the error function. The edge is arbitrary set to  $x_0 = 0 \mu\text{m}$ .

The measured reflected laser intensity with respect to the edge position, with a translation step size of 80 nm, is shown in Fig. 4.5. The inset shows a photography of the sample with the white arrow depicting the translation direction of the Si substrate.

To calculate the beam width, the coefficient  $\sigma$  was extracted by fitting Eq. 4.2 to the data (blue points). The fit is depicted by the red line on the figure. The extracted beam width is  $d_0 = 1.7 \mu\text{m}$  with less than 1% uncertainty.

In the paraxial approximation for Gaussian beam propagation, the beam radius is linked to its divergence with  $\theta_{NA} = 2\lambda/\pi d_0$ . In this case, it corresponds to the maximum angle with which the objective focus the excitation source. It is linked to the NA of the objective with  $NA = n \sin(\theta_{NA})$ . Hence,  $\theta_{NA} \sim 12^\circ$ , and the effective NA of the objective for focusing the excitation laser is 0.21.

The theoretical NA of the objective is 0.55, achieved if the 5 mm entrance pupil is fully illuminated. As the ratio between the effective and the theoretical NA is  $\sim 38\%$ , we can conclude that only  $5 \times 38\% = 1.9 \text{ mm}$  of the entrance pupil is illuminated. It corresponds to the diameter of the collimated excitation laser.

### 4.2.3 Calibration

The CCD camera returns the intensity integrated over time and pixel area, for each of its pixel. The raw data returned by the CCD is the intensity as a function of pixel position. In order to convert these data into a spectrum, a calibration table must be established between pixel positions and wavelengths.

Krypton and Neon calibration lamps with precisely known emission lines are used to get 9 points of calibration spanning the whole sensor. To take into account the non-linear relationship between wavelengths and diffraction angles of the grating, a quadratic regression is performed. Finally, to convert wavelengths into relative wavenumbers (in  $\text{cm}^{-1}$ ), the transformation  $10^7 \cdot [1/\lambda_{laser}(\text{nm}) - 1/\lambda(\text{nm})]$  is applied, where  $\lambda_{laser}$  is the wavelength of the excitation laser.

The non-linear regression provides a quadratic coefficient of approximately  $10^{-6} \text{ nm}$ . It leads

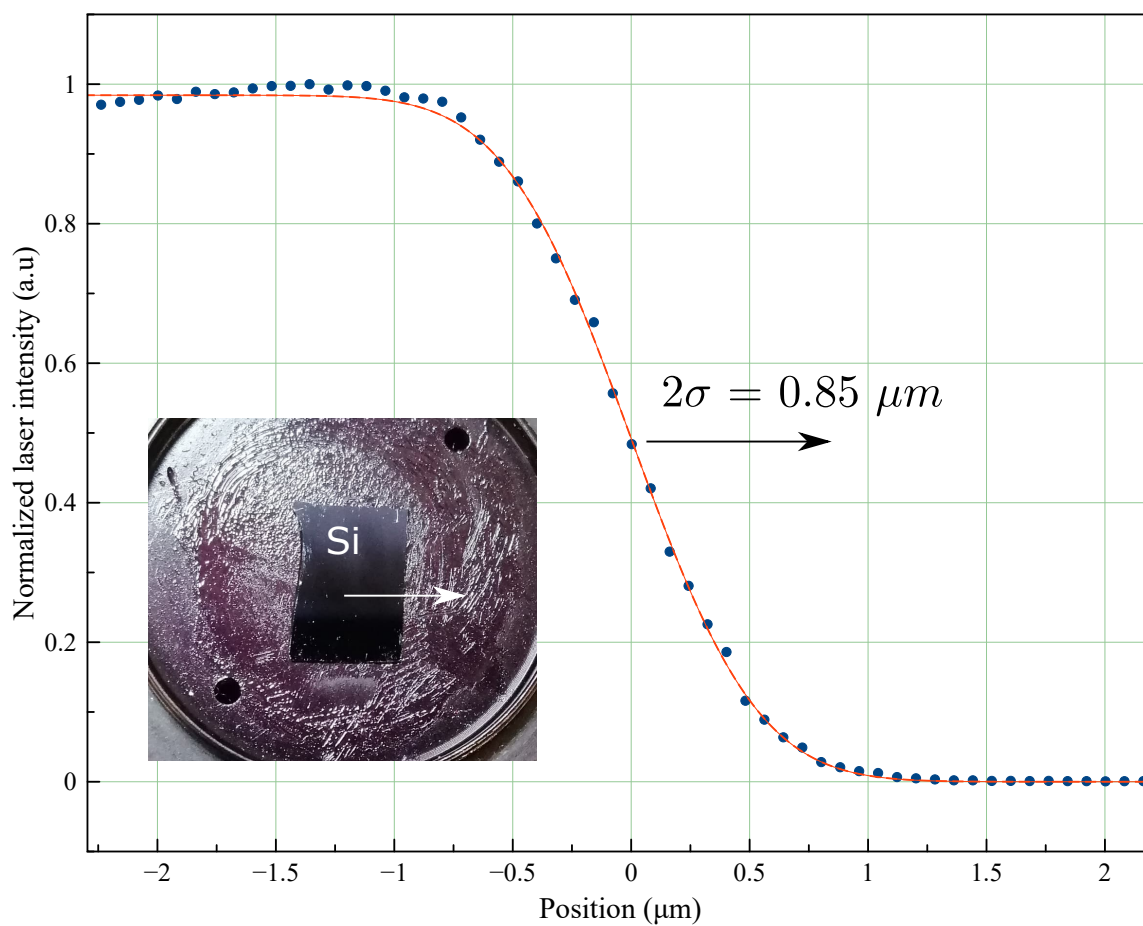


Figure 4.5 Measurement of the beam width focused by an under illuminated 0.55 NA objective. The red line is a fit of Eq. 4.2 to the data, represented by blue circles. The extracted  $\sigma$  parameter leads to a beam width of  $4\sigma = 1.7 \mu\text{m}$ , at an intensity of  $1/e^2$ . The center position of the edge  $x_0$  was arbitrary set to  $0 \mu\text{m}$ .

to a correction of about  $-4\text{ cm}^{-1}$  for the last pixel of the sensor, compared to the simpler but less accurate linear regression. A non-linear regression is therefore required.

When performing angular dispersion measurement, an oblique incidence can lead to a small lateral shift, which is translated by the spectrometer into a wavenumber shift in the spectra. To compensate, a correction must be added to the calibration table, as described next.

First, as the excitation laser position can slightly shift by  $\sim 0.5\text{ cm}^{-1}$  over days, the spectra at  $0^\circ$  incidence were recalibrated so the wavenumber of the excitation laser line is at  $0\text{ cm}^{-1}$ . Then, fully symmetric  $A'_{11}$  and  $A^3_{11}$  phonon frequencies from GaSe are used as a reference, since they are isotropic and do not exhibit any angular dispersion. The spectra for oblique incidences were then recalibrated using a linear regression so the frequency of these phonons matches the frequency found at normal incidence.

#### 4.2.4 Data processing

This section focuses on the processing of experimental Raman spectra to extract useful spectral information about PhPs from GaSe. As an example, Fig. 4.6 displays a processed Raman spectra for a sample of thickness  $380 \pm 2\text{ nm}$  at  $300\text{ K}$  and a sample tilt angle of  $10^\circ$ . The solid red curve corresponds to the sum of all fitted functions used to model experimental data, which are depicted by blue circles. Individual functions corresponding to phonons and PhPs are depicted by solid colored lines. The discussion below describes the steps followed for data processing and how spectral information were extracted.

#### Pre-processing

In GaSe, the spectral region of interest is between  $120$  and  $350\text{ cm}^{-1}$ . In this region, a parabolic baseline is subtracted to remove a broad background composed of an intense GaSe photoluminescence at  $2700\text{ cm}^{-1}$  (in relative units), second order Si Raman modes and residual stray light.

#### Phonon lines

As shown in Sec. 3.3.1, only vibrational modes of symmetry  $A'_{11}$ ,  $E'$  and  $E''$  are allowed in Raman scattering from GaSe. Acoustic modes apart, it leads to potentially 18 visible spectral lines in experiments. However, Davydov doublets and degenerate  $E'$  and  $E''$  mode reduce the number of potentially observable Raman lines to 6.

One  $E'$  and one  $E''$  modes have a very low frequency that cannot be measured with the

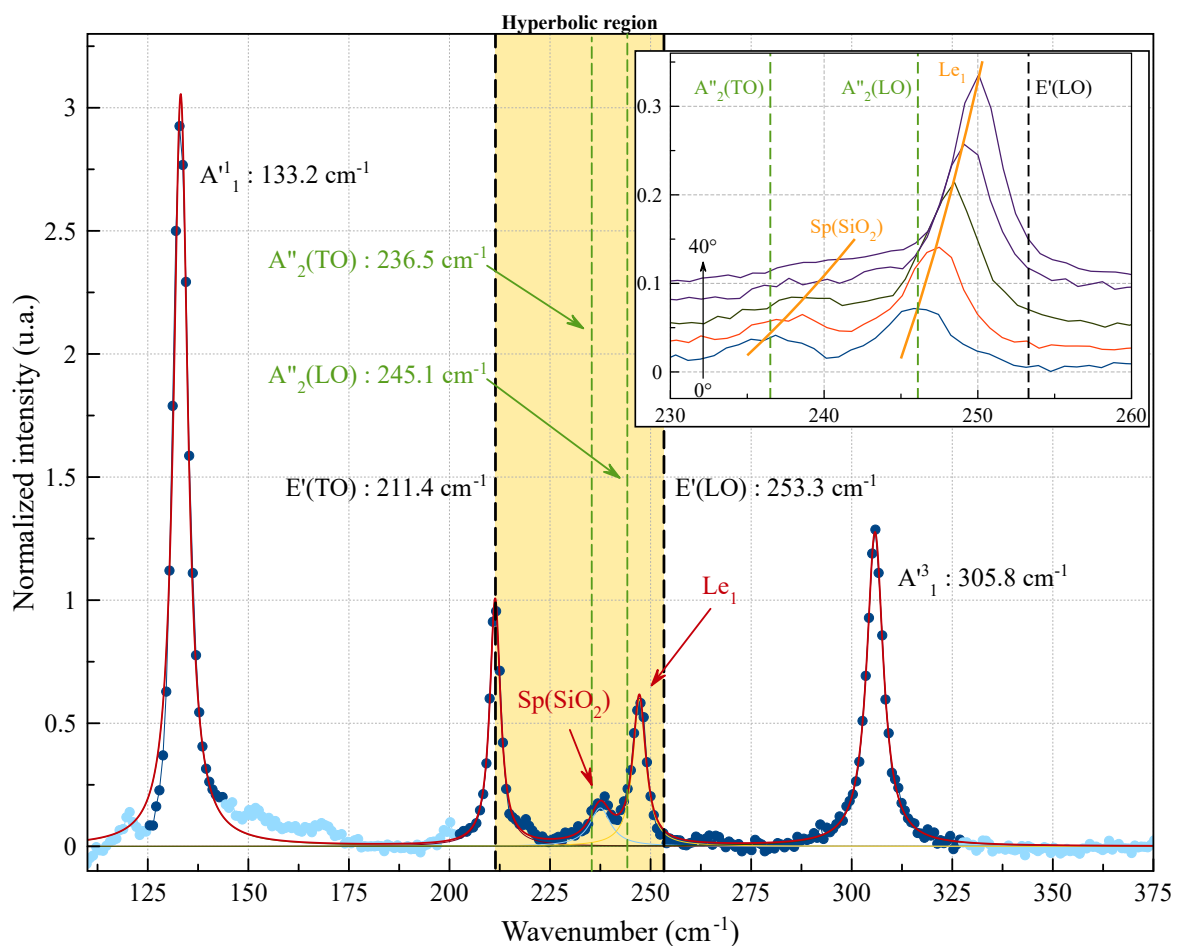


Figure 4.6 Raman spectra from a GaSe flake of thickness  $380 \pm 2 \text{ nm}$  at  $300 \text{ K}$ , with a sample tilt angle of  $10^\circ$ . The spectra is composed of 3 phonons ( $A^1_1$ ,  $E'(\text{TO})$  and  $A^3_1$ ) and 2 PhPs ( $Le_1$  and  $Sp(\text{SiO}_2)$ ). Blue circles display experimental data. Deep blue circles are data considered for the regression. The dashed red line is the sum of all single fitted functions, depicted by the different colored curves. Finally, vertical dashed lines indicate the tabulated position of GaSe pure phonons.

available Raman system. Moreover, the remaining  $E'$  is not allowed in the backward configuration. Because the remaining  $E'$  is polar, the LO-TO degeneracy is split at the Brillouin zone center. However, the  $E'$ (LO) mode is not allowed in the backscattering configuration. As a result, 3 Raman lines from phonons are expected in GaSe Raman spectra. They are labeled as  $A^1_1$ ,  $E'$ (TO) and  $A^3_1$ .

These Raman lines are reported in the spectrum presented in Fig. 4.6. They are located at a frequency of 133.2 for the  $A^1_1$ , 211.4 for the  $E'$ (TO) and 305.8  $\text{cm}^{-1}$  for the  $A^3_1$ . These correspond to tabulated frequencies with a deviation of at most 1% (see Table S1). The phonon spectral intensity profiles are best modeled by a Lorentzian lineshape. As can be seen in Fig. 4.6, this lineshape successfully captures the spectral information of experimental data, especially the ones from the  $E'$ (TO) and the  $A^3_1$ . Typically, the uncertainty on the extracted peaks position is approximately 0.05  $\text{cm}^{-1}$ .

A slight discrepancy between data and the fitted function appears at the base of the  $A^1_1$ . In this region, the measured intensity is affected by the long-pass filter. Also, weak Raman features around 120  $\text{cm}^{-1}$  and 150  $\text{cm}^{-1}$  are measured. They are attributed to GaSe oxidation products [76]. Despite protecting the flakes from ambient air during Raman measurements, the exfoliation is not performed in a controlled atmosphere, allowing some oxidation to occur even on a short time scale. Although the Lorentzian profile does not correctly model the base of the  $A^1_1$  profile, its very high intensity allows for the analysis of its position, width and amplitude with a similar accuracy as the other phonons.

### Phonon-polariton lines

Inside the hyperbolic region of GaSe delimited by the  $E'$ (TO) and  $E'$ (LO) polar phonons, two spectral features attributed to  $Le_1$  (longitudinal extraordinary) and  $Sp(\text{SiO}_2)$  (surface) PhPs modes are identified. The inset of Fig. 4.6 shows Raman spectra for sample tilt angles ranging from  $0^\circ$  to  $40^\circ$ . The orange curve is a guide for the eye of peak position. Dispersive behaviors with an amplitude of 3.8  $\text{cm}^{-1}$  for the  $Le_1$  and 4.9  $\text{cm}^{-1}$  for the  $Sp(\text{SiO}_2)$  are observed over this angular range. As demonstrated in Ref. [24], any observed angular dispersion of more than 0.9  $\text{cm}^{-1}$  at a sample tilt of  $45^\circ$  cannot be attributed to angular dispersion of polar phonons.

The linewidth of the  $Le_1$  is well resolved by the instrumentation, so a Lorentzian lineshape is used to model this linewidth. For the sample studied in Fig. 4.6, it is measured at a frequency of  $246.12 \pm 0.08 \text{ cm}^{-1}$  at normal incidence, and  $249.95 \pm 0.02 \text{ cm}^{-1}$  for a sample tilt of  $40^\circ$ . As can be seen on the inset, the FWHM decreases with increasing sample tilt, going from 4.7 to 3.5  $\text{cm}^{-1}$ . Indeed, the slope of the dispersion curve decreases for higher

incidence angles, resulting in a lower angular broadening of PhPs. This effect will be further discussed in the next section. Finally, the intensity of this mode increases by a factor of 3.7 between normal and  $40^\circ$  incidence. This is explained by the Raman tensor of the Le mode, described by Eq. 3.48.

A weaker additional Le line was sometimes measured at a higher frequency. Its intensity was vanishing at oblique incidence angles. This line has been attributed to a PhP mode thanks to a resonant excitation near the 1s GaSe exciton [24]. It will not be further discussed in this work.

As already introduced in the modeling section of PhPs, two surface modes can propagate, one at each interface. They lie between  $E'(TO)$  and  $A''_2(LO)$  phonons. This region contains a type-II hyperbolic band between  $E'(TO)$  and  $A''_2(TO)$ , and a double Reststrahlen band between  $A''_2(TO)$  and  $A''_2(LO)$ . Here, only one surface mode is measured in the spectrum.

In Fig. 4.6, the mode at the GaSe/substrate interface appears at a frequency of  $236.0 \pm 0.2 \text{ cm}^{-1}$  at normal incidence and  $240.9 \pm 0.4 \text{ cm}^{-1}$  at  $40^\circ$ . Since the substrate is composed of Si with a thin  $\text{SiO}_2$  layer, this mode is labeled  $\text{Sp}(\text{SiO}_2)$ . It is more dispersive than the  $\text{Le}_1$ . As a consequence, angular broadening leads to broader spectral lines, and the FWHM can be as large as  $14 \text{ cm}^{-1}$  for some samples. Due to this angular broadening, the lineshape is not expected to remain Lorentzian. However, for most spectra, a Lorentzian lineshape captures successfully the lineshape of the  $\text{Sp}(\text{SiO}_2)$ . For a few samples, a Gaussian lineshape proved to be more appropriate.

Contrary to the  $\text{Le}_1$ , the intensity of the  $\text{Sp}(\text{SiO}_2)$  decreases with increasing sample tilt, as can be seen on the inset of the figure. It loses approximately half of its intensity when comparing normal and  $40^\circ$  incidence. The  $\text{Sp}(\text{SiO}_2)$  is described by a combination of Te and Le Raman tensors. As Te tensor components decrease with sample tilt (see Eq. 3.48), we can suppose this surface mode to have a dominant Te component. Finally, a quick drop of signal can also be observed when the mode is close to the  $A''_2(LO)$  frequency, forbidden in Raman. Despite reducing the quality of the lineshape modeling, the uncertainty on the  $\text{Sp}(\text{SiO}_2)$  frequency always remains below  $1 \text{ cm}^{-1}$ .

#### 4.2.5 Angular Broadening

As presented in the previous section, the frequency region between  $A''_2(LO)$  and  $E'(LO)$  phonons contains many guided Le modes. Their frequency decreases with increasing mode order. In this work, only the fundamental mode  $\text{Le}_1$  is observed experimentally. As the Le modes are separated by few wavenumbers, the instrumental resolution of  $\sim 1 \text{ cm}^{-1}$  and the

FWHM of the  $\text{Sp}(\text{SiO}_2)$  ( $\sim 10 \text{ cm}^{-1}$ ) and the  $\text{Le}_1$  ( $\sim 4 \text{ cm}^{-1}$ ) prevents their observation.

The PhP linewidth can be interpreted by virtue of the non zero angular acceptance of the instrumentation, that broaden PhP spectral lines. This angular broadening is attributed to the finite NA of the microscope objective combined with the wide Raman excitation and Raman collection beams at the sample location.

The angular broadening is quantified by the maximum angle made by the rays of these beams with the optical axis, in the objective focal plane. This angle, defined as  $\theta_{NA}$ , is linked to the  $\text{NA} = n \sin(\theta_{NA})$  of the objective. At first approximation, this angle is the same for both the sample excitation and the signal collection. The calculated effective NA of 0.21 from Sec. 4.2.1 leads to an estimation of  $\theta_{NA,excit} = \theta_{NA,col} = 7^\circ$  for these two contributions.

### Angular broadening from Raman signal collection

As PhPs can scatter photons in all directions, the objective collects all the Raman scattered signal within the NA of the objective. The collected Raman signal is attributed to PhPs with propagation angles in the range  $\theta \pm \theta_{NA,col}$ , with  $\theta$  the sample tilt angle and  $\theta_{NA,col}$  the collection angle. As one propagation angle is related to one frequency in the PhP dispersion relation, probing many propagation angles at once leads to the measurement of PhPs with different frequencies. Hence, a large collection angle induces broadening of PhP spectral lines.

This broadening is accounted for in the computed PhP dispersion using the model described in Sec. 3.4.2. The calculated broaden Raman spectra matching the experimental data is computed by summing simulated unbroaden Raman spectra for all collected angles, weighted according to a Gaussian distribution centered at the tilt angle  $\theta$  (fixed) and having a standard deviation of  $\sigma = \theta_{NA,col} / \sqrt{2 \ln(2)}$ . The angle best modeling experimental data is  $\theta_{NA,col} = 5^\circ$  [24].

Fig. 4.7 shows an example of superimposed experimental and computed PhP Raman scattering dispersion from a 650 nm thick sample. Experimental PhP spectral line positions are depicted by white circles. The background is the computed PhP dispersion without angular broadening effects, with bright color corresponding to the Raman intensity. Grey dashed horizontal lines indicate pure phonon frequencies. The green dashed horizontal line located at a frequency of  $241.6 \text{ cm}^{-1}$  is the permittivity confinement criterion for the  $\text{Sp}(\text{SiO}_2)$  [24]. This will be further discussed in the next chapter.

The green region depicts the tilt angle range probed at normal incidence due to angular broadening. Since the dispersion is strong in this region, a large amount of frequencies

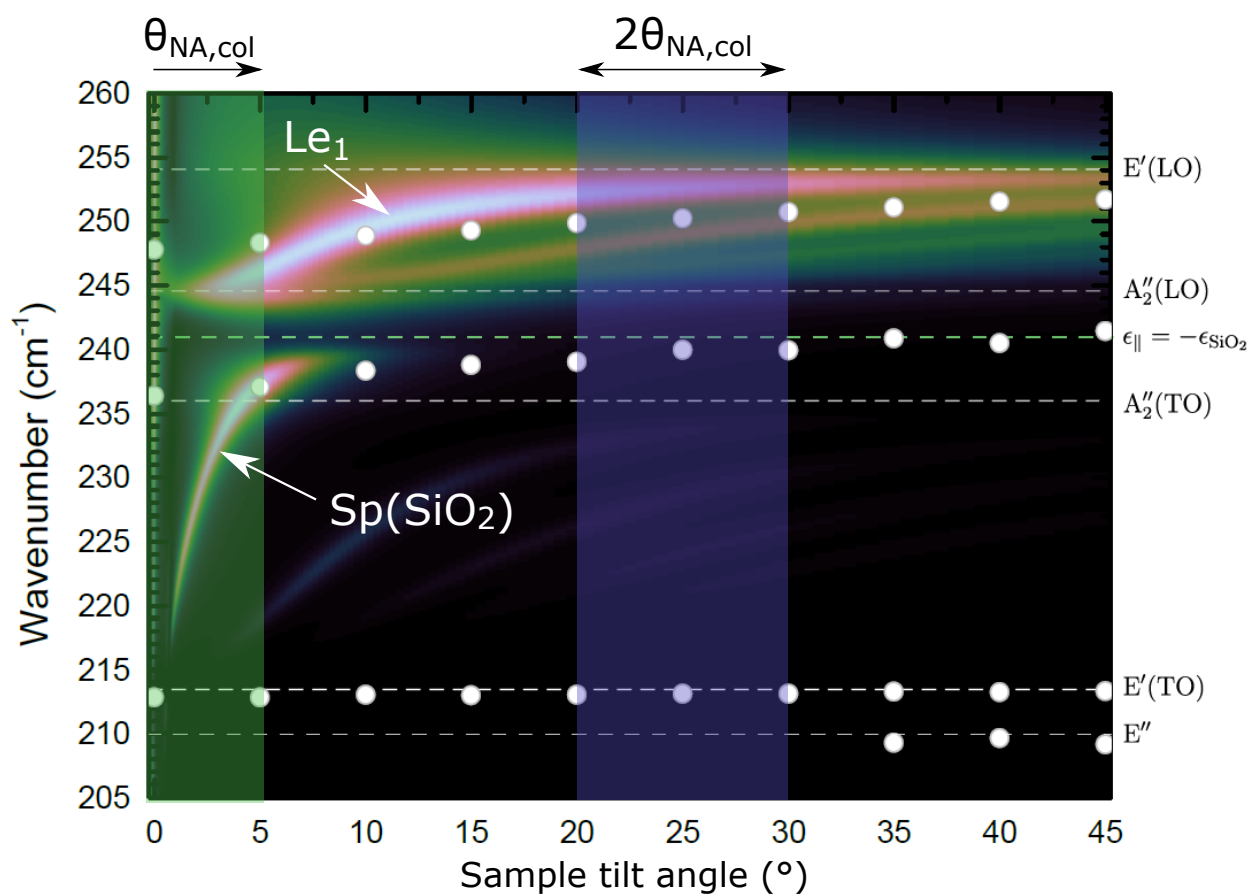


Figure 4.7 Calculated Raman spectra of PhP dispersion for a 650 nm sample, without angular broadening. The computed background corresponds to the Raman intensity depending on the sample tilt angle on a logarithmic scale of  $S=10$ . White circles are data points of experimental PhP Raman line positions. The attributed uncertainty is lower than the point size. The green region corresponds to the probed PhP propagation angles due to angular broadening at  $0^\circ$  incidence, while the blue region is the probed region for sample tilt of  $25^\circ$ . Adapted with permission from Ref. [24] © 2020 Alaric Bergeron.

contribute to the collected Raman spectrum. It leads to a large broadening of PhP lines and frequencies higher than what is expected from the tilt angle alone. The blue region shows the probed angle range for a sample tilt of  $25^\circ$ , where the dispersion is much weaker. In this second case, the measurement more faithfully reports the PhP frequency and the effect of angular broadening is minimized.

### **Angular broadening from Raman excitation**

Angular broadening originating from the Raman excitation also limits the spectral resolution. At a sample tilt  $\theta$ , each incident ray between  $\theta - 7^\circ$  and  $\theta + 7^\circ$  also contributes to the scattering of PhPs in any direction. These scattered PhPs subsequently induce angular broadening from Raman signal collection. As a result, every incident ray contributes to the broadening of the PhP Raman lines. This contribution is however harder to account for in the simulations. Combined with angular broadening from the signal collection, the required computational time is too important as it is around 10 h for one incidence angle.

Angular broadening is therefore a key experimental aspect of PhP Raman measurements. Due to the finite NA of the microscope objective at the sample location, both the excitation and the collection Raman beams induce angular broadening of the PhP Raman lines. This broadening originates from the dispersion of PhPs, and is more important at low sample tilts. This therefore lowers the resolution of PhP Raman lines, alters their measured frequency, and limits the ability to resolve all PhP modes. The angular dispersion can be minimized using low NA objectives and k-imaging techniques.

## CHAPTER 5 RESULTS

The propagation properties of PhPs are encoded in the dispersion relation, which links the frequency  $\omega$  of a PhP to its wavevector  $\mathbf{q}$ . In hyperbolic materials the dispersion is hyperbolic and PhPs with high momentum can propagate. As demonstrated in Sec. 3.3, these PhPs are experimentally accessible using Raman scattering in the backward configuration. In this configuration, PhPs with in-plane wavevectors in the range of 0 to  $2 \times 10^5 \text{ cm}^{-1}$  can be probed. Therefore, the dispersion of PhPs from thin GaSe crystal can be measured experimentally.

The crystal dimension highly influences the dispersion of PhPs. The first result of this work presents the dependence of the PhP dispersion on the thickness of the GaSe sample. Then, the frequency of the  $\text{Le}_1$  and the  $\text{Sp}(\text{SiO}_2)$  PhP modes are compared with calculated Raman spectra as a function of the GaSe thickness.

Finally, polarization-resolved Raman measurements are performed to probe lateral confinement of PhPs in rectangular GaSe samples. As the polarization angle is varied, the measured frequency of the PhP shifts. It is observed that the maximum frequency shift occurs along the short and long sample axes.

### 5.1 Raman measurement of phonon-polaritons dispersion

In thin GaSe crystals, PhP modes are vertically confined which influences their dispersion. In this section, the influence of the GaSe crystal thickness on the PhP dispersion is studied. First, experimental data of PhP angular dispersion as a function of the crystal thickness are presented. Then, the measured  $\text{Le}_1$  and  $\text{Sp}(\text{SiO}_2)$  mode frequencies are compared with calculated PhP Raman spectra.

#### 5.1.1 Thickness dependent phonon-polaritons dispersion

Vertically confined PhPs have higher wavevectors than PhPs propagating in bulk crystals, so much so that their dispersion can be probed using Raman scattering in the backward geometry. This technique was used in order to investigate changes in the PhP dispersion from GaSe crystal of different thicknesses.

The angular dispersion of PhPs measured by Raman backscattering is presented in Fig. 5.1, considering GaSe samples of thickness ranging from 201 nm to  $12 \mu\text{m}$ . They have lateral dimensions between  $10 \mu\text{m}$  and more than  $100 \mu\text{m}$  to lower the risk of unwanted lateral confinement effects, even though it is negligible compared to vertical confinement effects.

Due to geometrical constraints, the maximum sample tilt angle usually ranges between  $25^\circ$  and  $45^\circ$ . The sample tilt angles, shown on the top axis, are converted to in-plane wavevectors  $q_{\parallel}$  by using Eq. 3.54. Displayed on the bottom axis, this scale is more convenient to discuss the dispersion of PhPs. The modes measured at normal incidence ( $\theta = 0^\circ$ ) are consequently associated to a zero in-plane wavevector, at which no PhP mode should be measured. Angular broadening from Raman signal collection includes PhPs measured at  $\pm 5^\circ$  around the sample tilt angle. At normal incidence, PhPs with an in-plane wavevectors of up to  $2 \times 10^4 \text{ cm}^{-1}$  are therefore probed. This value constitutes the in-plane wavevector resolution of the instrumentation at normal incidence.

In total, three PhP branches are observed. They are displayed in blue, green and yellow for the  $\text{Sp}(\text{SiO}_2)$ ,  $\text{Sp}(\text{air})$  and  $\text{Le}_1$  mode, respectively. In the reported dispersion curves, the color gradient gives a visual reference of the GaSe crystal thickness, where darker colors indicates thicker samples. Finally, the  $\text{A}''_2(\text{TO})$ ,  $\text{A}''_2(\text{LO})$  and  $\text{E}'(\text{LO})$  polar phonon frequencies are indicated on the right axis.

### Thickness-dependent dispersion of the $\text{Le}_1$ mode

As introduced in the previous chapters, the  $\text{Le}_1$  PhP mode is located in a type-II hyperbolic region of GaSe, between the  $\text{A}''_2(\text{LO})$  and  $\text{E}'(\text{LO})$  polar phonon frequencies. These respectively defines the lower and the upper frequency limits of the mode. At lower wavevectors, the  $\text{Le}_1$  extrapolates to the dispersion of light in air, down to the  $\text{A}''_2(\text{LO})$  frequency. At higher wavevectors, this mode extrapolates to the frequency of the  $\text{E}'(\text{LO})$  phonon. As can be seen in Fig. 5.1, the expected  $\text{Le}_1$  mode dispersion is measured.

An increase in the measured dispersion slope with decreasing sample thickness is observed. This can be explained by the vertical confinement of PhPs, which flattens their dispersion curves and reduces the effects of angular broadening. The in-plane wavevector of extraordinary PhPs can be written using Eq. 3.31 as

$$q_{\parallel} = \sqrt{\epsilon_{\parallel} \frac{\omega^2}{c^2} - \frac{\epsilon_{\parallel}}{\epsilon_{\perp}} q_{\perp}^2}, \quad (5.1)$$

where  $q_{\parallel}$  and  $q_{\perp}$  are the in-plane and out-of-plane PhP wavevector components. In the case of a  $\text{Le}_1$  mode, these components are real. The out-of-plane wavevector is given by  $q_{\perp} = \pi/d$ , with  $d$  the thickness of the GaSe slab. In the type-II hyperbolic region,  $\epsilon_{\perp} < 0$  and  $\epsilon_{\parallel} > 0$ . Then, at a fixed frequency, the in-plane wavevector  $q_{\parallel}$  increases when the thickness  $d$  decreases. A reduction of the slab thickness therefore shifts the mode toward higher wavevectors and flattens the  $\text{Le}_1$  dispersion curve.

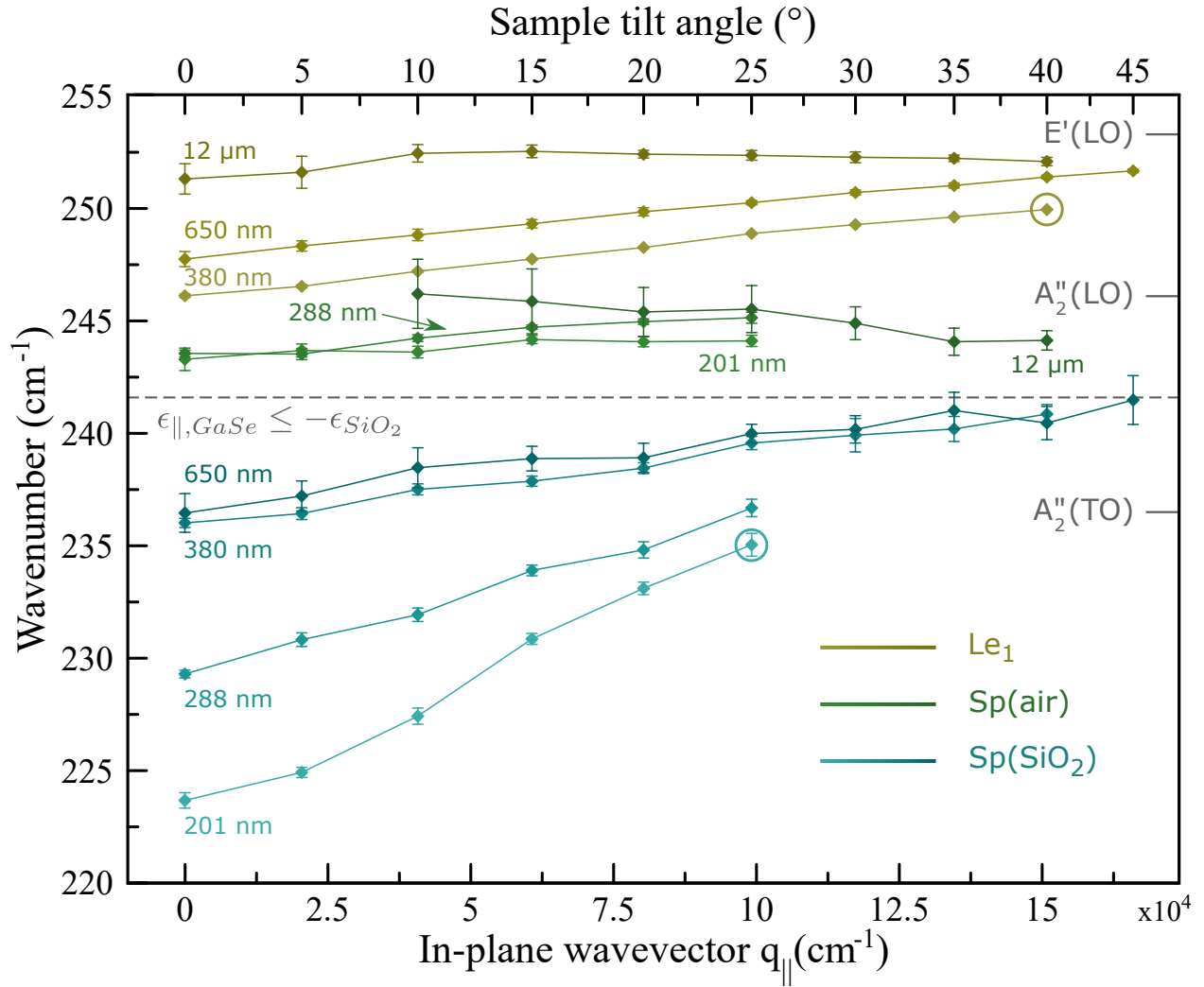


Figure 5.1 PhP dispersions from GaSe samples of different thicknesses. The different colors correspond to the different PhP modes: the Sp(SiO<sub>2</sub>) in blue, the Sp(air) in green and the Le<sub>1</sub> in yellow. The yellow and the blue circles are data points used to evaluate the PhP confinement factor in the text. Darker colors correspond to thicker samples in the color gradient. Pure phonon frequencies are indicated on the right. The horizontal dashed line is the permittivity confinement criterion for the Sp(SiO<sub>2</sub>).

In thicker crystals, the  $\text{Le}_1$  mode dispersion is very steep. It extrapolates to its upper limit frequency at a lower wavevector than the in-plane wavevector resolution imposed by angular broadening effects. The whole dispersion is then contained in the Raman spectra, so the extracted PhP frequency is an average over many polariton states. The measured PhP frequency is therefore close to the upper frequency limit for any sample tilt angle. That leads to a very flat measured  $\text{Le}_1$  mode dispersion, as observed in Fig. 5.1 for the  $12\ \mu\text{m}$  thick sample.

By reducing the crystal thickness, the dispersion of the  $\text{Le}_1$  PhP flattens and extrapolates to its upper limit frequency at a much higher wavevector. As a result, fewer PhP frequencies are measured within the acceptance angle, and the extracted frequency resolution increases. As a result, in thinner samples, the measured  $\text{Le}_1$  frequency at normal incidence decreases down to the  $A''_2(\text{LO})$  frequency. The measured frequency increases to the upper frequency limit for higher tilt angles. This results in a higher measured dispersion slope. This can be observed in Fig. 5.1 by comparing the measured  $\text{Le}_1$  dispersion from samples of different thicknesses. Moreover, the measured in-plane wavevector increases at a fixed frequency as the sample thickness decreases.

The data point from the  $380\ \text{nm}$  sample depicted by a yellow circle is located at a frequency of  $240.9 \pm 0.4\ \text{cm}^{-1}$  and an in-plane wavevector of  $q_{\parallel} = 15 \times 10^4\ \text{cm}^{-1}$ . This PhP is measured between the two frequency limits of the  $\text{Le}_1$  mode, which ensures a high photon-phonon mixed nature. With a vacuum wavevector of  $k_0 = 1.5 \times 10^3\ \text{cm}^{-1}$ , the confinement factor  $\eta = q_{\parallel}/k_0$  is between 89 and 110. The large range of values originates from the uncertainty on the in-plane wavevector induced by the angular broadening. This estimation of the PhP confinement factor is higher than the ones reported in  $\text{MoO}_3$  or hBN. A confinement factor of 60 was indeed measured in a  $\text{MoO}_3$  crystal of thickness  $55\ \text{nm}$  [44]. In a hBN monolayer, in which the PhP vertical confinement is maximized, a confinement factor of 60 was measured by *Dai S. et. al.* [41]. This demonstrates that PhPs from GaSe are interesting because they get more easily vertically confined.

The  $\text{Le}_1$  mode from the same sample is measured at a frequency of  $246.1 \pm 0.1\ \text{cm}^{-1}$  at normal incidence, very close to the lower limit frequency. Angular broadening effects are minimized, and the measured dispersion is expected to match the theoretical  $\text{Le}_1$  dispersion. The PhP group velocity can then be extracted and a value of  $0.014c$  is estimated. This value is approximately 10 times higher than the ones reported in other materials supporting PhPs, revealing that the  $\text{Le}_1$  PhP from GaSe is less dispersive.

### Thickness-dependent dispersion of surface modes

The  $\text{Sp}(\text{air})$  is located between the  $E'(\text{TO})$  and the  $A''_2(\text{LO})$  phonon frequencies. Its field is located at the air/GaSe interface. Like the  $\text{Le}_1$ , the  $\text{Sp}(\text{air})$  extrapolates to the dispersion of light in air at lower wavevectors. At higher wavevectors, it extrapolates to the  $A''_2(\text{LO})$  frequency. Its propagation properties are either the ones of light guided in air or the ones of a pure phonon mode, so this PhP mode has a very low photon-phonon mixed nature. Similarly to what is reported in Fig. 5.1, the dispersion of this mode is flat. The dispersion from the  $12\ \mu\text{m}$  thick sample should not be associated with a negative group velocity. This results from a gain of frequency resolution from increasing the sample tilt angle, which decreases the FWHM of every PhP Raman line. The  $\text{Sp}(\text{air})$  is seldomly observed because of the width of the  $\text{Le}_1$ , which can extend up to the  $A''_2(\text{LO})$  frequency. Moreover, surface irregularities induced by the exfoliation process of GaSe samples can promote losses and inhibit the propagation of the  $\text{Sp}(\text{air})$ .

Like the  $\text{Sp}(\text{air})$ , the  $\text{Sp}(\text{SiO}_2)$  is located between the  $E'(\text{TO})$  and  $A''_2(\text{LO})$  phonon frequencies. The  $\text{Sp}(\text{SiO}_2)$  has field components at the GaSe/SiO<sub>2</sub>/Si interface, which can extend to the air/GaSe interface. At a fixed wavevector, the  $\text{Sp}(\text{SiO}_2)$  has a lower frequency than the  $\text{Sp}(\text{air})$  because of the higher permittivity of SiO<sub>2</sub> and Si. The dispersion of the  $\text{Sp}(\text{SiO}_2)$  extrapolates to the dispersion of light in Si at lower wavevectors, reaching the  $E'(\text{TO})$  frequency. This polariton follows the permittivity confinement criterion depicted in Fig. 5.1 by a gray dashed horizontal line located at a frequency of  $241.6\ \text{cm}^{-1}$ , and this mode extrapolates to this frequency at higher wavevectors. Similarly to the two PhP modes presented above, the expected dispersion is measured for the  $\text{Sp}(\text{SiO}_2)$ .

The combination of dispersion curve flattening with decreasing the sample thickness and angular broadening also explains the variation of the measured dispersion slope of the  $\text{Sp}(\text{SiO}_2)$ . Here, the dispersion flattening arises from the coupling between the two surface modes. This coupling takes a slightly different form for a symmetric and an asymmetric waveguide.

A symmetric waveguide is considered first. Fig. 5.2 displays the  $E_x$  electric field of the two surface modes in two different GaSe waveguides at a frequency of  $240\ \text{cm}^{-1}$ . The first has a thickness of  $80\ \mu\text{m}$  **a-b**) and the second has a thickness of  $5\ \mu\text{m}$  **c-d**). For a slab thick enough, the evanescent fields of the surface modes do not overlap and the two modes are degenerate. When reducing the thickness of the GaSe slab, the evanescent field of the surface mode eventually couple and the degeneracy is lifted. The two modes can be decomposed into an even ( $\text{Sp}_1$ ) and an odd ( $\text{Sp}_2$ ) mode because of the mirror symmetry defined by the  $x-y$  plane at the center of the waveguide. The field distributions of the  $\text{Sp}_1$  and the  $\text{Sp}_2$  are depicted by Fig. 5.2 **c**) and **d**), for a slab thickness of  $5\ \mu\text{m}$ . Due to a node in the distribution of the

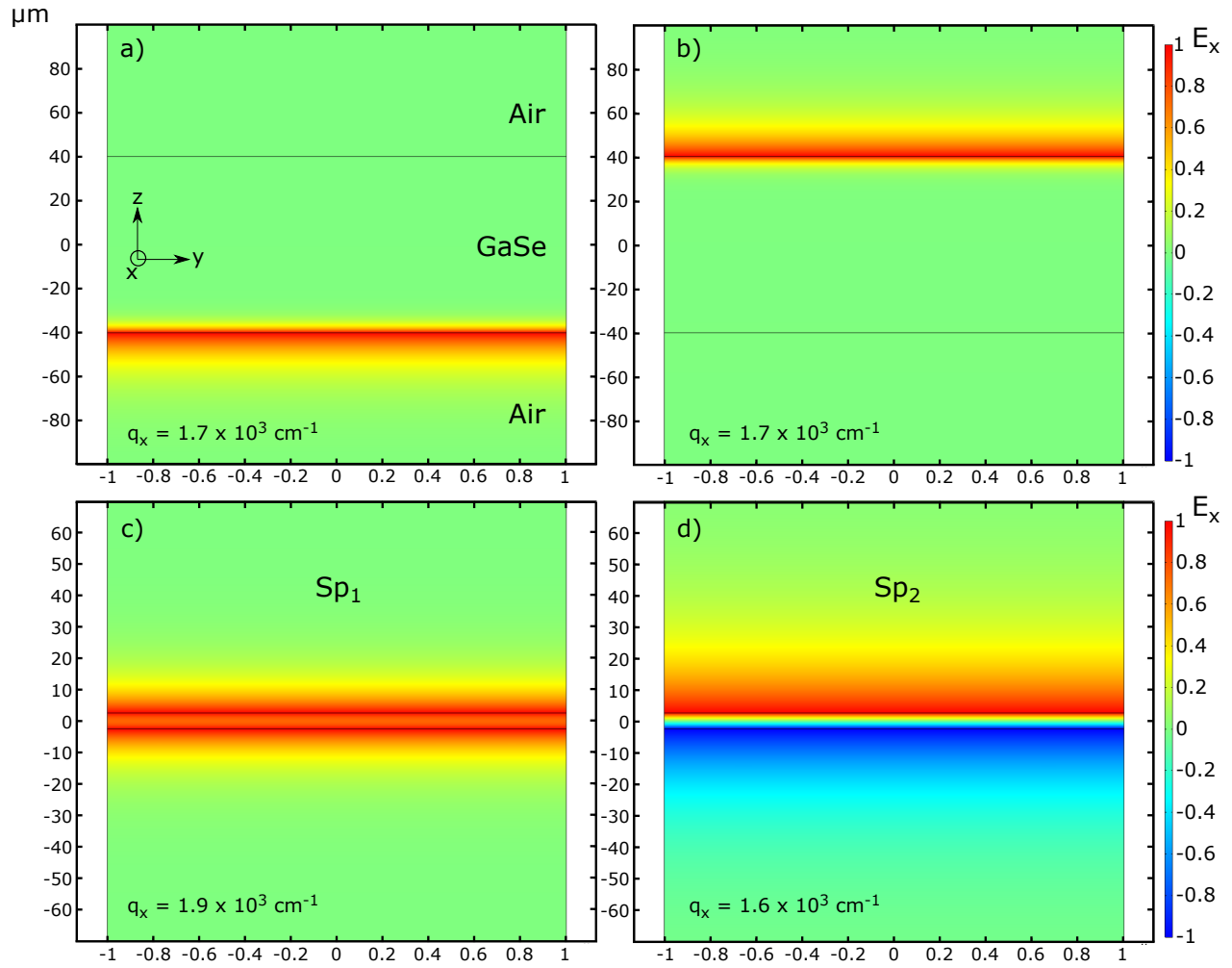


Figure 5.2 Surface PhP field maps from two GaSe waveguides suspended in air. The frequency of the PhP is  $240 \text{ cm}^{-1}$ .  $q_x$  is its calculated in-plane wavevector. The thicknesses of the slabs are **a-b)**  $80 \mu\text{m}$  and **c-d)**  $5 \mu\text{m}$ . In **a)** and **b)**, the two surface modes are degenerate. The degeneracy is lifted in the thinner GaSe slab and **c)** depicts the symmetric  $Sp_1$  mode while **d)** shows the anti-symmetric  $Sp_2$  mode.

Sp<sub>2</sub> electric field, this mode has a lower wavevector ( $q_{\parallel,Sp_2} = 1.6 \times 10^3 \text{ cm}^{-1}$ ) than the Sp<sub>1</sub> ( $q_{\parallel,Sp_1} = 1.9 \times 10^3 \text{ cm}^{-1}$ ).

To better visualize the splitting between the surface modes, Fig.5.3 shows the evolution of the modes dispersion with the thickness of the GaSe slab. When reducing the thickness of the waveguide from 80 to 5  $\mu\text{m}$ , two distinct dispersion branches arise because of the mode fields coupling, as depicted in Fig. 5.3 **a)** and **b)**. Reducing the slab thickness increases the frequency splitting even more, as shown in Fig.5.3 **c)** for a thickness of 500 nm. The dispersion of the lower branch (Sp<sub>1</sub>) flattens as this mode shifts toward higher wavevectors. Inversely, the upper branch (Sp<sub>2</sub>) has a stronger dispersion and saturates quickly to the A<sub>2</sub>(LO) phonon frequency.

In an asymmetric waveguide (GaSe slab deposited on a SiO<sub>2</sub>/Si substrate), the two surface modes are not degenerate because of the different permittivities at the two waveguide interfaces. The electric field of the two surface mode nevertheless couples when they overlap, but the two modes cannot be effectively expressed in an even and odd basis due to the broken reflection symmetry of the waveguide. Despite the less effective coupling, the frequency of the surface modes split and this splitting increases by decreasing the GaSe crystal thickness. This is shown in Fig. 5.4, where the Raman dispersion curves of PhPs is computed for a GaSe thickness of 650, 380 and 201 nm. In this calculation, the angular broadening is ignored. The permittivity damping rate is set to  $\Gamma_{\parallel} = \Gamma_{\perp} = 1.8 \text{ cm}^{-1}$  instead of  $0.5 \text{ cm}^{-1}$  to better reproduce the PhP Raman lines broadening induced by the phonon lifetimes [24]. As can be seen, the dispersion curve of the Sp(SiO<sub>2</sub>) flattens by decreasing the crystal thickness  $d$ . The Sp(air) is difficult to discern because it is located near the A<sub>2</sub>(LO) frequency, very close to the Le<sub>1</sub>.

Thereafter, the angular broadening acts in the same way as described for Le<sub>1</sub> and the measured dispersion slope of the Sp(SiO<sub>2</sub>) increases with decreasing the sample thickness. Because the Sp(SiO<sub>2</sub>) spans a larger frequency range than the Le<sub>1</sub>, the change in its measured dispersion is more pronounced.

For the 201 nm sample, the data point located at a wavevector of  $q_{\parallel} = 10 \times 10^4 \text{ cm}^{-1}$  and depicted by the blue circle in Fig. 5.1 can be used to evaluate the PhP confinement factor. Its frequency of  $235.0 \pm 0.5 \text{ cm}^{-1}$  is far from the Sp(SiO<sub>2</sub>) frequency limits. With the corresponding vacuum wavevector of  $k_0 = 1.5 \times 10^3 \text{ cm}^{-1}$ , the resulting confinement factor  $\eta$  is between 54 and 79. These values are in the range of the ones reported in MoO<sub>3</sub> and hBN. Coupled to its high sensitivity to its dielectric environment, the Sp(SiO<sub>2</sub>) is also of great interest for the development of polaritronic devices.

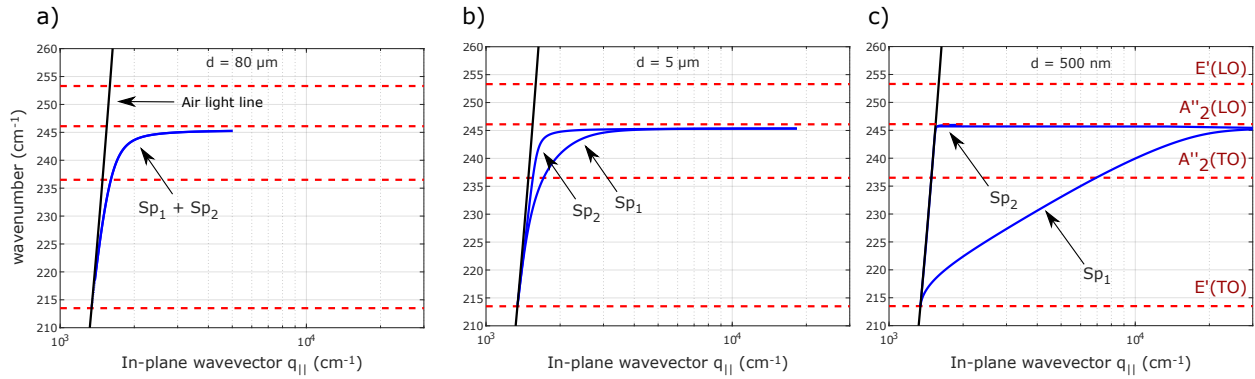


Figure 5.3 Calculated surface PhP dispersion for a GaSe slabs suspended in air with thicknesses of **a)**  $80\ \mu\text{m}$ , **b)**  $5\ \mu\text{m}$  and **c)**  $500\ \text{nm}$ . The in-plane wavevector  $q_{||}$  is expressed on a logarithmic scale to help visualize the evolution of the dispersion near the air light line. The lower branch in **b)** and **c)** corresponds to the symmetric surface mode  $Sp_1$ , while the upper branch is the anti-symmetric surface mode  $Sp_2$ . The solid black line corresponds to the dispersion of light in air. The polar phonon frequencies are indicated by the dashed red lines.

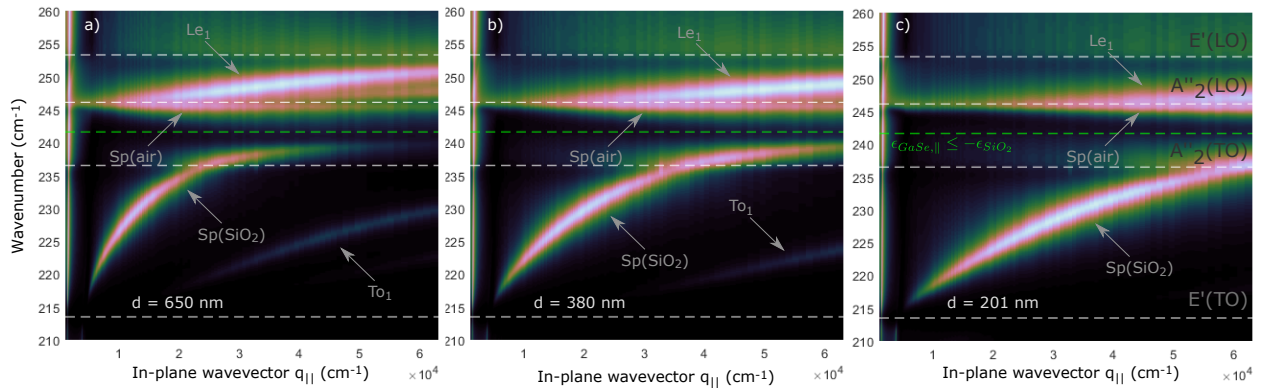


Figure 5.4 Computed PhP Raman dispersion for an asymmetric waveguide (GaSe slab deposited on a  $\text{SiO}_2/\text{Si}$  substrate) with a GaSe thickness  $d$  of **a)**  $650$ , **b)**  $380$  and **c)**  $201\ \text{nm}$ . The bright color corresponds to the presence of Raman signal, on a logarithmic scale. The scaling factor is  $S = 10$ . Dashed horizontal gray lines indicate the position of the pure phonon frequencies. The dashed horizontal green line depicts the permittivity confinement criterion of the  $Sp(\text{SiO}_2)$ .

### 5.1.2 Thickness dependent Raman spectra

The model presented in Sec. 3.4.2 enables the computation of PhP Raman spectra. It was used by *Bergeron* to compute PhP Raman spectra as a function of the GaSe crystal thickness [24]. In order to demonstrate the ability of this model to reproduce and explain experimental data, the calculated spectra are compared with the measured PhP mode frequencies from GaSe samples of various thicknesses.

The results are presented in Fig. 5.5, for a sample tilt angle of  $0^\circ$ . The background corresponds to the calculated Raman intensity presented on a logarithmic scale and with a scaling factor of  $S = 10$ . The effect of the angular broadening, as presented in Sec. 4.2.5, is included. In total, 17 samples with thickness ranging from 30 to 750 nm were measured (14 in this work and 3 from the work led by *Bergeron* in Ref. [24]). The dashed horizontal gray lines are the positions of the pure phonon frequencies<sup>1</sup>. As can be seen, only the  $Le_1$  and the  $Sp(SiO_2)$  are identified in the simulated Raman spectra. The measured mode frequencies are depicted by blue squares and yellow circles, respectively.

The energy of the  $Le_1$  is weakly affected by the variation of the thickness, as only a broadening of its Raman line is observed for sample thicknesses above 500 nm. There is a good agreement between the computed spectra and the reported  $Le_1$  frequencies. Two  $Le$  modes are reported for the 750 nm whose frequencies match the broaden computed spectra.

In the experimental data, it proved difficult to identify the  $Le_1$  mode for samples under 200 nm thick. To explain this, the x-axis intensity polarization of the PhP field is shown in Fig. 5.6 for crystal thicknesses of 2500, 1500, 500 and 200 nm. The considered in-plane wavevector is  $q_{\parallel} = 6 \times 10^3 \text{ cm}^{-1}$ , that corresponds to a sample tilt angle close to  $0^\circ$  in experiments. The permittivity damping rate is set to  $\Gamma_{\parallel} = \Gamma_{\perp} = 1.8 \text{ cm}^{-1}$  [24]. As can be seen, the frequency of the  $Le_1$  decreases between sample thickness of 2500 and 500 nm, and gets closer to the  $A''_2(LO)$  frequency. For a sample thickness of 500 nm and below, the  $Le_1$  field is indistinguishable from the  $Sp(\text{air})$ . The field intensity of both the  $Le_1$  and the  $Sp(\text{air})$  diminishes, and so does their Raman intensity.

As opposed to the  $Le_1$ , the frequency of the  $Sp(SiO_2)$  is highly influenced by the thickness of the GaSe crystal as shown in Fig. 5.5. For crystal thinner than 400 nm, the central frequency of the computed spectra decreases close to the  $E'(TO)$  frequency. The spectra are also broader, especially between sample thicknesses of 100 and 400 nm.

There is also a good agreement between the computed Raman spectra and the measured

---

<sup>1</sup>This calculation was made by *Bergeron* during a former work [24]. The considered GaSe phonons frequencies were slightly different from this actual work.

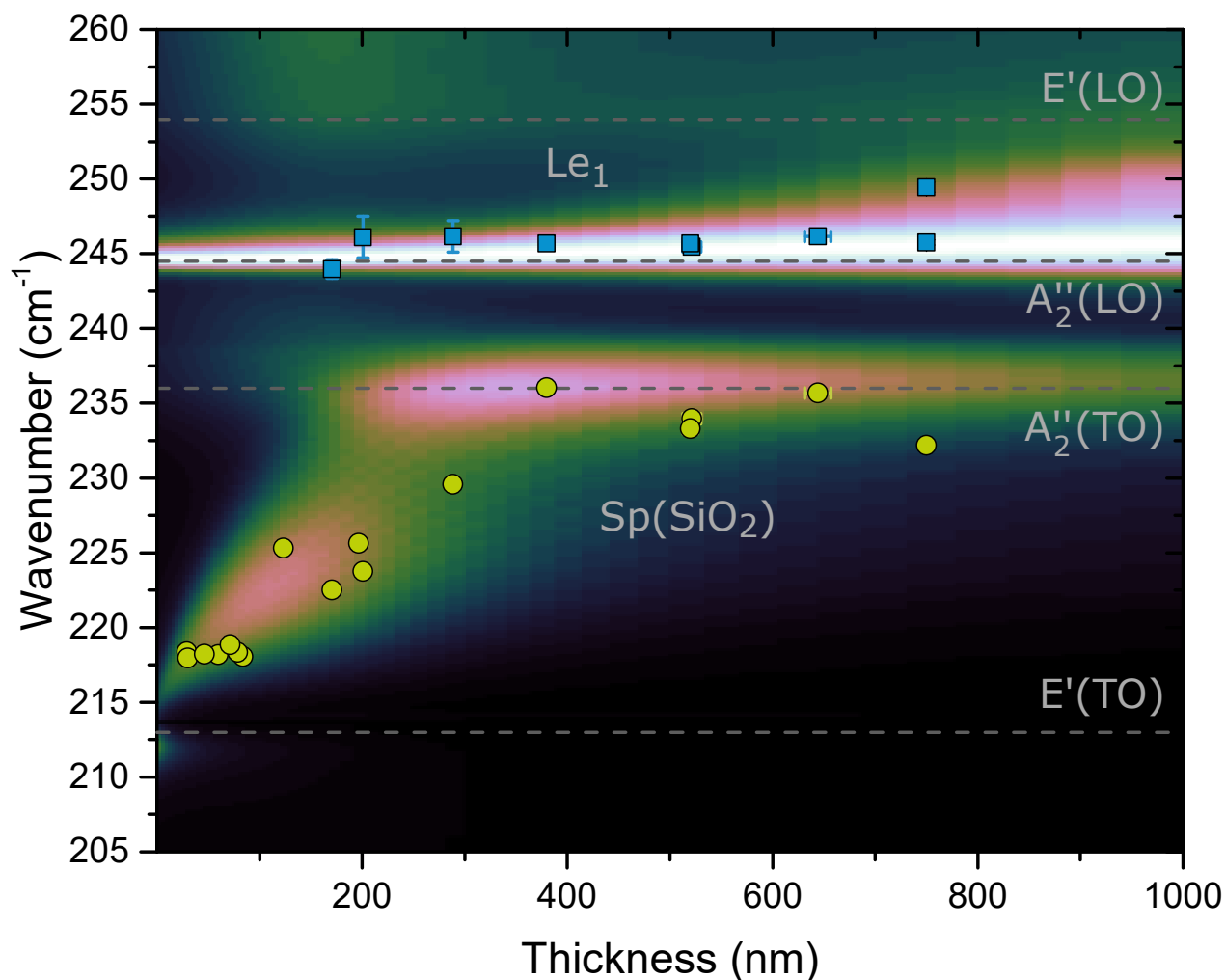


Figure 5.5 Comparison between computed thickness dependent Raman spectra and experimentally measured PhP frequencies. The bright color of the simulated background corresponds to the presence of Raman signal, displayed on a logarithmic scale with  $S = 10$ . Yellow circles and blue squares denote for the measured frequencies of the to the  $\text{Sp}(\text{SiO}_2)$  and the  $\text{Le}_1$ , respectively. Vertical error bars are the uncertainty on the PhP frequency, while the horizontal error bars is the uncertainty on the sample thickness. For most of the data points, the error bar is lower than the symbol size. Dashed horizontal lines indicate the position of the pure phonon frequencies.

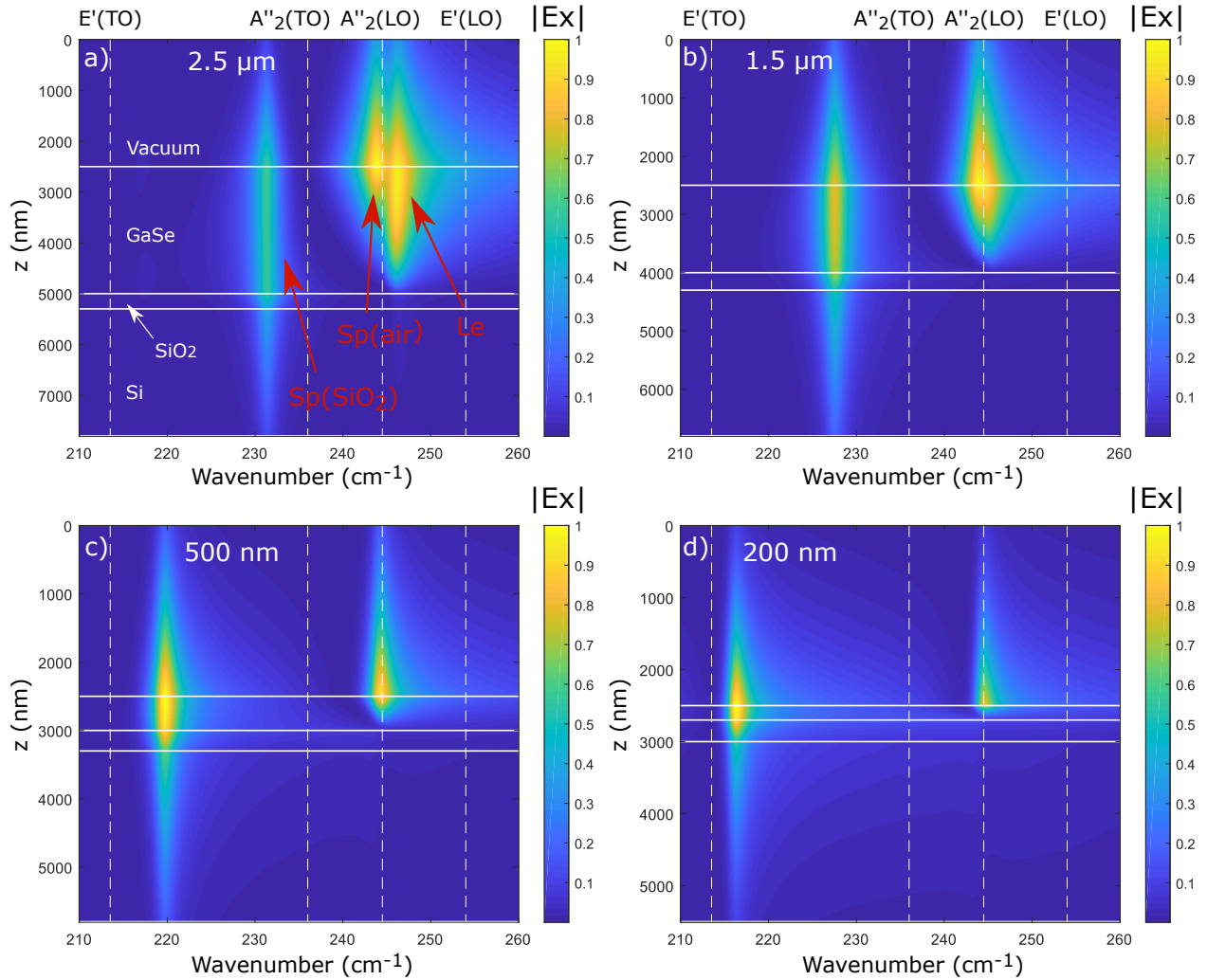


Figure 5.6  $|E_x|$  electric field for asymmetric waveguides with GaSe thicknesses of **a)**  $2.5 \mu\text{m}$ , **b)**  $1.5 \mu\text{m}$ , **c)**  $500 \text{ nm}$  and **d)**  $200 \text{ nm}$ . The amplitude of the field is displayed on a logarithmic scale with  $S=10$ . The considered PhP in-plane wavevector is  $q_{\parallel} = 6 \times 10^3 \text{ cm}^{-1}$ , which corresponds to a sample tilt angle close to  $0^\circ$ . The solid horizontal lines depicts the transitions between the waveguide layers. The dashed vertical lines show the position of the pure phonon frequencies.

Sp(SiO<sub>2</sub>) frequencies. The maximum measured frequency is  $236.0 \pm 0.3 \text{ cm}^{-1}$  and is reported for the sample of thickness 380 nm. The minimum frequency reported is  $217.9 \pm 0.2 \text{ cm}^{-1}$  for a sample thickness of 30 nm. This corresponds to a frequency variation of  $18.1 \pm 0.4 \text{ cm}^{-1}$  (2.24 meV). Moreover, the frequency varies linearly with the sample thickness with a linear coefficient of  $\sim 0.06 \text{ cm}^{-1}/\text{nm}$  between thicknesses of 84 and 380 nm. Finally, the measured frequencies between thicknesses of 30 and 84 nm appears like plateau whereas the Sp(SiO<sub>2</sub>) frequency should keep decreasing as shown by the computed spectra. This discrepancy could not be explained at the moment. The surface roughness of GaSe flakes could have higher impacts when the thickness gets close to the Si thermal oxide thickness (100 nm).

The data reported in this section are of great importance in the experimental characterization of PhPs propagating in thin GaSe crystals and in the validation of the available computational models. It is shown that along with its vertical confinement, the sensitivity of the Sp(SiO<sub>2</sub>) to its dielectric environment can be used to engineer its dispersion, which could be exploited to probe surface impurities or to engineer planar refractive optics by modulating the dielectric properties of the substrate [20, 46, 79]. The high confinement factor measured for the Le<sub>1</sub> and the Sp(SiO<sub>2</sub>) could also improve the interaction strength with electric dipoles [15, 48, 80]. The variation of the PhP mode frequencies with the GaSe sample thickness could be used to estimate the crystal thickness. The Sp(SiO<sub>2</sub>) could be used to probe the crystal thickness between 100 and 380 nm, while the Le<sub>1</sub> could be used between 380 nm and 12  $\mu\text{m}$ .

## 5.2 Polarization resolved Raman scattering of laterally confined phonon-polaritons

The previous section demonstrated that Raman scattering in the backward geometry can be used to probe the PhP dispersion in GaSe thin crystals. It also showed that PhPs can be vertically confined by reducing the sample thickness.

This section demonstrates the possibility of probing laterally confined PhPs in thin GaSe crystals with polarization-resolved Raman spectroscopy. First, polarization-resolved measurements on bulk Si and GaSe are presented to establish the experimental setup polarization control and sensitivity. Then, experimental results of polarization-resolved measurement from rectangular samples are presented. The observed PhP polarization anisotropy is attributed to lateral confinement.

### 5.2.1 Mathematical resources for the data processing

In the following sections, the experimental results will be discussed quantitatively with the help of two mathematical tools. The first is the autocorrelation function. It is utilized to

identify a periodic signal in the presence of noise. The autocorrelation is the correlation between a data set and itself with a delay  $\tau$ . It is defined as

$$\rho(\tau) = \frac{\int_0^{2\pi} P(\psi)P^*(\psi - \tau)d\psi}{\int_0^{2\pi} |P(\psi)|^2d\psi}. \quad (5.2)$$

Here,  $P(\psi)$  corresponds to either the intensity or the frequency of a Raman line at a polarization angle  $\psi$ . The autocorrelation has positive values and  $\int_0^{2\pi} |P(\psi)|^2d\psi$  is a normalization term. The autocorrelation is  $360^\circ$  periodic with  $\rho(0^\circ) = \rho(360^\circ) = 1$ .

In this work,  $P(\psi)$  is either isotropic,  $180^\circ$ -periodic or  $90^\circ$ -periodic, with a possible mixture of these three behaviors. As a result, the autocorrelation is symmetric with respect to  $\tau = 180^\circ$ . For a perfectly correlated signal,  $\rho(0^\circ) = \rho(180^\circ) = 1$  independently of the periodicity mentioned above. In the presence of uncorrelated noise,  $\rho(0) - \rho(180^\circ) = \gamma_{freq,int}$  can be different from 0.  $\gamma_{freq,int}$  quantifies the correlation that has been lost for a delay of  $180^\circ$ . The subscripts *freq* and *int* denote the loss of correlation of a frequency or an intensity polarization scan. For a polarization scan only made of uncorrelated noise and centered around zero,  $\rho(0) = 1$  and  $\rho(\tau \neq 0) = 0$ , which gives a correlation loss of  $\gamma_{freq,int} = 100\%$ . When correlation is added to  $P(\psi)$ , from either a uniform variation or a periodic signal,  $\gamma_{freq,int} < 100\%$ .  $\gamma_{freq,int}$  is a normalized quantity that can be compared between the different measurements.

The autocorrelation reveals the periodicity of the input data set, which helps probe polarization anisotropy in  $P(\psi)$ . An asymmetry in  $P(\psi)$  can also be detected if the periodicity of the autocorrelation deviates from the expected ones. Moreover, the amplitude of the oscillations can be used to measure the polarization contrast. This contrast is defined as the ratio of the maximum and the minimum value of  $P(\psi)$ .

The second mathematical tool is a general parametric function that will be fitted to the polarization response  $P(\psi)$ . This will enable the characterization of the anisotropy presents in the angle-resolved polarization scans. This function writes as

$$P_{mod}(\psi) = C_0 + C_1 \sin(\alpha_1 - \psi)^2 + C_2 \sin(\alpha_1 - 2\psi)^2, \quad (5.3)$$

where  $C_0$ ,  $C_1$ ,  $C_2$  and  $\alpha_1$  are fit parameters.  $C_0$ ,  $C_1$  and  $C_2$  define the amplitudes of a contribution from an isotropic, anisotropic with a  $180^\circ$  periodicity and anisotropic with a  $90^\circ$  polarization response, respectively. These coefficients have values between 0 and 1 and are always normalized such as  $C_0 + C_1 + C_2 = 1$ . Finally,  $\alpha_1$  is a phase term. In experiments, these coefficients are discussed in order to characterize the PhP polarization response.

### 5.2.2 Polarization resolved Raman scattering from Silicon

The mathematical tools presented above are applied to the case of Si in order to test the polarization-resolved measurement system. Si has a diamond-like crystal structure with two atoms per unit cell. It belongs to the  $O_h^7$  space-group and has one Raman-active phonon mode at the center of the Brillouin zone [81]. It is located at a frequency of  $519\text{ cm}^{-1}$ . Its scattering efficiency is relatively high and presents a strong polarization intensity anisotropy.

#### Intensity polarization anisotropy

Due to the Si cubic crystal structure, the Si phonon mode is three-time degenerate at the center of the Brillouin zone. It has a  $T_{2g}$  symmetry and its Raman tensors are [81]

$$\overset{\leftrightarrow}{R}_{T_{2g}}(x) = \begin{pmatrix} 0 & 0 & 0 \\ 0 & 0 & e \\ 0 & e & 0 \end{pmatrix}, \quad \overset{\leftrightarrow}{R}_{T_{2g}}(y) = \begin{pmatrix} 0 & 0 & e \\ 0 & 0 & 0 \\ e & 0 & 0 \end{pmatrix}, \quad \overset{\leftrightarrow}{R}_{T_{2g}}(z) = \begin{pmatrix} 0 & e & 0 \\ e & 0 & 0 \\ 0 & 0 & 0 \end{pmatrix}, \quad (5.4)$$

where  $x, y, z$  denote for the propagation direction and  $e$  is a constant. A half-waveplate is placed on the optical path of both the excitation and scattered signals to rotate their polarization. This rotation is expressed by the following matrix

$$J_\psi = \begin{pmatrix} -\cos(\psi) & \sin(\psi) & 0 \\ \sin(\psi) & \cos(\psi) & 0 \\ 0 & 0 & 0 \end{pmatrix}. \quad (5.5)$$

The angle  $\psi$  corresponds to half of the angle between the waveplate fast axis and the incoming light polarization. The Raman intensity as a function of the polarization angle  $\psi$  therefore writes

$$I_{Si}(\psi) \propto \sum_{i=1,2,3} |\mathbf{e}_s \cdot J_\psi^T \cdot \overset{\leftrightarrow}{R}_{T_{2g}}(i) \cdot J_\psi \cdot \mathbf{e}_i|^2. \quad (5.6)$$

In the parallel (subscript  $\parallel$ ,  $\mathbf{e}_s = \mathbf{e}_i^T = (1, 0, 0)$ ) or the crossed (subscript  $\perp$ ,  $\mathbf{e}_i^T = (1, 0, 0)$ ;  $\mathbf{e}_s = (0, 1, 0)$ ) polarization configuration, this expression simplifies to

$$I_{Si}(\psi)_{\parallel,\perp} \propto |\sin(\alpha_{\parallel,\perp} - 2\psi)|^2. \quad (5.7)$$

$\alpha_{\parallel,\perp}$  denote for the angle made between the polarizer and the analyzer in the parallel ( $\alpha_{\parallel} = 0^\circ$ ) or in the crossed ( $\alpha_{\parallel} = 90^\circ$ ) configuration. With Eq. 5.3, Eq. 5.7 is retrieved by setting  $C_0 = C_1 = 0$  and  $C_2 = 1$ , with  $|\alpha_{1,\perp} - \alpha_{1,\parallel}| = 90^\circ$ .

A polarization-resolved Raman intensity scan from a [100] cleaved Si sample is presented in Fig. 5.7. It is measured at normal incidence ( $\theta = 0^\circ$ ) and ambient temperature. Green and red diamonds are data points from the parallel and crossed configuration. The intensities are normalized by the maximum value extracted from the parallel configuration. During the experiment, the angle step was  $1^\circ$ , but it is increased to  $5^\circ$  in the diagram for clarity.

Eq. 5.3 is fitted to the data and the resulting curves are depicted by the solid lines. As can be seen, the four-fold symmetry is retrieved and there is a good agreement with the measured intensities. For the parallel configuration, the extracted parameters are  $C_{0,\parallel} = 0.035$ ,  $C_{1,\parallel} = 0.030$ ,  $C_{2,\parallel} = 0.935$ , and  $\alpha_{1,\parallel} = 42.5^\circ$ . As expected, the coefficients associated with an isotropic ( $C_0$ ) and a  $180^\circ$ -periodic anisotropic ( $C_1$ ) response are close to zero. In contrast, the coefficient associated with a  $90^\circ$  periodicity ( $C_2$ ) is close to one. The phase coefficient  $\alpha_{1,\parallel}$  is compared below with the one extracted from the crossed polarization response. In the crossed configuration, the extracted coefficients from the fit of Eq. 5.3 give  $C_{0,\perp} = 0^2$ ,  $C_{1,\perp} = 0.027$ ,  $C_{2,\perp} = 0.973$ , and  $\alpha_{1,\perp} = 136.4^\circ$ . Again, the  $C_0$  and  $C_1$  coefficients are close to zero while the  $C_2$  dominates. These values define the references of a perfectly symmetric four-lobed polarization response. The phase offset between the two configurations is  $|\alpha_{\parallel} - \alpha_{\perp}| = 94^\circ$ . This corresponds to an error of approximately 4% with the theoretical value of  $90^\circ$  and shows good experimental control of the excitation and scattered polarizations.

In Fig. 5.7, an intensity factor of 2.5 between the parallel and the crossed intensity amplitudes is observed. The Raman intensity from the crossed polarization was always lower than that of the parallel configuration because of the lower signal reaching the camera sensor. Finally, a contrast ratio of 33:1 and 284:1 between the higher and the lower measured intensities of the parallel and crossed configurations are extracted, respectively. The significant difference between these two ratios is explained by the half-waveplate retardation value of 0.53, different from the theoretical value of 0.50. This deviation decreases the intensity contrast of the scan made in the parallel configuration. The intensity contrast is nevertheless very satisfying and demonstrates the high sensitivity of the polarization-resolved Raman instrumentation.

---

<sup>2</sup>Any fit parameter with a value below 0.001 is considered as 0.

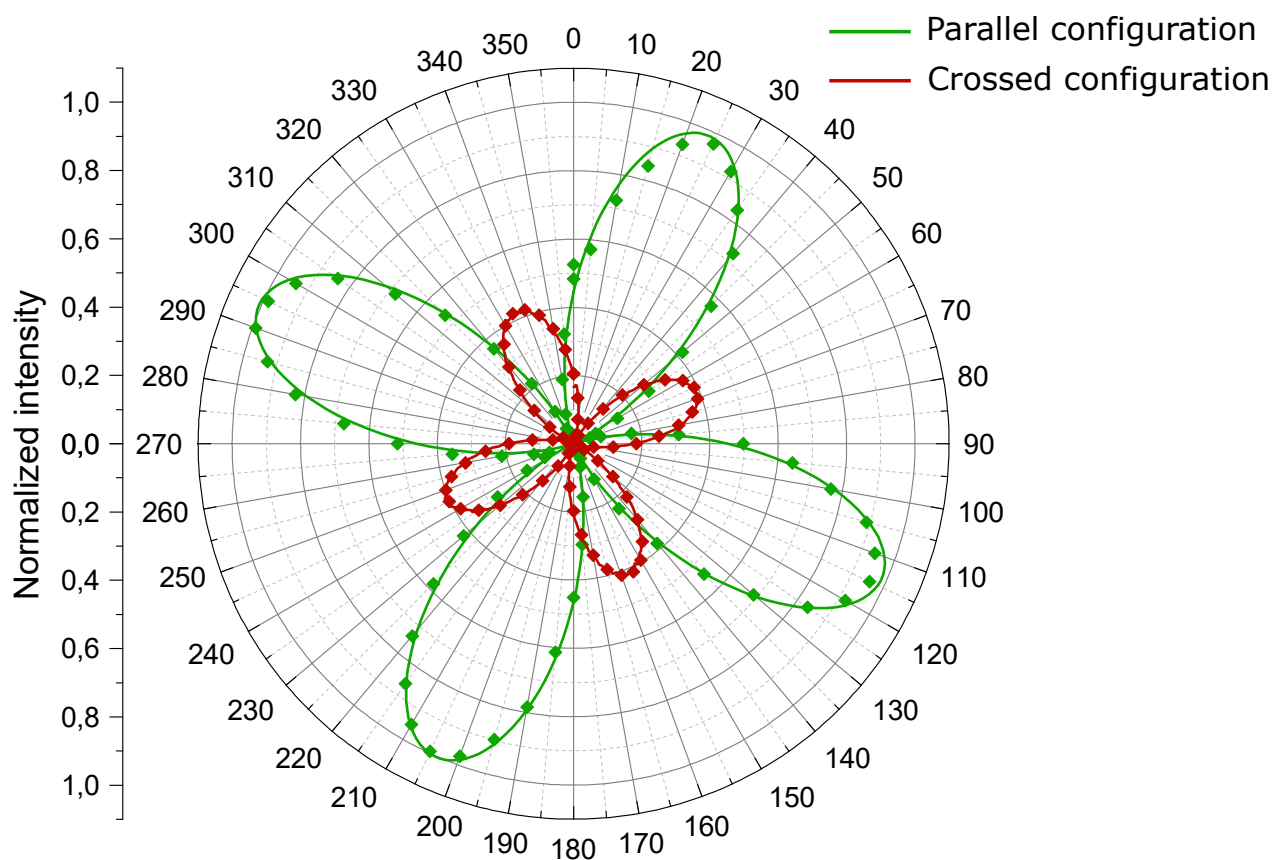


Figure 5.7 Polarization-resolved Raman intensity from a [100] cleaved Si sample at normal incidence and ambient temperature. The intensity is normalized by the higher value reported in the parallel configuration. The green and red diamonds correspond to the parallel and the crossed configuration, respectively. The solid lines are a fit of Eq. 5.3 to the data.

## Frequency polarization anisotropy

In the same way as for the vertical confinement of PhPs, the lateral confinement of PhPs can be probed by measuring frequency shifts. The sensitivity of the polarization instrumentation to the Raman lines frequency variations is evaluated with the Si phonon mode. The frequency of this phonon is not expected to change and therefore has an isotropic polarization response. The Si substrate lateral dimension is large enough (many centimeters) to prevent any spatial confinement effects.

The frequencies are extracted from the intensity scan from Fig. 5.7. The resulting polarization diagram is shown in Fig. 5.8, with the solid green and red lines corresponding to the parallel and crossed configurations. The radial coordinate indicates the frequency deviation from the smallest reported value. This metric is very sensitive to noise, but it is nonetheless suitable to display the frequency variation of multiple Raman lines and identify periodic patterns. Some data points were removed from the diagram to avoid irrelevant phonon frequencies extracted from regions where the Raman intensity is close to zero.

As shown in Fig. 5.8, the evolution of the frequency offset is isotropic with a few variations. The polarization angles associated with a higher frequency offset are regions with a weak Raman intensity. The associated uncertainty is therefore much higher ( $\pm 0.6 \text{ cm}^{-1}$ ) than that extracted from a sufficient Raman intensity ( $\pm 0.02 \text{ cm}^{-1}$ ). The standard variation extracted from the frequency variation, excluding the outlier data points, is  $0.02 \text{ cm}^{-1}$  for the two configurations. This defines the lowest variation of frequency measurable by the instrumentation.

The fit of Eq. 5.3 is not displayed in the figure for clarity. The extracted  $C_0$  coefficients for the parallel and crossed configurations are 0.812 and 0.922 respectively, revealing an isotropic polarization response. The difference between the coefficients of the two configurations is due to outliers. The value of the other parameters are  $C_{1,\parallel} = 0.138$ ,  $C_{2,\parallel} = 0.050$  and  $C_{1,\perp} = 0.078$ ,  $C_{2,\perp} = 0$ . As a result, any  $C_1$  and  $C_2$  values lower than 0.138 and 0.050 demonstrate a dominant isotropic frequency response.

## Correlation of the measured polarization response

Fig. 5.9 displays the autocorrelation of the intensity and frequency shift of the Si polarization response presented above. As the results are similar for the two polarization configurations, only the parallel configuration is presented. The data points are depicted by diamonds, each connected by a solid line. The data points are displayed every  $4^\circ$  for clarity.

The red curve represents the autocorrelation on the normalized Raman intensity from Fig.

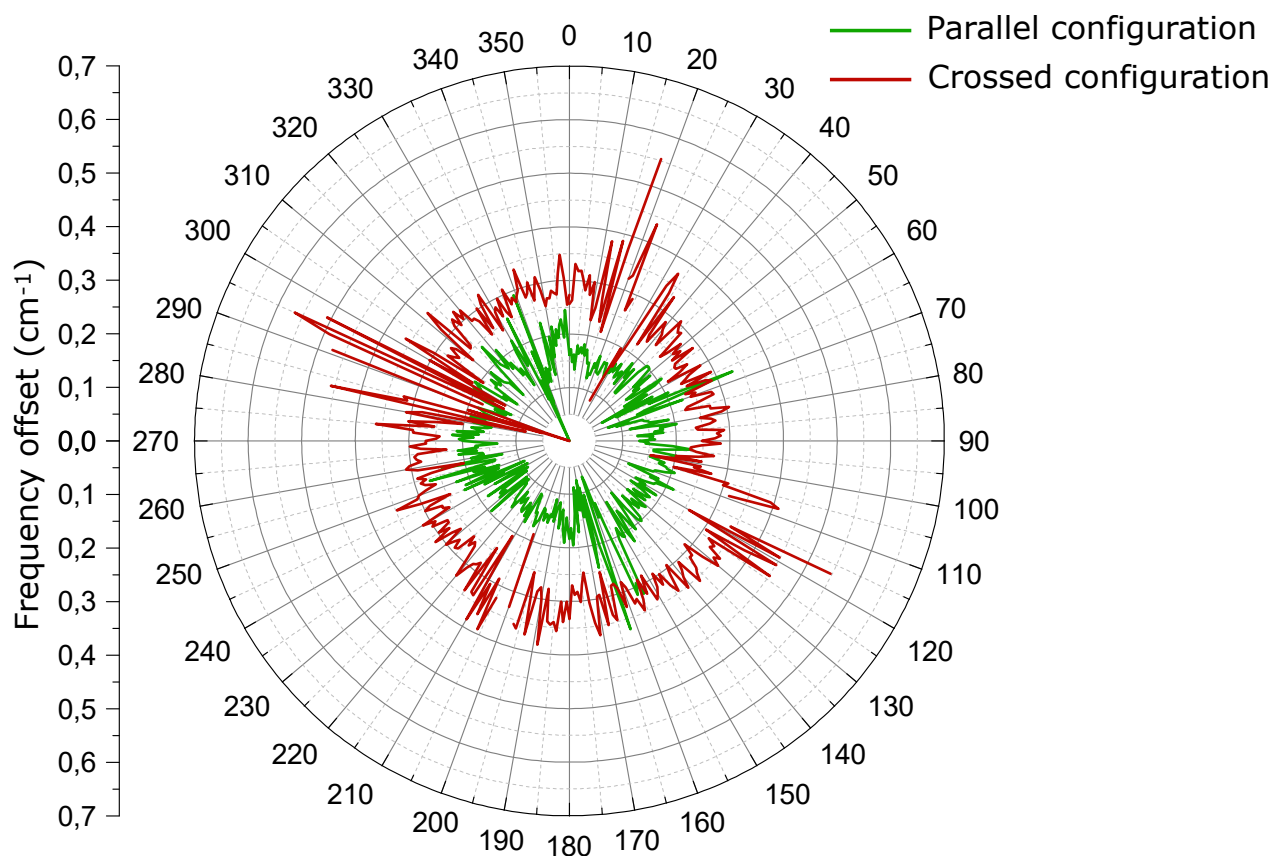


Figure 5.8 Phonon frequency polarization anisotropy from a [100] cleaved Si sample, at normal incidence and ambient temperature. The solid green and red lines denote for the parallel and the crossed configurations. The radial coordinate corresponds to the distance from the lower reported frequency for each configuration. To avoid irrelevant frequencies associated a very low Raman intensity, some data points have been removed.

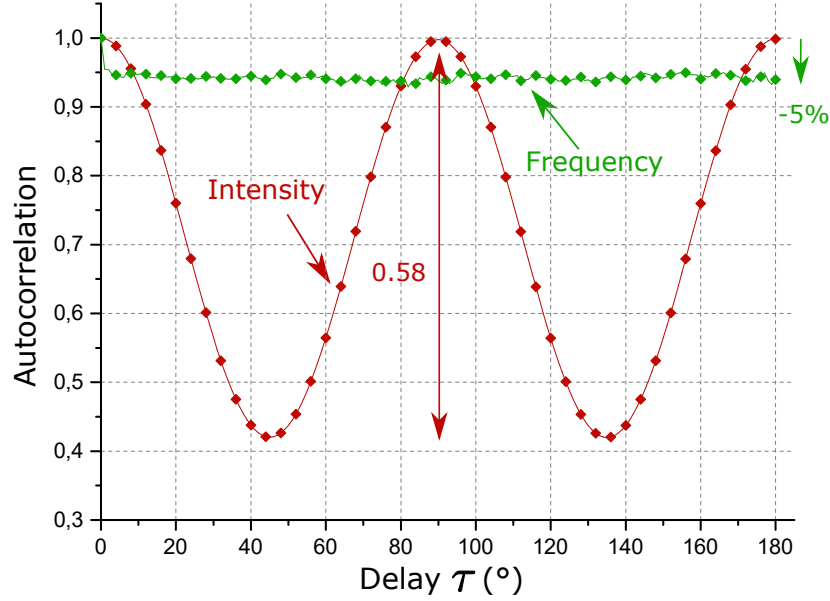


Figure 5.9 Autocorrelation of the intensity and frequency Si polarization response from the parallel configuration data set of Fig. 5.7 and 5.8. The angle step was  $1^\circ$  in the experiment, but the data points are displayed every  $4^\circ$  for clarity.

5.7. The autocorrelation has a periodicity of  $90^\circ$  which reproduces the four-lobed polarization anisotropy of the Si phonon mode. However, the oscillation amplitude is not 1 because of the polarization lobes finite width, leading to a non-zero autocorrelation for delays of  $45^\circ$  and  $135^\circ$ . As a result, the observed amplitude is 0.58.

A very low loss of correlation of  $\gamma_{int} = 0.12\%$  is extracted. This illustrates the small contribution of uncorrelated noise within the Raman intensity and demonstrates that the observed oscillations primarily originate from the crystal scattering properties. Moreover, the difference between the autocorrelation at delays of  $180^\circ$  and  $90^\circ$  quantifies the presence of a  $180^\circ$ -periodic pattern in the polarization response. In the case of Raman intensity from bulk samples, this is attributed to the residual birefringence within the polarization instrumentation. Here,  $\rho(180^\circ) - \rho(90^\circ) = 0.001$  and depicts a very low amount of birefringence.

The green curve presents the autocorrelation calculated on the frequency offsets from Fig. 5.8. For this calculation, all the data point including outliers were kept. It drops rapidly after an angle delay of  $2^\circ$  to a constant value of 0.95. These demonstrate that the observed fluctuations are highly uncorrelated and that the frequency variation is uniform. The frequency shift spikes with a periodicity of  $90^\circ$  observed in Fig. 5.8 at polarization angles of  $70^\circ$ ,  $160^\circ$ ,  $250^\circ$  and  $340^\circ$  are not found in the autocorrelation. This reveals the robustness of this tool to identify periodic signal in the presence of noise. The loss of correlation on the frequency

offset is  $\gamma_{freq} = 5\%$  and demonstrates that the correlation, mainly attributed to the isotropic response, is well conserved even for high delays.

### 5.2.3 Polarization-resolved Raman scattering from bulk GaSe

In wide GaSe crystals, the polarization-resolved Raman response of phonons and PhPs is expected to be isotropic due to the in-plane crystal symmetry. Any observed asymmetry can then be attributed to the imperfection of the polarization instrumentation. Again, only the results for the parallel configuration are presented.

#### Intensity polarization anisotropy

Fig. 5.10 presents the polarization-resolved Raman intensity from a GaSe sample with a lateral dimension of a few millimeters and a thickness of  $12\mu\text{m}$ . The measurement was performed under normal incidence and at ambient temperature. The normalized Raman intensity of the  $A'^3_1$  and  $E'(TO)$  phonons is depicted in red and green while the  $Le_1$  polariton intensity is depicted in blue. The solid curves correspond to the fits of Eq. 5.3 to the data.

The intensity of the two phonons decreases by 10% when the polarization angle deviates by  $\pm 90^\circ$  from their maximum intensity. This results in a low  $180^\circ$  symmetry in the intensity profile with a  $90^\circ$  phase shift between the two phonon scans. The two  $A'^3_1$  lobes are aligned along the  $0^\circ$ - $180^\circ$  axis, while the  $E'(TO)$  are aligned along the  $90^\circ$ - $270^\circ$  axis. The response from these two phonons should be perfectly isotropic. The observed discrepancies are explained by the retardation of the imperfect half-waveplate (0.53 instead of 0.5). Finally, the intensity of the  $Le_1$  fluctuates by 20%, but the polarization response is still mainly isotropic.

The extracted coefficients illustrate the dominant isotropic response of the polarization scan as  $C_0$  values of 0.913, 0.918 and 0.892 are extracted for the  $A'^3_1$ ,  $E'(TO)$  and  $Le_1$  modes, respectively. The lower  $Le_1$  parameter depicts a less isotropic response. It is attributed to higher intensity uncertainty due to the lower polariton scattering efficiency. For the two phonons, the  $C_{1,2}$  parameters are lower by one order of magnitudes compared to the  $C_0$  coefficient and are then negligible. For the  $Le_1$  polariton,  $C_1$  and  $C_2$  are 0.048 and 0.070. For the intensity polarization response, higher  $C_1$  and  $C_2$  values will be used to confirm the presence of periodic modulations of  $180^\circ$  and  $90^\circ$ .

The autocorrelation calculated on the data of Fig. 5.10 is presented in Fig. 5.11. As can be seen, the autocorrelation value is close to 1 for the two phonon modes and the  $Le_1$  polariton. The scale was adapted in order to better capture the very small variations.

The autocorrelation retrieves the two-fold symmetric polarization response observed in Fig.

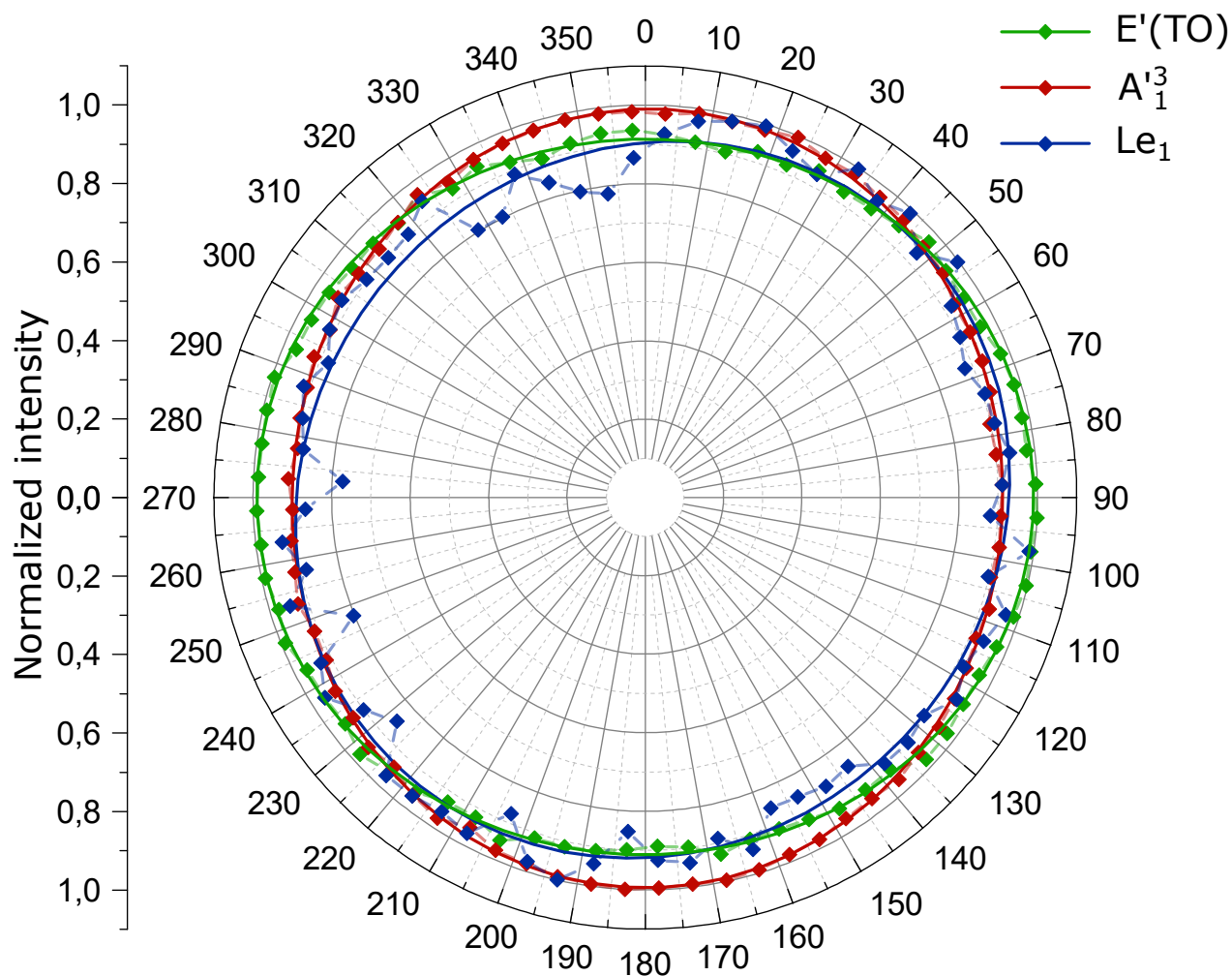


Figure 5.10 Polarization-resolved Raman intensity from a GaSe sample with a lateral dimension of a few millimeters and a thickness of  $12\ \mu\text{m}$ , in the parallel configuration. The measurement was made at normal incidence and ambient temperature. Raman intensity from the  $E'(TO)$  and the  $A_1^3$  phonons is depicted in green and red, while the  $Le_1$  polariton is depicted in blue. Each curve is normalized by the maximum intensity of the associated mode. Diamonds, connected by dashed line, correspond to experimental data. The solid curves correspond to fits of Eq. 5.3 to the data.

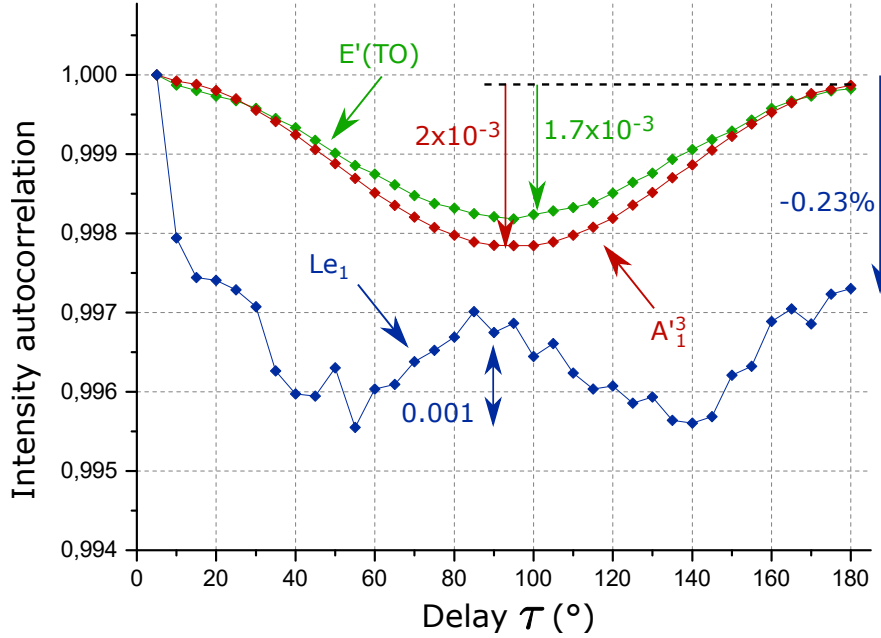


Figure 5.11 Autocorrelation of the polarization-resolved Raman intensity from the GaSe sample presented in Fig. 5.10. The green and red curves show the autocorrelation of the  $E'(TO)$  and  $A_1^3$  phonons, while the autocorrelation of the  $Le_1$  polariton is shown in blue.

5.10 for both phonons. The lower oscillation amplitude of the  $E'(TO)$  mode compared to  $A_1^3$  denotes a slight difference in the contribution of the birefringence in the intensity measurement because of the phonons different frequencies. Values  $\rho(180^\circ) - \rho(90^\circ)$  of  $2 \times 10^{-3}$  and  $1.7 \times 10^{-3}$  are extracted from the autocorrelation. The birefringence contribution to the intensity modulation is therefore very similar to the one from the Si phonon. It demonstrates that this birefringence comes from the instrumentation. Finally, a loss of correlation of  $\gamma_{int} < 0.02\%$  for the two phonon modes is extracted. This is significantly lower than that for the Si phonon. This can be explained by the much longer integration time used for measurements on GaSe. This helps mitigate the fluctuation of the scattered Raman intensity over time.

The autocorrelation of the  $Le_1$  presents a rapid drop at low delay attributed to higher uncorrelated variations than the phonons. Indeed, a higher correlation loss of  $\gamma_{int} = 0.23\%$  is extracted. The intensity uncertainty of this mode is higher than for phonons because of its lower Raman intensity in the spectra. In addition, an unexpected  $90^\circ$ -periodic pattern is observed. The origin of this pattern is unknown. It is however important to note that its amplitude is very small (0.001). This testifies to the sensitivity of the autocorrelation to periodic signals. As such, this value will be used next as a minimum threshold for which a polarization anisotropy in intensity polarization scans can be associated to lateral confinement effects.

## Frequency polarization anisotropy

The polarization instrumentation involves the rotation of birefringent optics, that may impact the measured frequencies by affecting the beam path. Because the amplitude of the frequency polarization anisotropy from confined PhPs is small ( $\sim 1 \text{ cm}^{-1}$ ), it is important to characterize the uncertainty in the measurement of frequencies.

Fig. 5.12 shows the frequency offset associated to the polarization-resolved intensity data presented in Fig. 5.10. As depicted in Fig. 5.12 **a**), the phonon frequency exhibits low amplitude variations as a function of the polarization angles. These variations present a standard deviation of  $0.03 \text{ cm}^{-1}$ , comparable to the value extracted from Si. This suggests that the frequency variation from GaSe phonons is primarily attributed to the limited resolution of the polarization instrumentation.

The frequency offset of the  $\text{Le}_1$  polariton is displayed in Fig. 5.12 **b**). Its frequency variation is higher than the phonons, with a standard deviation of  $0.13 \text{ cm}^{-1}$ . The fit of Eq. 5.3 leads to coefficient  $C_0$ ,  $C_1$  and  $C_2$  of 0.553, 0.368 and 0.079. Although the polarization response is mainly isotropic, there is a non-negligible contribution of a  $180^\circ$  periodic modulation. This anisotropy is not observed in the phonon frequency polarization response and indicates that the instrumentation does not induce this effect. Polaritons are very sensitive to their dielectric environment [31]. It is plausible that sample inhomogeneities induce a residual anisotropy. Fortunately, this anisotropy is much weaker than the one induced by lateral confinement, as presented in the next section.

The autocorrelations of the frequency offset are presented in Fig. 5.13. The autocorrelation of the  $\text{A}^3_1$  displays a linear evolution. The origin of this evolution remains unknown. It is ignored next because the frequency of the  $\text{A}^3_1$  does not affect the  $\text{Le}_1$  polariton in the spectra. As expected, the autocorrelation of the  $\text{E}'(\text{TO})$  and  $\text{Le}_1$  modes decreases to a constant value within a low angle delay of  $5^\circ$ . A loss of correlation  $\gamma_{freq}$  of 23 and 12% are extracted for the  $\text{E}'(\text{TO})$  phonon and the  $\text{Le}_1$  polariton, respectively. The autocorrelation of the  $\text{Le}_1$  displays a weak  $180^\circ$  periodicity with an amplitude of 0.05. This value defines the minimum threshold at which a polarization anisotropy (either two or four-fold symmetric) is detected in GaSe frequency scans.

The polarization instrumentation successfully retrieves the expected isotropic polarization response from a large GaSe. This uniform response is explained by the large size of the sample compared to the propagation length of phonons and PhPs. As a result, there is no lateral confinement and the in-plane symmetry of the crystal is preserved.

In the two last sections, the polarization instrumentation was evaluated with the help of the

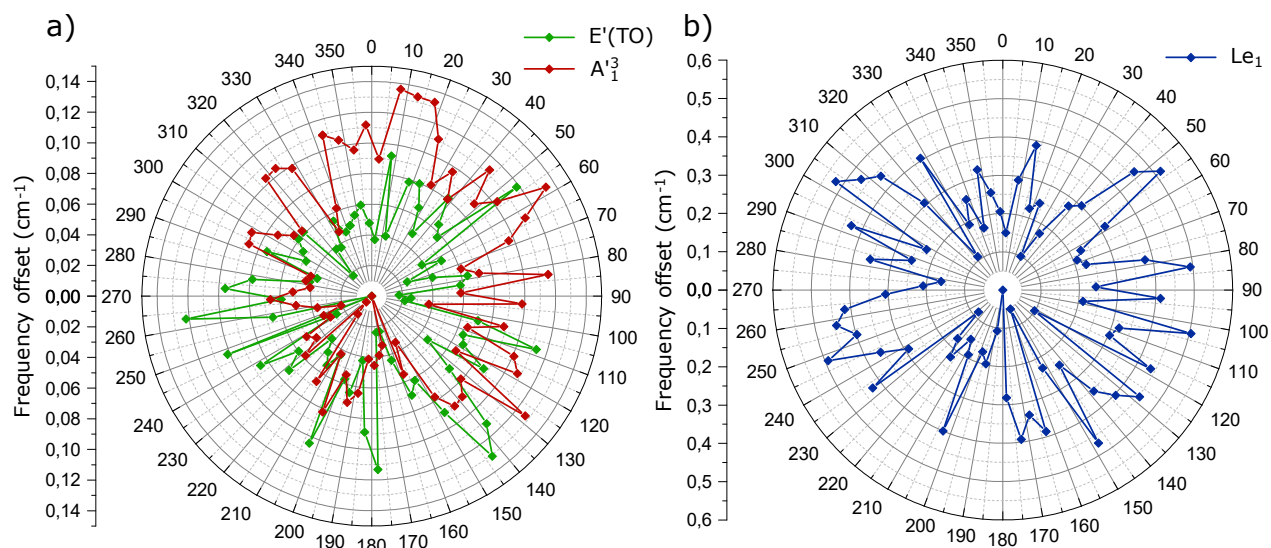


Figure 5.12 Polarization-resolved Raman frequency from a GaSe sample with a lateral dimension of few millimeters and a thickness of 12  $\mu\text{m}$ . The measurements were made at normal incidence and ambient temperature, in the parallel configuration. **a)** the green and the red solid curves correspond to the Raman frequency from the E'(TO) and the A<sup>3</sup><sub>1</sub> phonons, while **b)** the blue solid curve corresponds to the Le<sub>1</sub> polariton. These frequencies are extracted from the intensity scan presented in Fig. 5.10.

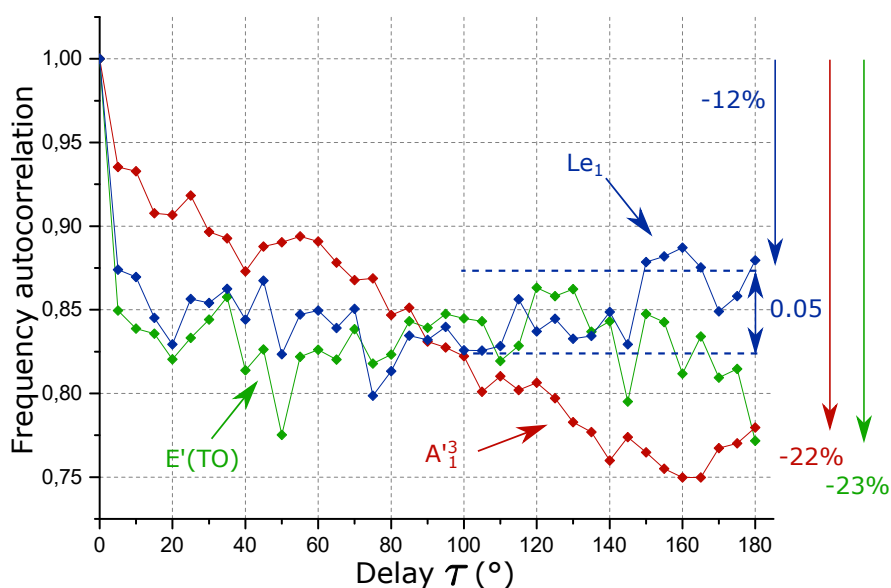


Figure 5.13 Autocorrelation of the frequency offset extracted from the polarization response presented in Fig. 5.12. The green and red curves show the autocorrelation of the E'(TO) and A<sup>3</sup><sub>1</sub> phonons, while the autocorrelation of the Le<sub>1</sub> polariton is shown in blue.

parametric function Eq. 5.3 and the autocorrelation calculated on the polarization scans. Some metrics were extracted in order to characterize the polarization response of rectangular GaSe samples. These metrics are always used in addition to directly comparing the phonons and the polaritons polarization response. First, a  $C_0$  coefficient higher than 0.9 illustrates an isotropic polarization response. For lower values, the  $C_1$  and  $C_2$  coefficients along with the autocorrelation are used to discriminate between a  $180^\circ$  or a  $90^\circ$  periodic polarization response. For intensity polarization scans, periodic oscillations of the autocorrelation with an amplitude greater than 0.001 reveal the presence of a periodicity. A value  $\rho(180^\circ) - \rho(90^\circ)$  lower than 0.005 indicates that the  $180^\circ$  periodic modulation of an intensity scan can be attributed to the residual birefringence induced by the instrumentation. In a frequency polarization scan, periodicity is detected by an autocorrelation oscillation amplitude greater than 0.05. The  $\rho(180^\circ) - \rho(90^\circ)$  value is used to quantify the  $180^\circ$  periodic modulation owed to the different lateral sizes of the sample. Finally, the frequency or intensity correlation loss  $\gamma_{freq,int}$  is discussed case by case since it is closely related to the average value of the polarization scan.

#### 5.2.4 Polarization-resolved Raman scattering from thin rectangular GaSe samples

In rectangular samples, the propagation of PhPs along the sample short and long axes is not equivalent as the in-plane crystal symmetry is broken. In hBN and MoO<sub>3</sub>, PhP propagation lengths of  $\approx 20 \mu\text{m}$  have been reported [31, 34]. For samples of similar dimensions, the PhP undergo lateral confinement effects that result in a frequency shift. Along the diagonal of the sample axes, the distance the PhP must travel to reach each sample boundary is greater. Therefore, lateral confinement effects are minimized along the diagonals of a rectangular sample.

These lateral confinement effects are probed with polarization-resolved Raman scattering by gradually rotating the excitation polarization angle from the sample short to the long axis. In a rectangular sample, the presence of lateral confinement should lead to a PhP polarization response with a  $90^\circ$  periodic pattern. Moreover, the PhP density of states is also redefined by the new boundary conditions. Therefore, a similar polarization anisotropy as for PhP frequencies is expected in intensity polarization scans.

The amount of data is limited and the lateral confinement of PhP could not be extensively characterized similarly to vertical confinement. In total, the polarization response of 12 rectangular samples was probed in this work. From them, 8 presented evidence of lateral confinement effects. The 4 samples set aside had a scattering efficiency too low to perform a

satisfactory polarization scan.

This section presents experimental evidence of laterally confined PhP. The polarization response of 3 samples is exploited with the help of the metrics discussed in the two previous sections. The polarization-dependent Raman measurements were conducted at normal incidence ( $\theta = 0^\circ$ ) and a temperature of 77 K. This lower temperature increases the signal-to-noise ratio and reduces the risk of sample damage caused by the long exposure needed to record a complete polarization scan.

### First sample: intensity polarization response

The first sample presented has a thickness of  $200 \pm 3$  nm and lateral dimensions of  $8.4 \times 25$   $\mu\text{m}$ . The intensity polarization response is presented in Fig. 5.14. An optical image of the sample position during the experiment is displayed in the panel **b**). The turquoise and yellow colors denote the short and long sample axes. Fig. 5.14 **a**) illustrates the normalized Raman intensity as a function of the polarization angle of the  $A^3_1$  and  $E'(TO)$  phonons and the  $Sp(SiO_2)$  and  $Le_1$  polaritons. These intensities are individually normalized by their maximum value. Diamonds correspond to data points and the solid curve is a fit of Eq. 5.3 to the data of the  $Sp(SiO_2)$  and  $Le_1$  polaritons. Finally, the autocorrelation of the intensity polarization diagram is shown in Fig. 5.14 **c**).

The fit of Eq. 5.3 to the  $A^3_1$  phonon leads to coefficient values of  $C_0 = 0.848$ ,  $C_1 = 0.140$  and  $C_2 = 0.012$ . The  $C_0$  coefficient is lower while the  $C_1$  is higher than those from the wide GaSe crystal, which denotes a slightly more important two-lobed polarization response. This small anisotropy can still be attributed to the instrument residual birefringence since the two-lobed pattern is similarly aligned along the  $0^\circ$ - $180^\circ$  axis. This stronger two-fold periodic pattern is also supported by the value  $\rho(180^\circ) - \rho(90^\circ)$  of 0.005, 2.5 times higher than for the wide crystal. Finally, the loss of autocorrelation remains low since  $\gamma_{int} = 0.11\%$ . Concerning the  $E'(TO)$  phonon, the extracted coefficients  $C_0 = 0.932$ ,  $C_1 = 0.035$  and  $C_2 = 0.033$  illustrate an isotropic polarization response. The  $C_0$  coefficient is higher than that extracted from the intensity polarization response from the wide GaSe sample, which illustrates a very uniform response. The loss of correlation of  $\gamma_{int} = 0.05\%$  is also comparable to that from the wide sample. Given the scale at which the autocorrelation is presented, the  $E'(TO)$  autocorrelation is considered uniform. Despite the small loss of isotropy of the  $A^3_1$ , the polarization response of the two phonons is comparable to that from a wide GaSe sample. As expected, reducing the sample dimension does not affect the phonon polarization responses.

As can be seen in Fig. 5.14 **a**), the polarization response of the  $Sp(SiO_2)$  polariton is mainly uniform. The extracted coefficients from the fit of Eq. 5.3 are  $C_0 = 0.874$ ,  $C_1 = 0.074$  and

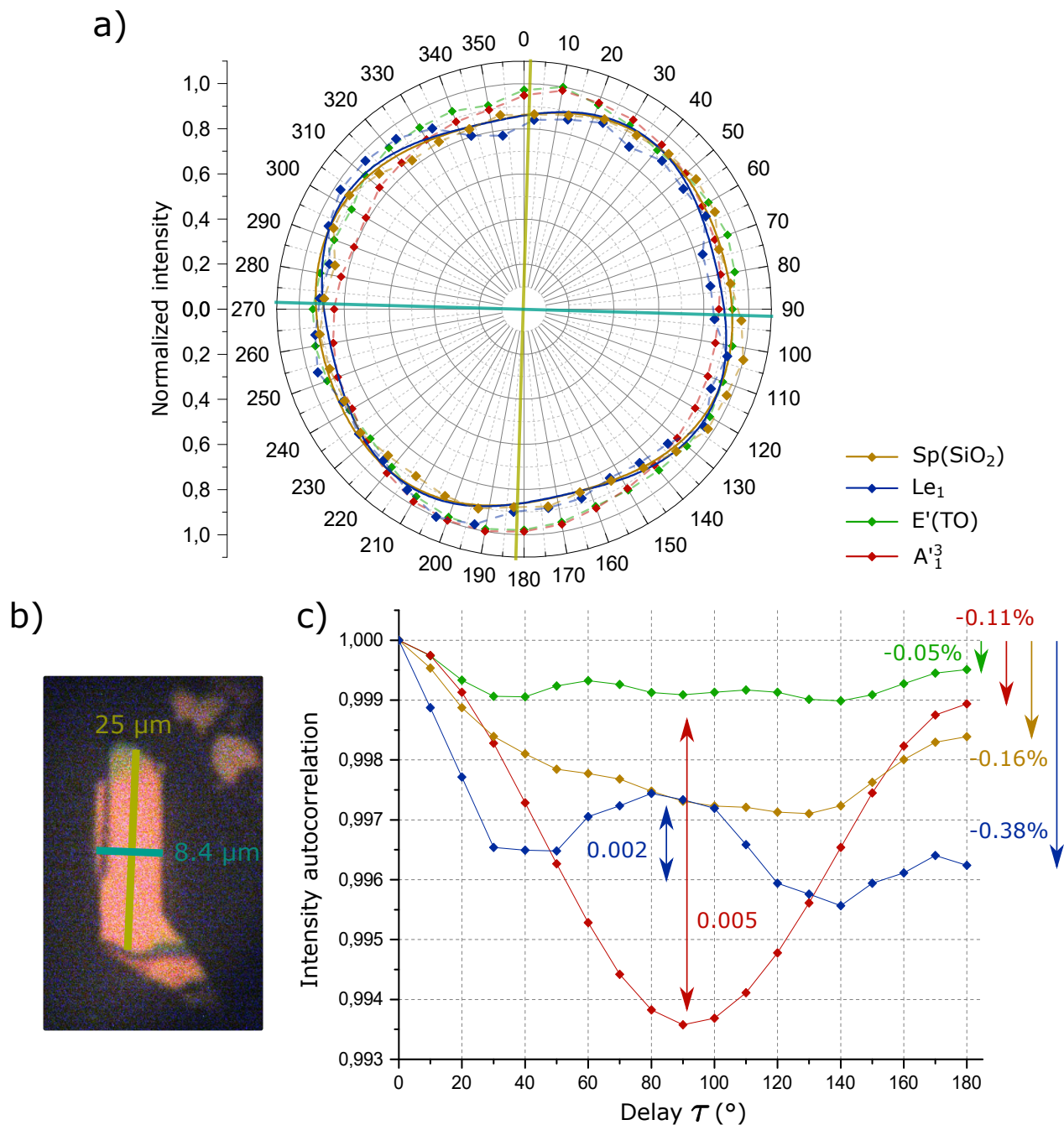


Figure 5.14 Intensity polarization response of the sample of thickness  $200 \pm 3$  nm and lateral dimensions of  $8.4 \times 25 \mu\text{m}$ . **a)** each intensity scans are individually normalized. Diamonds correspond to the experimental data while the solid curves shows a fit of Eq. 5.3 to the data of the  $\text{Sp}(\text{SiO}_2)$  and the  $\text{Le}_1$ . The cyan and yellow solid lines depicts the orientation of the sample short and long axis. These lines are also displayed in **b)**, superimposed on an optical image of the sample. This images shows the position of the sample during experiments. The autocorrelation of the intensity polarization response shown in **a)** is displayed in **c)**.

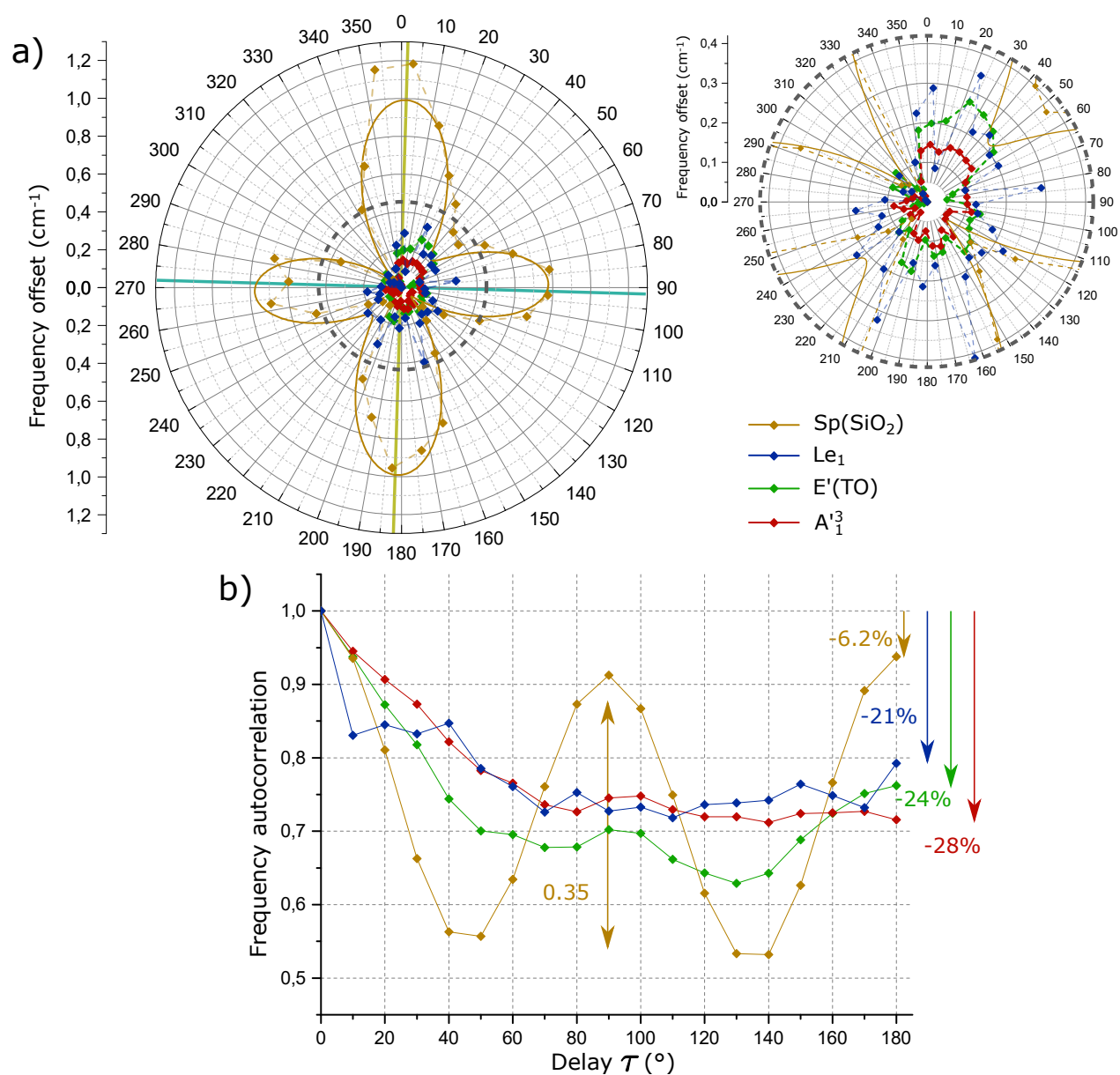


Figure 5.15 Frequency polarization response of the sample of thickness  $200 \pm 3$  nm and lateral dimensions of  $8.4 \times 25$   $\mu\text{m}$ . The frequencies are assimilated to the intensities of the polarization scan of Fig. 5.14. The frequency offset with respect to the lower reported frequency is shown in **a)**, as a function of the polarization angle. The inset zooms onto lower frequency offsets. Diamonds correspond to the experimental data while the solid curves illustrate a fit of Eq. 5.3 to the data of the  $\text{Sp}(\text{SiO}_2)$ . The cyan and yellow solid lines depicts the orientation of the sample short and long axis (see Fig. 5.14 **b)**). The autocorrelation of the polariton frequency offsets is shown in **c)**.

$C_2 = 0.051$ . The  $C_0$  coefficient is slightly below 0.9, which reveals the presence of a weak anisotropy. The  $C_1$  coefficient is similar to that of the phonons from the wide GaSe sample and indicates the presence of a weak  $180^\circ$  periodic modulation pattern. This is supported by the autocorrelation shown in Fig. 5.14 **a)** with  $\rho(180^\circ) - \rho(90^\circ) = 0.001$ , despite the asymmetry depicted by the deviation of  $40^\circ$  of the autocorrelation minimum from its expected localization at  $90^\circ$ . The loss of correlation of  $\gamma_{int} = 0.16\%$  is similar to that from the  $\text{Le}_1$  polariton of the wide crystal. The intensity polarization response of the  $\text{Sp}(\text{SiO}_2)$  is therefore uniform with a weak  $180^\circ$  periodic pattern owing to the residual birefringence. The intensity scan of the  $\text{Sp}(\text{SiO}_2)$  does not reveal the presence of lateral confinement as it is similar to that of phonons.

The polarization response of the  $\text{Le}_1$  intensity shows a faint four-lobed pattern. The extracted coefficients from Eq. 5.3 are  $C_0 = 0.883$ ,  $C_1 = 0.035$  and  $C_2 = 0.083$ . This weak four-lobed polarization response is revealed by the small increase of the  $C_2$  coefficient by 0.013 compared to that of the  $\text{Le}_1$  polariton from the wide GaSe sample. The autocorrelation depicted in Fig. 5.14 **c)** oscillates with an approximately  $80^\circ$  periodicity and an amplitude of 0.002. However, the polarization lobes are neither aligned with the sample axes nor a diagonal of the sample axes. In addition, the irregular periodicity of the autocorrelation indicates that the lobes are mostly asymmetric. There is consequently not enough evidence of polarization anisotropy in the intensity scan that could be attributed to lateral confinement for the  $\text{Le}_1$  polariton.

### First sample: frequency polarization response

The frequency polarization response from the same sample is presented in Fig. 5.15. The frequencies originate from the polarization presented in Fig. 5.14. Fig. 5.15 **a)** illustrates the frequency offset as a function of the polarization angle of the  $\text{A}^3_1$  and  $\text{E}'(\text{TO})$  phonons and the  $\text{Sp}(\text{SiO}_2)$  and  $\text{Le}_1$  polaritons. The inset zooms onto lower frequency offsets depicted by the dashed gray circle. The solid curve is a fit of Eq. 5.3 to the data of the  $\text{Sp}(\text{SiO}_2)$  polariton. The turquoise and yellow colors denote the short and long sample axes as shown in the sample image in Fig. 5.14 **b)**.

Because they have the same polarization response characteristics, the two phonons and the  $\text{Le}_1$  polariton are discussed simultaneously. As can be seen in the inset of Fig. 5.15 **a)**, their frequency offset is much lower than that of the  $\text{Sp}(\text{SiO}_2)$  ( $0.4 \text{ cm}^{-1}$  at most). Eq. 5.3 could not be fitted because the polarization response is very asymmetric and cannot be satisfyingly resolved by the function. Only the autocorrelation on the frequency offsets depicted in Fig. 5.15 **b)** is utilized.

For the  $\text{A}^3_1$  phonon and the  $\text{Le}_1$  PhP, the autocorrelation is very similar and decreases to

a constant value within  $70^\circ$  angle delay. This denotes a small correlation in the frequency variation for low-angle delays, followed by a uniform variation for higher delays. The autocorrelation loss is 28% and 21% respectively, close to that from the frequency autocorrelation of the wide GaSe sample. The autocorrelation of the E'(TO) also decreases up to a delay of  $50^\circ$ . The autocorrelation for higher angle delays does not reveal a well defined symmetry. The value  $\rho(180^\circ) - \rho(90^\circ)$  of 0.06 is slightly higher than that of the  $Le_1$  frequency autocorrelation from the wide sample. Although this illustrates a weak contribution of a  $180^\circ$  symmetric pattern, the correlation loss of  $\gamma_{freq} = 24\%$  is similar to that extracted from uncorrelated frequency variations in the wide sample. Therefore, the evolution of the E'(TO) frequency is assimilated to random frequency variations. As a result, the frequency polarization response of these three modes reveals no significant polarization anisotropy, and there is no indication of spatial confinement for the  $Le_1$  polariton.

As depicted by Fig. 5.15 a), the Sp(SiO<sub>2</sub>) PhP displays a strong anisotropy with a dominant  $90^\circ$  periodicity and a maximum frequency offset of  $1.2 \text{ cm}^{-1}$ . In addition, the polarization lobes precisely align with the sample short and long axis, to within  $1^\circ$ . The minimum frequency shifts are aligned with the sample diagonals, as expected. The parameters extracted from the fit of Eq. 5.3 to the Sp(SiO<sub>2</sub>) polariton are  $C_0 = 0.016$ ,  $C_1 = 0.256$  and  $C_2 = 0.728$ . The  $C_2$  coefficient is 1 order of magnitude higher than the  $C_0$  and nearly 3 times higher than the  $C_1$ , which illustrates the dominant four-fold symmetry pattern. The value of  $C_1$  is close to that extracted from the frequency polarization scan of the wide GaSe crystal for the  $Le_1$  polariton, which reveals a non-negligible modulation by a  $180^\circ$  periodic pattern. These modulations are however not along the same axis (see Fig. 5.12 b) for comparison) and demonstrates that this modulation does not originate from the polarization instrumentation.

The Sp(SiO<sub>2</sub>) autocorrelation is presented in Fig. 5.15 c) and displays a clear  $90^\circ$  periodicity with a correlation amplitude of 0.35. This amplitude is one order of magnitude larger than the residual oscillation observed in the polariton frequency autocorrelation from the large GaSe crystal (see Fig. 5.13). The difference  $\rho(180^\circ) - \rho(90^\circ) = 0.035$  is larger than that of the intensity response from Si, which illustrates the more pronounced  $180^\circ$  periodic pattern observed here. A frequency difference of  $0.3 \text{ cm}^{-1}$  is indeed extracted between the short and long sample axes. Finally, a correlation loss of  $\gamma_{freq} = 6.2\%$  is extracted, much lower than the correlation loss from the polariton frequency offset of the large GaSe crystal. The frequency polarization response of the Sp(SiO<sub>2</sub>) reveals polarization anisotropy that was not present in the large GaSe sample. Hence, this polariton experiences lateral confinement effects along the sample axes.

### First sample: conclusion

The intensity polarization response does not reveal the presence of lateral confinement for the two PhP modes. However, the frequency polarization response of the  $\text{Sp}(\text{SiO}_2)$  polariton is anisotropic with a  $90^\circ$  periodic pattern, and the measured frequency shift is three times larger than that of the two phonons. This anisotropy is illustrated by a dominant  $C_2$  coefficient value over  $C_0$  and  $C_1$ , a  $90^\circ$  periodicity in the autocorrelation with an amplitude of 0.35, and a low loss of correlation of 6.2% within  $180^\circ$  angle delays. Moreover, the maximum frequency shifts of the  $\text{Sp}(\text{SiO}_2)$  are measured along the sample axes, while the minimum frequency shifts are found along the sample diagonals. Therefore, we can conclude that the polarization anisotropy observed for the  $\text{Sp}(\text{SiO}_2)$  PhP arises from the reduction of the sample dimension close to the propagation length of this polariton. As a result, the propagation length can be estimated as the length of the sample long axis, leading to a PhP propagation length of  $25\ \mu\text{m}$ .

In this work, the estimated PhP propagation lengths do not originate from a direct measurement extracted by fitting an exponential decay to a propagating PhP field. The extracted values in this work therefore only provide a first approximation. If confirmed, the PhP propagation length in this sample is comparable to the ones reported in hBN and  $\text{MoO}_3$  (see Table 2.1), which demonstrates interesting polariton guiding properties in GaSe.

### Second sample: intensity polarization response

The second sample presented in this work has a thickness of  $284 \pm 3\ \text{nm}$  and a lateral dimension of  $19 \times 50\ \mu\text{m}$ . Similarly to Fig. 5.14, Fig. 5.16 presents the normalized intensity polarization response of  $A^3_1$  the  $E'(\text{TO})$  phonons and the  $\text{Sp}(\text{SiO}_2)$  and  $\text{Le}_1$  polaritons. The panel **b)** presents an optical image of the sample. The limited field of view of the direct imaging instrumentation of the Raman setup prevents the complete observation of the sample during the setting of the experiment. The sample dimension are characterized using an optical microscope afterward. The autocorrelation on the intensity polarization scan is presented in panel **c)**.

The  $A^3_1$  and  $E'(\text{TO})$  intensity polarization responses are similar to that from the first sample. The extracted coefficients from Eq. 5.3 are respectively  $C_0 = 0.856$ ,  $C_1 = 0.114$ ,  $C_2 = 0$  and  $C_0 = 0.882$ ,  $C_1 = 0.118$ ,  $C_2 = 0$ . These coefficients are close to the one extracted from the  $A^3_1$  intensity scan of the first sample. The autocorrelation also resembles that of the first sample and that from the wide GaSe crystal. The  $180^\circ$  symmetric pattern owing to the residual birefringence is indeed retrieved by the  $\rho(180^\circ) - \rho(90^\circ)$  value of 0.002 and 0.004,



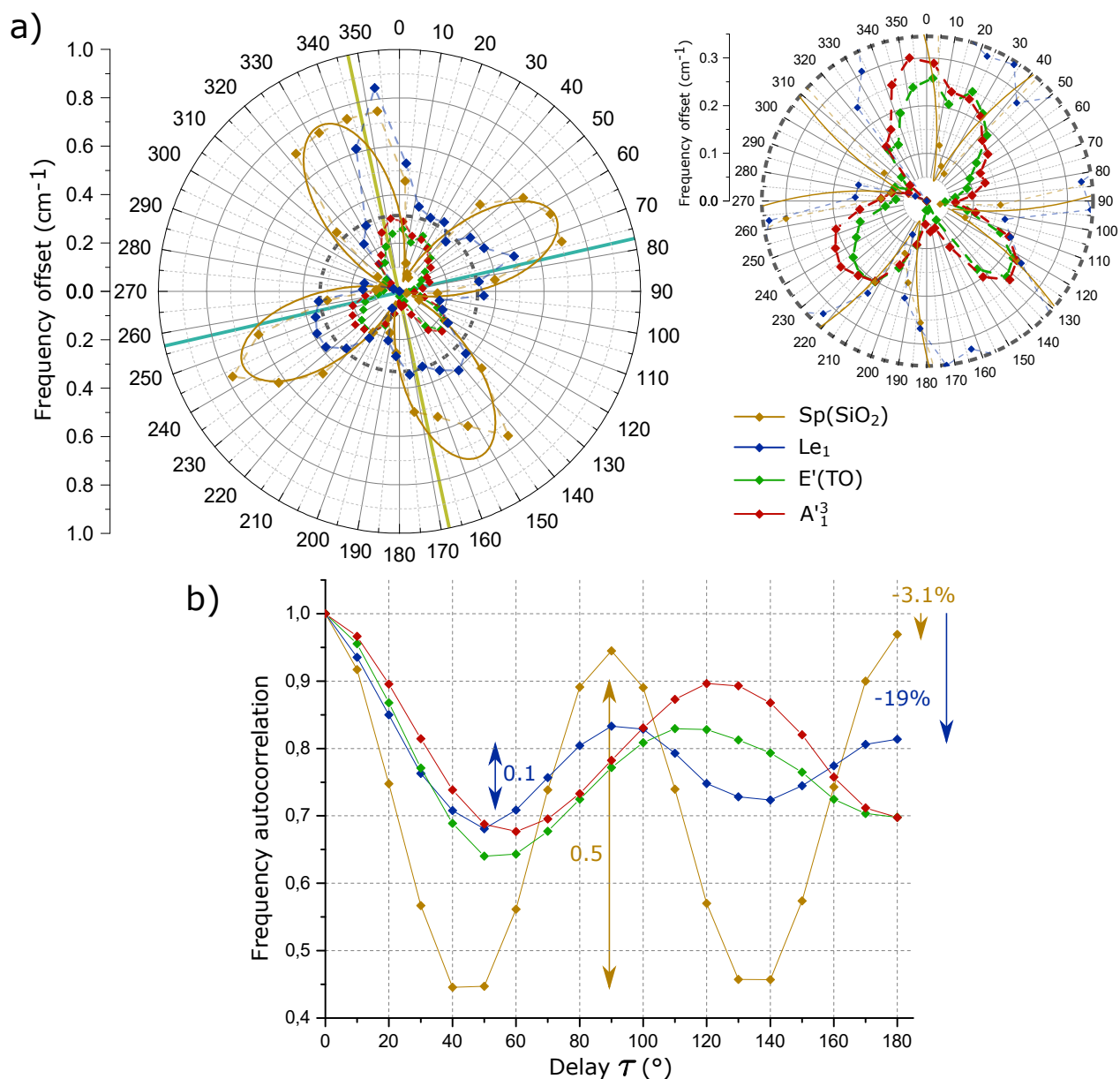


Figure 5.17 Frequency polarization response of the sample of thickness  $284 \pm 3$  nm and lateral dimensions of  $19 \times 50$   $\mu\text{m}$ . The frequencies are assimilated to the intensities of the polarization scan of Fig. 5.16. The frequency offset with respect to the lower reported frequency is shown in **a)**, as a function of the polarization angle. The inset zooms onto lower frequency offsets. Diamonds correspond to the experimental data while the yellow solid curve shows the fit of Eq. 5.3 to the  $\text{Sp}(\text{SiO}_2)$  data. The cyan and yellow solid lines depicts the orientation of the sample short and long axis (see Fig. 5.16 **b)**). The autocorrelation of the polariton frequency offsets is shown in **c)**.

similar to that from the first sample. Finally, the loss of correlation  $\gamma_{int}$  of 0.15% and 0.14% is also very close to what is already reported for the  $A^3_1$  and  $E'(TO)$  polarization response in this work. The usual uniform intensity polarization response with a little modulation attributed to the residual birefringence is measured for the two phonons.

Compared to the first sample, the intensity polarization response of the polaritons presents a noticeable  $90^\circ$  periodic pattern, as shown in Fig. 5.16 **b**). For the  $Sp(SiO_2)$ , the polarization lobes are misaligned with respect to the sample axis by an angle of  $28^\circ$ . Depending on the position of the excitation laser on the sample, the curved sides of the sample may influence the orientation of the polarization lobes and deviate their orientation. This can be verified by repeating the measurement at different sample locations. The extracted fit parameters for this polariton are  $C_0 = 0.820$ ,  $C_1 = 0.070$  and  $C_2 = 0.110$ . The  $C_0$  coefficient is lower than the  $Le_1$  from the first sample, denoting a lesser uniform polarization response. The higher  $C_1$  and  $C_2$  coefficients with  $C_1 < C_2$  illustrate a more anisotropic polarization response dominated by a four-fold periodic pattern. The autocorrelation depicted in Fig. 5.16 **c**) reveals this two-fold symmetric modulation with  $\rho(180^\circ) - \rho(90^\circ) = 0.002$ . This value is the same as the one extracted from the intensity autocorrelation of phonons, so this modulation is attributed to the residual birefringence of the instrumentation. The presence of a four-lobed symmetry is supported by the very symmetric  $90^\circ$  periodicity of the autocorrelation. The amplitude of this periodicity is 0.003, three times higher than that of the wide GaSe crystal  $Le_1$  intensity autocorrelation. Moreover, there is a lower correlation loss  $\gamma_{int}$  of 0.18%. The intensity scan anisotropy of the  $Sp(SiO_2)$  can be attributed to the lower lateral dimensions of the sample.

The polarization lobes of the  $Le_1$  PhP align better with the sample axes than the ones from the  $Sp(SiO_2)$  as a lower deviation of  $15^\circ$  is observed. The fit of Eq. 5.3 to the  $Le_1$  leads to fit coefficients of  $C_0 = 0.774$ ,  $C_1 = 0.045$  and  $C_2 = 0.181$ . The higher  $C_2$  coefficient than that of the  $Sp(SiO_2)$  illustrates an even more pronounced four-fold symmetry pattern. The intensity autocorrelation reveals this stronger anisotropy as the  $90^\circ$  periodic oscillations have an amplitude of 0.01, which is one order of magnitude higher than the polariton from the wide crystal. The residual instrumentation birefringence is again retrieved by the value  $\rho(180^\circ) - \rho(90^\circ) =$  of 0.001. Despite the slightly higher correlation loss  $\gamma_{int}$  of 0.35%, the perfect  $90^\circ$  periodicity, the well defined oscillation pattern of the autocorrelation and the great oscillation amplitude confirm the presence of a four-fold periodic anisotropy in the  $Le_1$  intensity polarization response. This anisotropy is stronger than that of the  $Sp(SiO_2)$  of the same sample and also reveals lateral confinement effects.

## Second sample: frequency polarization response

The frequency offsets associated with the intensity polarization response presented in Fig. 5.16 are shown in Fig. 5.17. The polarization diagram displaying the  $A_1^{31}$  and  $E'(TO)$  phonons and the  $Sp(SiO_2)$  and  $Le_1$  PhPs frequency offsets is shown in Fig. 5.17 a). The inset zooms onto lower frequency shifts. The autocorrelation calculated on the frequency offsets is depicted in Fig. 5.17 b).

The frequency polarization response of the  $A_1^{31}$  and  $E'(TO)$  phonons presents an unexpected  $120^\circ$  periodic pattern. Their maximum frequency shift is  $0.3 \text{ cm}^{-1}$ , lower than that of the two polaritons. This periodicity cannot be resolved by Eq. 5.3. The autocorrelation reproduces this periodicity, with a little deviation of  $5^\circ$  with the position of the maximum expected at a delay of  $120^\circ$ . The oscillation amplitude of 0.2 is one order of magnitude higher than that of the residual oscillation of the  $Le_1$  frequency autocorrelation of the wide GaSe crystal. Finally, the total correlation loss cannot be estimated at  $180^\circ$  because no autocorrelation maximum is expected at this delay for a three-fold periodic pattern. The evolution of the frequency offset is nevertheless regular and illustrates a correlated signal. The origin of this anisotropy cannot be explained by either the rectangular shape of the sample or the polarization instrumentation that can only induce a two or four-fold symmetric pattern. Because this is the only polarization measurement revealing such an anisotropy for the phonons and the observed frequency shift is lower than that of the polariton, this unexpected anisotropy will be set aside.

As shown in Fig. 5.17 a) the  $Sp(SiO_2)$  presents a strong four-lobed pattern with a periodicity of  $90^\circ$ . The maximum frequency shift observed is  $0.8 \text{ cm}^{-1}$ . The frequency polarization lobes are aligned with the lobes from the intensity scan with a deviation of  $15^\circ$ . Moreover, the frequency polarization lobes deviate from  $13^\circ$  to the sample axes. By fitting Eq. 5.3 to the  $Sp(SiO_2)$  polarization response, parameters of  $C_0 = 0.038$ ,  $C_1 = 0.058$  and  $C_2 = 0.904$  are extracted. Here, the  $C_2$  coefficient is higher than  $C_0$  and  $C_1$  by at least one order of magnitude. This illustrates the strong four-lobed polarization response with no modulation by a two-lobed pattern.  $C_2$  is also close to the one from the four-lobed response of the Si phonon, which illustrates the quality of the measured four-lobed frequency anisotropy.

The autocorrelation of the  $Sp(SiO_2)$  frequency offsets is shown in Fig. 5.17 c). It displays a clear  $90^\circ$  periodicity with oscillation amplitudes of 0.5. This amplitude is one order of magnitude larger than the oscillation of the frequency autocorrelation of the wide GaSe crystal. A total loss of correlation of  $\gamma_{freq} = 3.1\%$  is extracted and shows a more correlated signal than the ones of the previous sample. The value  $\rho(180^\circ) - \rho(90^\circ)$  of 0.025 is lower than of the  $Sp(SiO_2)$  of the first sample, which supports the absence of a two-lobed symmetry

modulation. The presence of lateral confinement effects is well established for this  $\text{Sp}(\text{SiO}_2)$  polariton.

The polarization lobes of the  $\text{Le}_1$  are quite asymmetric as depicted by Fig. 5.17 **a**). Indeed, the upper and left polarization lobes are separated by  $110^\circ$  instead of  $90^\circ$ . The intensity and frequency polarization lobes are almost aligned with a deviation of  $20^\circ$ . The  $\text{Le}_1$  has a lower frequency offset amplitude ( $0.5 \text{ cm}^{-1}$ ) than the  $\text{Sp}(\text{SiO}_2)$ , except for the lobe at  $350^\circ$  ( $0.8 \text{ cm}^{-1}$ ). The asymmetry of the polarization response prevents Eq. 5.3 from being satisfyingly fitted as it hardly reproduces the experimental data.

The  $\text{Le}_1$  autocorrelation is shown in Fig. 5.17 **c**). A total loss of correlation of  $\gamma_{freq} = 19\%$  is observed, close to the loss observed in the  $\text{Le}_1$  from the previous sample for which no lateral confinement was observed. Here however, the autocorrelation depicts a periodicity. The second autocorrelation maximum is located at an angle of  $95^\circ$  instead of  $90^\circ$  which is a consequence of the polarization response asymmetry. The amplitude of the oscillations is approximately 0.1, two times larger than the residual autocorrelation oscillations of the polariton frequency from the large GaSe sample. The oscillations decrease over time delays depicting a gradual correlation loss. The evolution of the frequency is therefore correlated within a certain time delay and still suggests the presence of lateral confinement effects.

The different polarization response of the two polaritons implies that lateral confinement effects might affect PhPs modes slightly differently. Fig. 5.17 **a**) depicts the  $10^\circ$  deviation between the  $\text{Le}_1$  and  $\text{Sp}(\text{SiO}_2)$  polarization lobe orientation around polarization angles of  $340^\circ$ . As shown in the optical image in Fig. 5.16 **b**), the sample has a slightly irregular and curved shape. Because surface and guided PhP propagates in different regions of the sample, they can experience lateral confinement effects differently. Here, the asymmetry of the  $\text{Le}_1$  polarization response reproduces the curved lateral shape of the sample, whereas the  $\text{Sp}(\text{SiO}_2)$  still has a very symmetric response. The polariton polarization response seems sensitive to the sample inhomogeneities.

## Second sample: conclusion

In this sample, an intriguing three-fold symmetric frequency polarization response is observed for the two phonons. This symmetry cannot be explained by either the residual birefringence or the rectangular shape of the sample. Moreover, this polarization response is not observed for the polariton. There is no explanation yet for this polarization response, which is set aside because the phonon frequency shifts are 3 times lower than the polaritons.

Concerning the polaritons, both the intensity and the frequency polarization response of the

Sp(SiO<sub>2</sub>) and Le<sub>1</sub> polaritons reveal the presence of a 90° periodic pattern. Moreover, the intensity and frequency polarization lobes are satisfyingly aligned, demonstrating the same origin of the observed anisotropy. The presence of lateral confinement is therefore established and a PhP propagation length of 50 μm can be estimated in this sample. If confirmed by a direct measurement, this value is higher than the ones reported in hBN and MoO<sub>3</sub>.

### Third sample: Intensity polarization response

The third and last sample has much larger dimensions with a thickness of  $820 \pm 1$  nm and lateral dimensions of 88x328 μm. The intensity polarization response is presented in Fig. 5.18 in the same fashion as in Fig. 5.14 and Fig. 5.16.

The intensity polarization scan presented in Fig. 5.18 a) of the A<sup>3</sup><sub>1</sub> and E'(TO) phonons is very similar to that of the first and the second samples. The regression of Eq. 5.3 to these intensities leads to fit coefficients of  $C_0 = 0.921$ ,  $C_1 = 0.079$ ,  $C_2 = 0$  and  $C_0 = 0.883$ ,  $C_1 = 0.103$ ,  $C_2 = 0.014$ , respectively. Moreover, the value of  $\rho(180^\circ) - \rho(90^\circ)$  is 0.002 and 0.004. The intensity polarization response of the two phonons is again isotropic with a weak 180° periodic pattern modulation due to the instruments residual birefringence.

The measured two polariton intensities decrease as a function of the polarization angle as shown in Fig. 5.18 a). This behavior was sometimes observed during a polarization scan, but its origin remains unknown. It is plausible that the sample degrades over time, reducing the scattering efficiency of the polaritons. However, it does not affect the measured frequency since the intensity remains sufficient. The autocorrelation depicted in 5.18 c) reproduces this linear evolution. The surface mode autocorrelation decreases monotonically to a correlation loss of 2.1%, much higher than the usually observed correlation loss of intensity polarization scan. This is a consequence of the linear evolution of the intensity scan. The autocorrelation of the Le<sub>1</sub> reveals a 90° periodicity with an amplitude en 0.004 within its linear decreasing. This is higher than the second sample oscillation amplitude observed in the Sp(SiO<sub>2</sub>) intensity autocorrelation. Despite the strong linear variation here, the Le<sub>1</sub> intensity autocorrelation retrieves a periodic signal even in the presence of a strong perturbation. The correlation loss of 0.89% is also higher than usually observed for the intensity scans and is similarly caused by the linear variation of the polarization scan. It can be concluded that the intensity scan of the Sp(SiO<sub>2</sub>) is isotropic. In contrast, the Le<sub>1</sub> intensity comprises a weak 90° periodic anisotropy owing to lateral confinement effects.

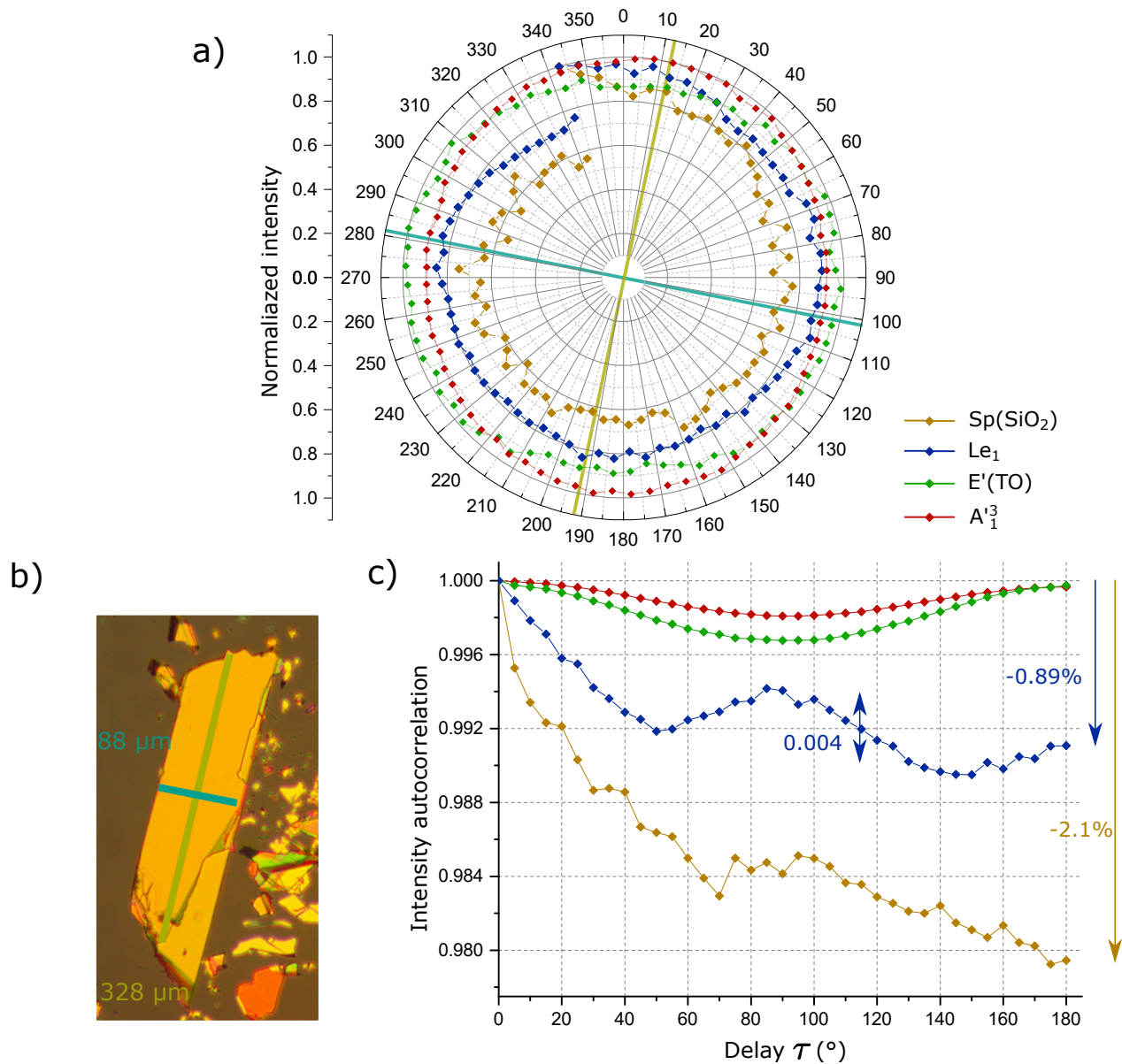


Figure 5.18 Intensity polarization response of the sample of thickness  $820 \pm 1$  nm and lateral dimensions of  $88 \times 328 \mu m$ . **a)** each intensity scans are individually normalized. Diamonds correspond to the experimental data. The cyan and yellow solid lines depicts the orientation of the sample short and long axis. These lines are also displayed in **b)**, superimposed on an optical image of the sample. This images shows the position of the sample during experiments. The autocorrelation of the intensity polarization response is shown in **c)**.

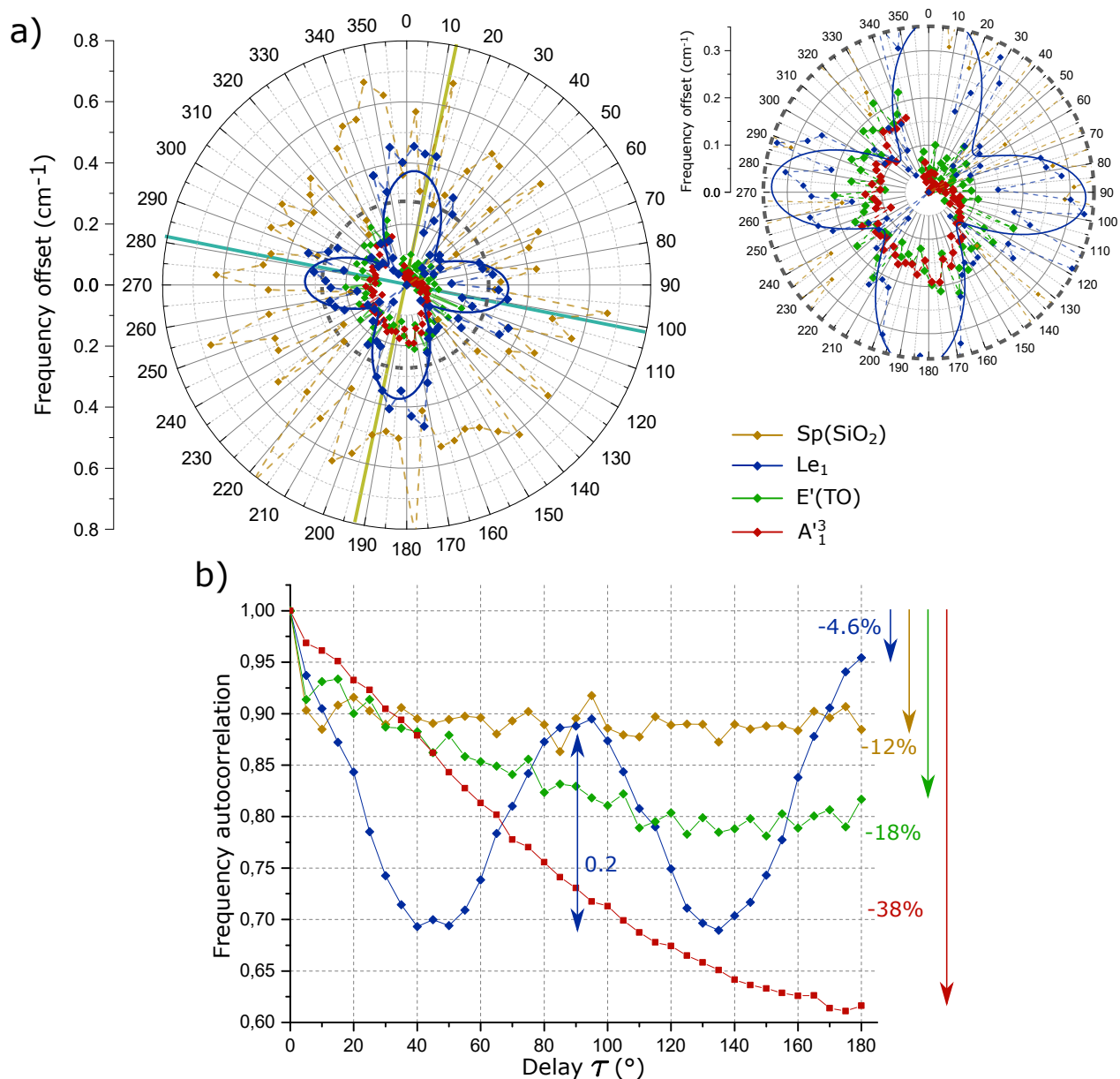


Figure 5.19 Frequency polarization response of the sample of thickness  $820 \pm 1$  nm and lateral dimensions of  $88 \times 328$   $\mu\text{m}$ . The frequencies are assimilated to the intensities of the polarization scan of Fig. 5.18. The frequency offset with respect to the lower reported frequency is shown in **a**), as a function of the polarization angle. Diamonds correspond to the experimental data while the solid blue curve shows the fit of Eq. 5.3 to the Le<sub>1</sub> polariton data. The cyan and yellow solid lines depicts the orientation of the sample short and long axis (see Fig. 5.18 **b**)). The autocorrelation of the frequency offsets is shown in **b**).

### Third sample: Frequency polarization response

Fig. 5.19 shows the frequency offset associated to the intensity polarization scans from Fig. 5.18. This figure is presented in the same fashion as Fig. 5.15 and Fig. 5.17.

The inset of Fig. 5.19 **a)** zooms onto lower frequency offsets to better visualize the evolution of the two phonons. A second unusual polarization scan is observed as the frequency offset remains close to  $0\text{ cm}^{-1}$  up to a polarization angle of  $90^\circ$ , and then increases rapidly up to  $0.2\text{ cm}^{-1}$  with a pattern that could be assimilated to a  $180^\circ$  periodic response. The autocorrelation shown in Fig. 5.19 **c)** displays a linear decrease with no modulation by a periodic  $180^\circ$  periodic pattern. This demonstrates that the frequency variation is mainly linear. The loss of correlation is substantial for  $A_1^3$  ( $\gamma_{freq} = 38\%$ ) and on the same order of magnitude as already observed for  $E'(TO)$  ( $\gamma_{freq} = 18\%$ ). There is no explanation for this unusual frequency variation yet. The frequency offsets of these two phonons are two times lower compared to the  $Le_1$  polariton discussed below. This unexpected frequency offset polarization scan is therefore set aside.

As can be seen in Fig. 5.19 **a)**, the polarization response of the  $Sp(SiO_2)$  is isotropic, with significant variations in the frequency. Because of these variations, the fit quality of Eq. 5.3 to the data is unsatisfactory. The autocorrelation displayed in Fig. 5.19 **c)** shows a quick drop of autocorrelation followed by a constant value of 0.88 revealing a uniform frequency variation. The correlation loss is  $\gamma_{freq} = 12\%$ . In the previous samples, the frequency shift of the  $Sp(SiO_2)$  decreased with increasing the sample dimension. This sample is then probably too large for this mode to be laterally confined. This explains the observed isotropic response comparable to the  $Le_1$  polariton from the wide GaSe sample presented in Figs. 5.12 and 5.13.

A four-lobed polarization pattern is observed for the  $Le_1$  polariton as depicted in Fig. 5.19 **a)**. The maximum frequency offset is  $0.5\text{ cm}^{-1}$ , similar to the  $Le_1$  from the previous sample. The larger sample dimensions did not decrease the frequency shift of this polariton. A two-lobed pattern modulates the polarization response as a slight frequency difference of nearly  $0.1\text{ cm}^{-1}$  is observed between the short and long sample axes. Similarly to the first sample, the higher frequency shifts are aligned with the sample long axes. The polarization lobes are well aligned with the sample axes since a deviation angle of  $6^\circ$  is observed.

The fit of Eq. 5.3 to the  $Le_1$  data provides fit coefficients of  $C_0 = 0.212$ ,  $C_1 = 0.142$  and  $C_2 = 0.646$ . The  $C_2$  coefficient dominates, illustrating the observed symmetric four-lobed pattern polarization response. The  $C_0$  coefficient is one order of magnitude higher than the previous samples presenting a four-lobed response and denotes a lower polarization anisotropy contrast. This loss of contrast results from the larger sample dimension, which induces

weaker lateral confinement effects along the sample axes. The  $C_1$  coefficient is lower than of the Sp(SiO<sub>2</sub>) of the first sample but 2.5 times higher than that of the second and reveals a moderate 180° periodic pattern modulation.

The autocorrelation is depicted in Fig. 5.19 c). A value  $\rho(180^\circ) - \rho(90^\circ)$  of 0.067 is extracted, between values extracted from the Sp(SiO<sub>2</sub>) frequency autocorrelation of the two first samples. It further demonstrates the presence of a two-lobed modulation within the Le<sub>1</sub> polarization response. The oscillation amplitude of the autocorrelation is 0.2, and a total correlation loss of  $\gamma_{freq} = 4.6\%$  is extracted. These values are comparable to those extracted above from polariton modes presenting lateral confinement effects. The Sp(SiO<sub>2</sub>) PhP therefore presents evidence of lateral confinement effects despite the much larger sample dimensions.

### Third sample: conclusion

In this sample, the polarization responses show a decrease in measurement quality due to the excitation time required to record a polarization scan (linear decrease in Raman line intensity or frequency). This phenomenon can be induced by the degradation of the sample during the excitation time. In the presented results, the effects are slight. In some cases, however, it is necessary to redo the entire polarization scan. Nonetheless, the data processing revealed interesting polarization anisotropy for the Le<sub>1</sub> polariton both in the intensity and frequency scan. This PhP therefore presents evidence of lateral confinement effects and a PhP propagation length could be estimated to 328 μm. If this result is confirmed, the propagation length of this PhP is one order of magnitude higher than reported in hBN and MoO<sub>3</sub>.

### Summary

This section presented experimental evidence of PhP lateral confinement effects in rectangular GaSe samples. Lateral confinement effects are revealed by polarization anisotropy with a 90° symmetry that is aligned with the sample axes, either in the intensity or the frequency polarization response. The mathematical tools presented in Sec. 5.2.1 have proved to be complementary resources to characterize and quantify the anisotropy within the polarization scans. Especially, the autocorrelation is powerful in probing the periodicity of a signal, even in the presence of strong variations. These experimental results enabled a first estimation of the PhP propagation lengths. Polarization-resolved Raman can therefore probe vertical confinement effects, and GaSe appears to be a good candidate for the development of PhP waveguides.

## CHAPTER 6 CONCLUSION

### 6.1 Contributions

This thesis presents the continuation of a work [24] initiated by *Bergeron* on the study of PhPs from GaSe using Raman backscattering.

The first contribution of this work is the development of a FEM model in order to compute PhP field maps in a 2D geometry. It enabled a better understanding of the origin of the surface polariton modes splitting, either in a symmetric or an asymmetric waveguide. Given a PhP frequency reported from a Raman spectra, this model can compute the associated polariton field and its theoretical wavevector. This wavevector can then be compared with the range of wavevectors probed within the numerical aperture of the instrumentation. Unfortunately, the lateral degree of freedom could not be exploited to compute laterally guided PhPs because of the problems encountered during the development of this model.

The second contribution is the measurement of the polariton dispersion relation as a function of GaSe sample thicknesses. Five samples with a thickness between 201 nm and 12  $\mu\text{m}$  were measured. The expected dispersion curve flattening with decreasing sample thickness was observed experimentally. Moreover, only one surface mode was usually reported in the spectra. Here, the coincident measurement of the two surface modes is reported along with their dispersion. Then, a group velocity of  $0.014c$  could be extracted for the  $\text{Le}_1$  polariton thanks to the good quality of its measured dispersion curve. This value is one order magnitude higher than the lower reported in the literature, which reveal that the  $\text{Le}_1$  PhP from GaSe is less dispersive. Finally, confinement factors of approximately 70 and 100 are reported for the  $\text{Sp}(\text{SiO}_2)$  and  $\text{Le}_1$  polaritons respectively. These values exceed the ones reported in the literature for hBN monolayers [41] and thin  $\text{MoO}_3$  [44]. The coupling from the interaction of such a confined light with a quantum emitter would be highly improved, which makes PhPs from GaSe very promising for the development of polaritonic devices.

In his previous work, *Bergeron* computed Raman spectra of PhPs as a function of the sample thickness [24]. This calculation predicted a decrease of the  $\text{Sp}(\text{SiO}_2)$  frequency for samples below 400 nm. Additionally, the  $\text{Le}_1$  Raman line should broaden in samples of larger thickness because of the propagation of higher-order modes. Therefore, the third contribution of this work is the addition of experimental data to this calculation to corroborate the predicted sample thickness dependence of the polariton frequencies. 14 samples were measured, which makes a total of 17 samples with thickness ranging from 30 to 750 nm (3 samples were

already measured by *Bergeron*). The reported polariton frequencies are in accordance with the calculated Raman spectra. Between sample thicknesses of 84 and 380 nm, a frequency shift of  $18.1 \pm 0.4 \text{ cm}^{-1}$  (2.24 meV) for the  $\text{Sp}(\text{SiO}_2)$  polariton is observed in addition to a linear variation of  $\sim 0.06 \text{ cm}^{-1}/\text{nm}$ . These data, along with the second contribution of this work discussed above, demonstrate that PhPs experiences strong vertical confinement effects which can be studied with Raman scattering. The PhP frequency measured at normal incidence could be used to estimate the sample thickness between 100 nm and 12  $\mu\text{m}$ .

The fourth contribution of this work concerns experimental evidence of lateral confinement of PhPs in rectangular GaSe samples. The PhP frequency shifts when the dimension of the sample is comparable to the polariton propagation length. Polarization-resolve Raman scattering is utilized and the excitation polarization is rotated to probe the PhP polarization response along the sample axes. The PhPs intensity and frequency polarization scans eventually display a symmetrical four-lobed polarization response, which indicates the presence of PhP lateral confinement. Moreover, the polarization lobes are mostly aligned with the sample axes. A maximum frequency shift of  $1.2 \text{ cm}^{-1}$  between the polariton propagating along the long axis of the sample and that propagating along a diagonal of the sample axes is reported. The propagation length of the measured polaritons can be estimated as the sample long axis length. A propagation length of up to 328  $\mu\text{m}$  could be approximated, which is one order of magnitude larger than the ones reported in hBN and  $\text{MoO}_3$  [31]. This places PhPs from GaSe as an excellent candidate to develop efficient polariton waveguides.

## 6.2 future works and conclusion

Despite the exciting results presented in this thesis, using Raman scattering to probe PhP properties is still a very recent method that needs to be perfected.

First, computational models are essential to give more credit to experimental data. However, because of the failed attempt on the FEM model in this work, no computational model is available yet to model lateral confinements of PhPs. This could detriment future publications in peer-reviewed journals and therefore slow the development of Raman scattering for the study of PhPs. Therefore, more effort should be dedicated to developing a model capable of modeling laterally confined PhPs.

Thin GaSe samples are very sensitive to oxidation, so much so that samples are damaged within a few minutes without precautions [76]. In this work, the samples are enclosed in a pump cryostat, limiting the oxidation reactions during measurements. However, the samples were fabricated in ambient air. Residual air humidity could infiltrate the sample and initiate

oxidation reactions over a certain amount of time. Therefore, the exfoliation process should be performed under a controlled environment to increase the quality of the samples. This is why a recently purchased glove box will benefit future works.

Then, the actual resolution of the Raman instrumentation can prevent the observation of small PhP frequency shifts. The frequency anisotropy usually observed is around  $1\text{ cm}^{-1}$  and less, at the limit of the instrumentation resolution. The spectrometer grating will be upgraded to multiply the frequency resolution by two. Therefore, the quality of the Raman data will improve and smaller PhP frequency shifts will be accessible.

Finally, there needs to be more available data on the lateral confinement of PhPs. Moreover, these data are hardly comparable because the exfoliation process cannot control the thickness of the GaSe samples. Therefore, a well-defined exfoliation process should be considered to increase the chances of obtaining samples of comparable thickness. Then, experimental data should be accumulated so lateral confinement of PhPs can be characterized as a function of the lateral sample dimension. After that, vertical and lateral confinement could be combined to study 1D PhPs.

Combined with the previous work led by *Bergeron* in Ref. [24], this work confirmed and extended the ability of Raman scattering in studying PhPs from thin GaSe crystals. Similarly to the s-SNOM technique, Raman scattering can measure the dispersion of PhPs along with their properties, such as their confinement factor, group velocity, and propagation length. Excellent properties of PhP from GaSe were extracted, eventually surpassing the state-of-the-art. GaSe is, therefore, a serious candidate in the development of phonon-polaritonics in the future.

## REFERENCES

- [1] K. B. Tolpygo, “Physical properties of a rock salt lattice made up of deformable ions,” *Ukrainian Journal of Physics*, vol. 53, 1950.
- [2] K. Huang, “On the interaction between the radiation field and ionic crystals,” *The Royal Society*, vol. 208, no. 1094, pp. 352–364, 1951.
- [3] J. J. Hopfield, “Theory of the Contribution of Excitons to the Complex Dielectric Constant of Crystals,” *Physical Review*, vol. 112, pp. 1555–1567, Dec. 1958.
- [4] X. Guo, W. Lyu, T. Chen, Y. Luo, C. Wu, B. Yang, Z. Sun, F. J. García de Abajo, X. Yang, and Q. Dai, “Polaritons in Van der Waals Heterostructures,” *Advanced Materials*, p. 2201856, Mar. 2023.
- [5] A. Reserbat-Plantey, I. Epstein, I. Torre, A. T. Costa, P. A. D. Gonçalves, N. A. Mortensen, M. Polini, J. C. W. Song, N. M. R. Peres, and F. H. L. Koppens, “Quantum Nanophotonics in Two-Dimensional Materials,” *ACS Photonics*, vol. 8, pp. 85–101, Jan. 2021.
- [6] S. Foteinopoulou, G. C. R. Devarapu, G. S. Subramania, S. Krishna, and D. Wasserman, “Phonon-polaritonics: enabling powerful capabilities for infrared photonics,” *Nanophotonics*, vol. 8, pp. 2129–2175, Oct. 2019.
- [7] D. Sanvitto and S. Kéna-Cohen, “The road towards polaritonic devices,” *Nature Materials*, vol. 15, pp. 1061–1073, Oct. 2016.
- [8] D. N. Basov, A. Asenjo-Garcia, P. J. Schuck, X. Zhu, and A. Rubio, “Polariton panorama,” *Nanophotonics*, vol. 10, pp. 549–577, Nov. 2020.
- [9] C. Schneider, K. Winkler, M. D. Fraser, M. Kamp, Y. Yamamoto, E. A. Ostrovskaya, and S. Höfling, “Exciton-polariton trapping and potential landscape engineering,” *Reports on Progress in Physics*, vol. 80, p. 016503, Jan. 2017.
- [10] F. I. Moxley, E. O. Ilo-Okeke, S. Mudaliar, and T. Byrnes, “Quantum technology applications of exciton-polariton condensates,” *Emergent Materials*, vol. 4, pp. 971–988, Aug. 2021.

- [11] J. Tang, J. Zhang, Y. Lv, H. Wang, F. F. Xu, C. Zhang, L. Sun, J. Yao, and Y. S. Zhao, “Room temperature exciton–polariton Bose–Einstein condensation in organic single-crystal microribbon cavities,” *Nature Communications*, vol. 12, p. 3265, Dec. 2021.
- [12] J. Keeling and S. Kéna-Cohen, “Bose–Einstein Condensation of Exciton-Polaritons in Organic Microcavities,” *Annual Review of Physical Chemistry*, vol. 71, pp. 435–459, Apr. 2020.
- [13] Z. Jiang, A. Ren, Y. Yan, J. Yao, and Y. S. Zhao, “Exciton-Polaritons and Their Bose–Einstein Condensates in Organic Semiconductor Microcavities,” *Advanced Materials*, vol. 34, p. 2106095, Jan. 2022.
- [14] Y.-C. Chen, B. Song, A. J. Leggett, P. Ao, and X. Zhu, “Resonant Confinement of an Excitonic Polariton and Ultraefficient Light Harvest in Artificial Photosynthesis,” *Physical Review Letters*, vol. 122, p. 257402, June 2019.
- [15] N. Rivera, I. Kaminer, B. Zhen, J. D. Joannopoulos, and M. Soljačić, “Shrinking light to allow forbidden transitions on the atomic scale,” *Science*, vol. 353, pp. 263–269, July 2016.
- [16] R. S. Anwar, H. Ning, and L. Mao, “Recent advancements in surface plasmon polaritons-plasmonics in subwavelength structures in microwave and terahertz regimes,” *Digital Communications and Networks*, vol. 4, pp. 244–257, Nov. 2018.
- [17] Z. Guo, H. Jiang, and H. Chen, “Hyperbolic metamaterials: From dispersion manipulation to applications,” *Journal of Applied Physics*, vol. 127, p. 071101, Feb. 2020.
- [18] S. Dai, Z. Fei, Q. Ma, A. S. Rodin, M. Wagner, A. S. McLeod, M. K. Liu, W. Gannett, W. Regan, K. Watanabe, T. Taniguchi, M. Thiemens, G. Dominguez, A. H. C. Neto, A. Zettl, F. Keilmann, P. Jarillo-Herrero, M. M. Fogler, and D. N. Basov, “Tunable Phonon Polaritons in Atomically Thin van der Waals Crystals of Boron Nitride,” *Science*, vol. 343, pp. 1125–1129, Mar. 2014.
- [19] S.-J. Yu, Y. Jiang, J. A. Roberts, M. A. Huber, H. Yao, X. Shi, H. A. Bechtel, S. N. Gilbert Corder, T. F. Heinz, X. Zheng, and J. A. Fan, “Ultrahigh-Quality Infrared Polaritonic Resonators Based on Bottom-Up-Synthesized van der Waals Nanoribbons,” *ACS Nano*, vol. 16, pp. 3027–3035, Feb. 2022.
- [20] J. J. Schwartz, S. T. Le, S. Krylyuk, C. A. Richter, A. V. Davydov, and A. Centrone, “Substrate-mediated hyperbolic phonon polaritons in MoO<sub>3</sub>,” *Nanophotonics*, vol. 10, pp. 1517–1527, Mar. 2021.

- [21] S. G. Menabde, S. Boroviks, J. Ahn, J. T. Heiden, K. Watanabe, T. Taniguchi, T. Low, D. K. Hwang, N. A. Mortensen, and M. S. Jang, “Near-field probing of image phonon-polaritons in hexagonal boron nitride on gold crystals,” *Science Advances*, vol. 8, p. eabn0627, July 2022.
- [22] P. Tonndorf, R. Schmidt, P. Böttger, X. Zhang, J. Börner, A. Liebig, M. Albrecht, C. Kloc, O. Gordan, D. R. T. Zahn, S. M. de Vasconcellos, and R. Bratschitsch, “Photoluminescence emission and Raman response of monolayer MoS<sub>2</sub>, MoSe<sub>2</sub>, and WSe<sub>2</sub>,” *Optics Express*, pp. 4908–4916, 2013.
- [23] C. H. Henry and J. J. Hopfield, “Raman Scattering by Polaritons,” *Physical Review Letters*, vol. 15, pp. 964–966, Dec. 1965.
- [24] A. Bergeron, *Raman Scattering From Hyperbolic Phonon-Polaritons in 2D Materials*. PhD Thesis, Polytechnique Montréal, 2020.
- [25] G. Fowles, “Introduction to Modern Optics,” Dover publications, 2nd ed., 1989.
- [26] A. Aigner, J. M. Dawes, S. A. Maier, and H. Ren, “Nanophotonics shines light on hyperbolic metamaterials,” *Light: Science & Applications*, vol. 11, p. 9, Dec. 2022.
- [27] P. Shekhar, J. Atkinson, and Z. Jacob, “Hyperbolic metamaterials: fundamentals and applications,” *Nano Convergence*, vol. 1, p. 14, Dec. 2014.
- [28] D. Lee, S. So, and G. Hu et. al, “Hyperbolic metamaterials: fusing artificial structures to natural 2D materials,” *eLight*, vol. 2, no. 1, 2022.
- [29] L. Ferrari, C. Wu, D. Lepage, X. Zhang, and Z. Liu, “Hyperbolic metamaterials and their applications,” *Progress in Quantum Electronics*, vol. 40, pp. 1–40, Mar. 2015.
- [30] R. Estevâm da Silva, R. Macêdo, T. Dumelow, J. A. P. da Costa, S. B. Honorato, and A. P. Ayala, “Far-infrared slab lensing and subwavelength imaging in crystal quartz,” *Physical Review B*, vol. 86, p. 155152, Oct. 2012.
- [31] G. Ni, A. S. McLeod, Z. Sun, J. R. Matson, C. F. B. Lo, D. A. Rhodes, F. L. Ruta, S. L. Moore, R. A. Vitalone, R. Cusco, L. Artús, L. Xiong, C. R. Dean, J. C. Hone, A. J. Millis, M. M. Fogler, J. H. Edgar, J. D. Caldwell, and D. N. Basov, “Long-Lived Phonon Polaritons in Hyperbolic Materials,” *Nano Letters*, vol. 21, pp. 5767–5773, July 2021.

- [32] E. Yoxall, M. Schnell, A. Y. Nikitin, O. Txoperena, A. Woessner, M. B. Lundeberg, F. Casanova, L. E. Hueso, F. H. L. Koppens, and R. Hillenbrand, “Direct observation of ultraslow hyperbolic polariton propagation with negative phase velocity,” *Nature Photonics*, vol. 9, pp. 674–678, Oct. 2015.
- [33] J. Mathurin, E. Pancani, A. Deniset-Besseau, K. Kjoller, C. B. Prater, R. Gref, and A. Dazzi, “How to unravel the chemical structure and component localization of individual drug-loaded polymeric nanoparticles by using tapping AFM-IR,” *The Analyst*, vol. 143, no. 24, pp. 5940–5949, 2018.
- [34] G. Pavlidis, J. J. Schwartz, J. Matson, T. Folland, S. Liu, J. H. Edgar, J. D. Caldwell, and A. Centrone, “Experimental confirmation of long hyperbolic polariton lifetimes in monoisotopic ( $^{10}\text{B}$ ) hexagonal boron nitride at room temperature,” *APL Materials*, vol. 9, p. 091109, Sept. 2021.
- [35] D. J. Evans, S. Ushioda, and J. D. McMullen, “Raman Scattering from Surface Polaritons in a GaAs Film,” *Physical Review Letters*, vol. 31, pp. 369–372, Aug. 1973.
- [36] J. H. Nicola and R. C. C. Leite, “Resonant Raman scattering from polaritons in ZnSe,” *Physical Review B*, vol. 11, pp. 798–801, Jan. 1975.
- [37] J. B. Valdez, G. Matteit, and S. Ushioda, “Light scattering spectra of guided wave polaritons in thin crystals: Experiment,” vol. 27, no. 11, p. 4, 1978.
- [38] Y. Sasaki and S. Ushioda, “Guided-wave polaritons in thin films of the layered compound GaSe,” *Physical Review B*, vol. 27, pp. 1122–1135, Jan. 1983.
- [39] G. Irmer, C. Röder, C. Himcinschi, and J. Kortus, “Phonon polaritons in uniaxial crystals: A Raman scattering study of polaritons in  $\alpha$ -GaN,” *Physical Review B*, vol. 88, p. 104303, Sept. 2013.
- [40] J. J. S. Viner, L. P. McDonnell, P. Rivera, X. Xu, and D. C. Smith, “Insights into hyperbolic phonon polaritons in h-BN using Raman scattering from encapsulated transition metal dichalcogenide layers,” *Physical Review B*, vol. 104, p. 165404, Oct. 2021.
- [41] S. Dai, W. Fang, N. Rivera, Y. Stehle, B. Jiang, J. Shen, R. Y. Tay, C. J. Ciccarino, Q. Ma, D. Rodan-Legrain, P. Jarillo-Herrero, E. H. T. Teo, M. M. Fogler, P. Narang, J. Kong, and D. N. Basov, “Phonon Polaritons in Monolayers of Hexagonal Boron Nitride,” *Advanced Materials*, vol. 31, p. 1806603, Sept. 2019.

- [42] Jiong Yang, Jianbo Tang, and et. al., “High-Q Phonon-polaritons in Spatially Confined Freestanding  $\alpha$ -MoO<sub>3</sub>,” *ACS Photonics*, vol. 9, no. 3, pp. 905–913, 2022.
- [43] Y. Zhao, J. Chen, and et. al., “Ultralow-Loss Phonon Polaritons in the Isotope-Enriched  $\alpha$ -MoO<sub>3</sub>.pdf,” *Nano Letters*, vol. 22, no. 24, pp. 10208–10215, 2022.
- [44] W. Ma, P. Alonso-González, S. Li, A. Y. Nikitin, J. Yuan, J. Martín-Sánchez, J. Taboada-Gutiérrez, I. Amenabar, P. Li, S. Vélez, C. Tollan, Z. Dai, Y. Zhang, S. Sri-ram, K. Kalantar-Zadeh, S.-T. Lee, R. Hillenbrand, and Q. Bao, “In-plane anisotropic and ultra-low-loss polaritons in a natural van der Waals crystal,” *Nature*, vol. 562, pp. 557–562, Oct. 2018.
- [45] R. Cuscó, “Isotopic Disorder: The Prevailing Mechanism in Limiting the Phonon Lifetime in Hexagonal BN,” *Physical Review B*, vol. 124, no. 16, p. 167402, 2020.
- [46] Qu Yunpeng, Chen Na, Teng, Hanchao, and et. al., “Tunable planar focusing based on hyperbolic phonon-polaritons in MoO<sub>3</sub>,” *Advanced Materials*, vol. 34, p. 2105590, June 2022.
- [47] P. Li, M. Lewin, A. V. Kretinin, J. D. Caldwell, K. S. Novoselov, T. Taniguchi, K. Watanabe, F. Gaussmann, and T. Taubner, “Hyperbolic phonon-polaritons in boron nitride for near-field optical imaging and focusing,” *Nature Communications*, vol. 6, p. 7507, Nov. 2015.
- [48] N. Rivera, G. Rosolen, J. D. Joannopoulos, I. Kaminer, and M. Soljačić, “Making two-photon processes dominate one-photon processes using mid-IR phonon polaritons,” *Proceedings of the National Academy of Sciences*, vol. 114, pp. 13607–13612, Dec. 2017.
- [49] W. Li and J. Li, “Piezoelectricity in two-dimensional group-III monochalcogenides,” *Nano Research*, vol. 8, pp. 3796–3802, Dec. 2015.
- [50] H. L. Zhuang and R. G. Hennig, “Single-Layer Group-III Monochalcogenide Photocatalysts for Water Splitting,” *Chemistry of Materials*, vol. 25, pp. 3232–3238, Aug. 2013.
- [51] Y. Cui, L. Peng, L. Sun, Q. Qian, and Y. Huang, “Two-dimensional few-layer group-III metal monochalcogenides as effective photocatalysts for overall water splitting in the visible range,” *Journal of Materials Chemistry A*, vol. 6, no. 45, pp. 22768–22777, 2018.
- [52] L. Ghalouci, B. Benbahi, S. Hiadsi, B. Abidri, G. Vergoten, and F. Ghalouci, “First principle investigation into hexagonal and cubic structures of Gallium Selenide,” *Computational Materials Science*, vol. 67, pp. 73–82, Feb. 2013.

- [53] S. Y. Lim, J.-U. Lee, J. H. Kim, L. Liang, X. Kong, T. T. H. Nguyen, Z. Lee, S. Cho, and H. Cheong, “Polytypism in few-layer gallium selenide,” *Nanoscale*, vol. 12, no. 15, pp. 8563–8573, 2020.
- [54] K. R. Allakhverdiev, M. O. Yetis, S. Ozbek, T. K. Baykara, and E. Y. Salaev, “Effective nonlinear GaSe crystal. Optical properties and applications,” *Laser Physics*, vol. 19, pp. 1092–1104, May 2009.
- [55] M. May, S. Debrus, K. Zakrzewska, H. Benisty, and A. Chevy, “Room-temperature optical nonlinearities in bulk GaSe,” *Journal of the Optical Society of America B*, vol. 14, p. 1048, May 1997.
- [56] X. Zhou, J. Cheng, Y. Zhou, T. Cao, H. Hong, Z. Liao, S. Wu, H. Peng, K. Liu, and D. Yu, “Strong Second-Harmonic Generation in Atomic Layered GaSe,” *Journal of the American Chemical Society*, vol. 137, pp. 7994–7997, July 2015.
- [57] C. Kittel, *Introduction to solid state physics*. Hoboken, NJ: Wiley, 8th ed ed., 2005.
- [58] J. Irwin, R. Hoff, B. Clayman, and R. Bromley, “Long wavelength lattice vibrations in GaS and GaSe,” *Solid State Communications*, vol. 13, pp. 1531–1536, Nov. 1973.
- [59] R. S. Mulliken, “Report on Notation for the Spectra of Polyatomic Molecules,” *The Journal of Chemical Physics*, vol. 23, pp. 1997–2011, Nov. 1955.
- [60] R. Loudon, “The Raman effect in crystals,” *Advances in Physics*, vol. 13, pp. 423–482, Oct. 1964.
- [61] D. L. Mills and E. Burstein, “Polaritons: the electromagnetic modes of media,” *Reports on Progress in Physics*, vol. 37, pp. 817–926, July 1974.
- [62] P. Y. Yu and M. Cardona, *Fundamentals of Semiconductors*. Graduate Texts in Physics, Berlin, Heidelberg: Springer Berlin Heidelberg, 2010.
- [63] S. Jandl, J. L. Brebner, and B. M. Powell, “Lattice dynamics of GaSe,” *Physical Review B*, vol. 13, pp. 686–693, Jan. 1976.
- [64] T. J. Wieting and J. L. Verble, “Infrared and Raman Investigations of Long-Wavelength Phonons in Layered Materials,” in *Electrons and Phonons in Layered Crystal Structures* (T. J. Wieting and M. Schlüter, eds.), pp. 321–407, Springer Netherlands, 1979.
- [65] R. M. Hoff, J. C. Irwin, and R. M. A. Lieth, “Raman Scattering in GaSe,” *Canadian Journal of Physics*, vol. 53, pp. 1606–1614, Sept. 1975.

- [66] S. Jandl and J. L. Brebner, “Group Theoretical Analysis of Lattice Vibrations in GaSe Polytypes,” *Canadian Journal of Physics*, vol. 52, pp. 2454–2458, Dec. 1974.
- [67] H. Yoshida, S. Nakashima, and A. Mitsuishi, “Phonon Raman spectra of layer compound GaSe,” *Physica Status Solidi (b)*, vol. 59, pp. 655–666, Oct. 1973.
- [68] K. Allakhverdiev, E. Salaev, M. Tagyev, and L. Genzel, “Davydov doublets in Raman spectra of GaSe,” *Solid State Communication*, vol. 59, no. 3, pp. 133–136, 1986.
- [69] G. H. Wagnière and S. Woźniak, “Nonlinear Optical Properties,” in *Encyclopedia of Spectroscopy and Spectrometry*, pp. 375–387, Elsevier, 2017.
- [70] D. L. Mills, Y. J. Chen, and E. Burstein, “Raman scattering of light by polaritons in thin films; surface polaritons and size effects,” *Physical Review B*, vol. 13, pp. 4419–4438, May 1976.
- [71] K. Subbaswamy and D. Mills, “Light scattering spectra of guided wave polaritons in thin crystals: Theory,” *Solid State Communications*, vol. 27, pp. 1085–1088, Sept. 1978.
- [72] N. C. Passler and A. Paarmann, “Generalized  $4 \times 4$  matrix formalism for light propagation in anisotropic stratified media: study of surface phonon polaritons in polar dielectric heterostructures,” *Journal of the Optical Society of America B*, vol. 34, p. 2128, Oct. 2017.
- [73] P. Yeh, “Electromagnetic propagation in birefringent layered media,” *Journal of the Optical Society of America*, vol. 69, p. 742, May 1979.
- [74] R. Kitamura, L. Pilon, and M. Jonasz, “Optical constants of silica glass from extreme ultraviolet to far infrared at near room temperature,” *Applied Optics*, vol. 46, p. 8118, Nov. 2007.
- [75] W. Karstens, D. C. Bobela, and D. Y. Smith, “Impurity and free-carrier effects on the far-infrared dispersion spectrum of silicon,” *Journal of the Optical Society of America A*, vol. 23, p. 723, Mar. 2006.
- [76] A. Bergeron, J. Ibrahim, R. Leonelli, and S. Francoeur, “Oxidation dynamics of ultrathin GaSe probed through Raman spectroscopy,” *Applied Physics Letters*, vol. 110, p. 241901, June 2017.
- [77] B. M. Kowalski, N. Manz, D. Bethke, E. A. Shaner, A. Serov, and N. G. Kalugin, “Role of humidity in oxidation of ultrathin GaSe,” *Materials Research Express*, vol. 6, p. 085907, May 2019.

- [78] Q. Zhao, R. Frisenda, P. Gant, D. Perez de Lara, C. Munuera, M. Garcia-Hernandez, Y. Niu, T. Wang, W. Jie, and A. Castellanos-Gomez, “Toward Air Stability of Thin GaSe Devices: Avoiding Environmental and Laser-Induced Degradation by Encapsulation,” *Advanced Functional Materials*, vol. 28, p. 1805304, Nov. 2018.
- [79] A. Fali, S. T. White, T. G. Folland, M. He, N. A. Aghamiri, S. Liu, J. H. Edgar, J. D. Caldwell, R. F. Haglund, and Y. Abate, “Refractive Index-Based Control of Hyperbolic Phonon-Polariton Propagation,” *Nano Letters*, vol. 19, pp. 7725–7734, Nov. 2019.
- [80] Y. Kurman, N. Rivera, T. Christensen, S. Tsesses, M. Orenstein, M. Soljačić, J. D. Joannopoulos, and I. Kaminer, “Control of semiconductor emitter frequency by increasing polariton momenta,” *Nature Photonics*, vol. 12, pp. 423–429, July 2018.
- [81] P. A. Temple and C. E. Hathaway, “Multiphonon Raman Spectrum of Silicon,”
- [82] V. Riede et. al, “Two-Phonon Absorption Spectra in GaSe,” *physica status solidi (b)*, vol. 104, no. 1, pp. 277–282, 1981.
- [83] N.M. Gasanly, A. Aydinli, H. Özkan, and C. Kocabas, “4 Temperature-dependent Raman scattering spectra of  $\epsilon$ -GaSe layered crystal,” *Material Research Bulletin*, vol. 37, pp. 169–176, 2002.
- [84] K. Allakhverdiev, N. Fernelius, F. Gashimzade, J. Goldstein, E. Salaev, and Z. Salaeva, “Anisotropy of optical absorption in GaSe studied by midinfrared spectroscopy,” *Journal of Applied Physics*, vol. 93, pp. 3336–3339, Mar. 2003.
- [85] N. Kuroda, O. Ueno, and Y. Nishina, “Lattice-dynamical and photoelastic properties of GaSe under high pressures studied by Raman scattering and electronic susceptibility,” *Physical Review B*, vol. 35, pp. 3860–3870, Mar. 1987.
- [86] R. Le Toullec, J. C. Chervin, N. Piccioli, and A. Chevy, “Anharmonic effects in phonon spectra of GaSe,” *Applied Optics*, vol. 20, p. 2566, July 1981.

## APPENDIX

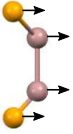
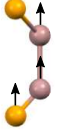
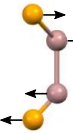
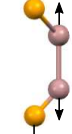
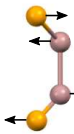
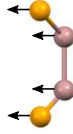
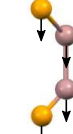
$E'(1^2)$	$A_2''(1^2)$	$E''(1^{1,2})$	$A_1'(1^{1,2})$	$E''(2^{1,2})$	$E'(2^{1,2})$	$A_2''(2^{1,2})$	$A_1'(2^{1,2})$
							
							
$19.5 \text{ cm}^{-1}$	$37.0 \text{ cm}^{-1}$	$60.1 \text{ cm}^{-1}$	$134.2 \text{ cm}^{-1}$	$210.4 \text{ cm}^{-1}$	TO: $213.5 \text{ cm}^{-1}$ LO: $253.3 \text{ cm}^{-1}$	TO: $236.5 \text{ cm}^{-1}$ LO: $246.1 \text{ cm}^{-1}$	$307.6 \text{ cm}^{-1}$
Raman Infrared	Infrared	Raman	Raman	Raman	Raman Infrared	Infrared	Raman
-	-	$\bar{x}(yz)x$ $\bar{y}(xz)y$	$\bar{x}(yy)x$ $\bar{x}(zz)x$ $\bar{y}(xx)y$ $\bar{y}(zz)y$ $\bar{z}(xx)z$ $\bar{z}(yy)z$	$\bar{x}(yz)x$ $\bar{y}(xz)y$	$\bar{y}(xx)y$ [LO] $\bar{x}(yy)x$ [TO] $\bar{z}(xx)z$ [TO] $\bar{z}(yy)z$ [TO]	-	$\bar{x}(yy)x$ $\bar{x}(zz)x$ $\bar{y}(xx)y$ $\bar{y}(zz)y$ $\bar{z}(xx)z$ $\bar{z}(yy)z$

Table S1 Normal modes of vibration of GaSe. From top to bottom for each mode are the representation of the mode ( $R(N^{a,b})$ ,  $N$  denotes for the occurrence number of the mode of representation  $R$ , and  $a, b$  are the Davydov numbering), atomic displacement in a unit cell (Davydov replica are omitted for clarity), frequency, mode activity and Raman selection rules.  $E'(1^2)$  and  $E''(1^{1,2})$  modes frequency taken from [65],  $A_2(1^2)$  from [82]. Reprinted with permission from Ref. [24] © 2020 Alaric Bergeron with updated frequency attribution from the literature review (see Table S2).

Reference (frequency in $\text{cm}^{-1}$ )	[83]	[65]	[84]*	[82]	[85]	[86]
$A_1'$	134.1	134.3	-	134	134	134.7
$E_2''$	209.7	211.9	-	212	208.7	-
$E'(TO)$	213.5	214	211-215	214	213.3	213.5
$A_2''(TO)$	-	-	236-237	237	236	-
$A_2''(LO)$	-	-	245-247	246	247	245.5
$E'(LO)$	253.2	252.1	252-255	255	251.5	254.2
$A_1'^4$	307.8	308	-	309	307.1	308.3

Table S2 Pure phonon frequencies of GaSe in the studied frequency range at room temperature, gathered from 6 references. \*: This reference reports many frequencies summarized in one table. The values picked are the minimum and maximum reported by this reference.

$D_{3h}$	E	$2C_3(z)$	$3C_2'$	$\sigma_h(xy)$	$2S_3$	$3\sigma_v$	linear functions, rotations	quadratic functions
$A_1'$	1	1	1	1	1	1	-	$x^2 + y^2, z^2$
$A_2'$	1	1	-1	1	1	-1	$R_z$	-
$E'$	2	-1	0	2	-1	0	(x,y)	$(x^2 - y^2, xy)$
$A_1''$	1	1	1	-1	-1	-1	-	-
$A_2''$	1	1	-1	-1	-1	1	z	-
$E''$	2	-1	0	-2	1	0	$(R_x, R_y)$	$(xz, yz)$

Table S3 Character table of the  $D_{3h}$  space group [64, 66].